Characterization of the architecture of BAK apoptotic foci and mitochondria-ER membrane contact sites

Dissertation

der Mathematisch-Naturwissenschaftlichen Fakultät

der Eberhard Karls Universität Tübingen

zur Erlangung des Grades eines

Doktors der Naturwissenschaften

(Dr. rer. nat.)

vorgelegt von

Vanessa Hertlein

aus Baden-Baden, Deutschland

Tübingen

2021

Gedruckt mit Genehmigung der Mathematisch-Naturwissenschaftlichen Fakultät der Eberhard Karls Universität Tübingen.

Tag der mündlichen Qualifikation:	10.11.2021
Dekan:	Prof. Dr. Thilo Stehle
1. Berichterstatter:	Prof. Dr. Ana J. García Sáez
2. Berichterstatter:	Prof. Dr. Ralf-Peter Jansen

Abstract

This thesis focuses on the study of mitochondrial alterations in apoptosis which is covered by two complementary projects: The first part (I) is dedicated to understanding the assembly mechanism of BAK and BAX during apoptosis. The second part (II) addresses the development of a novel proximity-based BRET biosensor for the investigation of mitochondria-ER membrane contact sites (MERCs), which are altered during apoptosis.

(I) BAK and BAX are key regulators of the intrinsic apoptosis pathway. They execute the permeabilization of the mitochondrial outer membrane, which is considered the point-of-no-return. Upon apoptotic stimulation, BAK and BAX oligomerize, assemble into foci, and form pores in the mitochondrial outer membrane. However, the assembly and pore formation mechanism are not fully understood. Therefore, the goals of this thesis are, (a) to characterize the apoptotic BAK assemblies, (b) to study the kinetics of BAK assemblies, (c) to investigate the contribution and influence of BAX on BAK assemblies, and (d) to explore the functional consequences of differences of the assembly mechanism and kinetics of BAK and BAX.

In this thesis, we have shown that BAK assembles into distinct supramolecular structures including rings, arcs and lines. These structures were similar to the ones formed by BAX, however, smaller and more uniform in size. The distribution of the BAK assemblies slightly changes over time during the progression of apoptosis, from more linear structures towards more rings. Furthermore, the two effectors co-assembled and influenced each other's supramolecular organization. Presence of endogenous BAX in BAK foci slightly increased their size. Interestingly, BAK pores enabled an earlier release of mtDNA highlighting that the difference in the assembly mechanisms can give rise to functional consequences.

(II) MERCs are distinct subdomains of the ER with close apposition to mitochondria. They are involved in many crucial cellular functions including calcium homeostasis, lipid biosynthesis and transport, mitochondrial morphology, and have been shown to play a role in apoptosis regulation. Therefore, the dynamics of these structures and their molecular composition is a matter of active research and novel tools are required for their investigation. In this thesis, we developed the proximity-based BRET biosensor MERLIN that enables the investigation of dynamic processes at the contact sites.

We systematically tested, optimized and verified the functionality of MERLIN. We showed the correct localization of the MERLIN constructs and a neglectable effect of MERLIN on cell viability and MERCs. We further validated MERLN by demonstrating its sensitivity to sense changes in MERCs after treatment with drugs known to cause concrete changes in MERCs and after overexpression or knockdown of the MERCs tether PDZD8. The main advantage of

MERLIN over other currently available biosensors is that MERLIN relies on proximity-sensing and does not require the formation of artificial physical links between the two organelles and thus allows the study of dynamic and reversible processes. We showed the ability of MERLIN to detect the plasticity of MERCs by transiently treating cells with stressors and following the kinetics of MERCs changes. MERLIN is capable of robustly detecting the increase in MERCS upon apoptosis induction.

Zusammenfassung

Diese Arbeit behandelt die Untersuchung der mitochondriellen Veränderungen, welche während der Apoptose auftreten, in zwei sich ergänzenden Projekten: (I) Das erste Projekt ist der Untersuchung des Mechanismus der Bildung von BAK und BAX Oligomeren während der Apoptose gewidmet. (II) Das zweite Projekt befasst sich mit der Entwicklung eines neuen BRET Biosensors namens MERLIN, welcher die Nahe zwischen Mitochondrien und dem ER an den Mitochondrien-ER Membran Kontaktstellen (MERCs) erspüren kann, die während der Apoptose verändert werden.

(I) BAK und BAX sind Schlüsselregulatoren des intrinsischen Apoptose Signalwegs. Sie führen den entscheidenden Schritt der intrinsischen Apoptose, die Permeabilisierung der mitochondriellen Außenmembran durch. Nach einem Apoptose Stimulus, akkumulieren und oligomerisiern BAK und BAX auf der mitochondriellen Außenmembran und formen Poren in der Membran. Dieser Prozess der Akkumulierung und Porenbildung ist jedoch noch nicht vollständig aufgeklärt. Die Ziele dieser Arbeit sind daher, (a) die Strukturen der BAK Akkumulierungen zu charakterisieren, (b) die Kinetik der BAK Akkumulierungen zu untersuchen, (c) den Einfluss von BAX auf BAK Akkumulierungen zu studieren und (d) herauszufinden welche funktionellen Konsequenzen die Unterschiede in der Kinetik und in dem Akkumulierungsmechanismus zwischen BAK und BAX bewirken.

In dieser Arbeit haben wir gezeigt, dass BAK klar abzugrenzende Strukturen bildet, beispielsweise Ringe, Halbringe und Linien. Diese Strukturen sind von der Form her denen von BAX ähnlich. Sie sind jedoch kleiner und einheitlicher in ihrer Größe. Darüber hinaus konnten wir zeigen, dass sich die Verteilung der BAK Akkumulierungen während dem Voranschreiten der Apoptose geringfügig verändert, von mehr Linien hinzu mehr Ringen. Die zwei Effektoren BAK und BAX beeinflussen sich gegenseitig, wenn sie gemeinsam akkumulieren. Das Vorhandensein von endogenem BAX in BAK Akkumulierungen lässt deren Größe leicht anwachsen. Die schnellere Akkumulierungskinetik von BAK aufgrund seiner mitochondriellen Lokalisierung verursacht einen funktionellen Unterschied zwischen BAK und BAX, in dem sie zu einer früheren Freisetzung der mtDNA führt.

(II) Die MERCs sind klar abgrenzbare Subdomänen des ER, welche einen sehr geringen Abstand zu den Mitochondrien aufweisen. Sie sind an vielen wichtigen Zellfunktionen beteiligt, unter anderem der Kalzium-Homöostase, der Synthese und dem Transport von Lipiden, der mitochondriellen Morphologie und es wurde zudem gezeigt, dass sie eine Rolle bei der Regulierung der Apoptose spielen. Die molekulare Zusammensetzung und die Dynamik dieser Strukturen sind daher Gegenstand aktiver Forschung und es ist deshalb notwendig neue Werkzeuge für ihre Erforschung zu entwickeln. In dieser Arbeit haben wir einen auf Nähe

zwischen den zwei Organellen basierenden BRET Biosensor namens MERLIN entwickelt. MERLIN ermöglicht es uns dynamische Vorgänge an den Kontaktstellen zu untersuchen.

Zuerst haben wir MERLIN systematisch getestet, optimiert und seine Funktionsfähigkeit bestätigt. Wir haben gezeigt, dass die MERLIN Konstrukte richtig lokalisiert sind und, dass sie einen zu vernachlässigenden Einfluss auf Zellvitalität und MERCs haben. Des Weiteren haben wir seine Funktionsfähigkeit bestätigt, indem wir demonstriert haben, dass MERLIN sensitiv genug ist, um Veränderungen in MERCs zu erspüren, welche wir durch MERCs beeinflussende Stoffe und Überexpression beziehungsweise gesenkter Expression eines MERCs Verbindungsproteins namens PDZD8 verursacht haben. Der größte Vorteil von MERLIN gegenüber anderen vorhandenen Biosensoren ist, dass MERLIN ausschließlich Nähe erspürt, und daher keine künstliche physikalische Kontakte zwischen den zwei Organellen herstellen muss. Dies ermöglicht MERLIN dynamische und umkehrbare Prozesse der MERCs zu detektieren. Indem wir Zellen für eine kurze Zeit mit MERCs Stressoren behandelt haben und währenddessen und danach Veränderungen in den MERCs gemessen haben, konnten wir diese Fähigkeit von MERLIN demonstrieren. Darüber hinaus ist MERLIN fähig zuverlässig den Anstieg in MERCs während der Apoptose aufzuzeigen.

Acknowledgment

First, I would like to express my deepest and sincere gratitude to you Ana. Thank you for all you have done for me during my four years with you. Without your contribution this work would have never been possible. You helped, encouraged, challenged and guided me through this whole journey. You inspired and supported me to become the scientist I am now. I'm extremely grateful that I had the opportunity to learn from you. Thank you!

To all my colleagues, who shared this time with me, those who left on the way (Aida, Bego, Britta, Joseph, Kushal, Raphael, Raquel, Rodrigo, Simon and Stephanie) and those who stayed with me till the finish line, I'm thankful that I had such wonderful colleagues. You all made these years special and contributed to amazing lab atmosphere. You all inspired, help and motivated me. I enjoyed the daily lab life and all our group activities. To Katia, I have greatly benefited from all our discussions, your comments and experience. I'm grateful that I had the opportunity to work together with you on a project. To Andreas, for always offering help, for always motivating me and for all the moments we shared together. To John, for our inspiring discussions and all his relentless support with the microscope. To Hector, for all his help, our long and sometimes exhausting debates and his German pronunciation that always made me smile. To Uris, for all the scientific support, always listening and providing good advice. To Lohans, for always being willing to help and for all her scientific and non-scientific support. To Raed, for all our small chats and always having words of encouragement. To Fabronia, for first and foremost being an amazing friend but also for all the scientific discussions we had and for always lending a hand. To Caro, who was always there when I needed help in the lab or outside of the lab, for her open and positive attitude and her friendship.

I would also like to thank my two TAC members Prof. Rapaport and Prof. Lupas, for participating in all my TAC meetings, for their constructive feedback, comments and suggestions. I would like to extend my acknowledgements to our collaborators Jonas Ries and Markus Mund from the EMBL in Heidelberg. For granting me permission to use their microscope, for their extensive support and for the insightful discussions. Thank you to my two amazing students Marina and Miralda, for all their motivation and help.

Outside of the lab, I would like to thank Michael and Vivien. To Michael, for always being there when I needed someone, for listening, caring and stepping on my toes more often than I stepped on yours. To Vivien, for becoming a friend I can always rely on, for all the ice creams and precious moments we shared.

Mehr Dank als ich jemals in Worte fassen kann geht an meine Eltern und meinen Bruder Maximilian, ohne die das alles nicht möglich gewesen wäre. Für eure bedingungslose Liebe und Unterstützung, für all eure aufmunternden Worte und dafür, dass ihr immer an mich geglaubt habt. Danke für alles, ohne euch wäre ich nicht der Mensch geworden, der ich heute bin. Ich liebe euch!

Contents

List of tables

List of figures

CHAPTER 1.

Introduction and Objectives

Apoptosis and the Bcl-2 family

Apoptosis is a form of regulated cell death that was first described in 1972 by Kerr, Wyllie and Currie as a mechanism of controlled cell dismissal to counterbalance cell division (Kerr, Wyllie, & Currie, 1972). Moreover, apoptosis is a crucial mechanism for the development of multicellular organisms, the proper function of the immune system, and the clearance of damaged and infected cells (Brokatzky et al., 2019; Elmore, 2007). Dysregulation of apoptosis has been linked to many disorders including cancer (Brown & Attardi, 2005; Ichim & Tait, 2016), autoimmune disease (Božič & Rozman, 2006) and Alzheimer's disease (Obulesu & Lakshmi, 2014). Morphologically apoptosis can be characterized by cell shrinkage, chromatin condensation and fragmentation, and the formation and "blebbing" of membrane-bound cell fragments (Buendia, Santa-Maria, & Courvalin, 1999; Taylor, Cullen, & Martin, 2008). These fragments, termed apoptotic bodies, are subsequently phagocytosed by macrophages. Due to the fact that the membrane stability of the cell fragments remains intact and inflammatory signals are neither released by the apoptotic nor by the phagocytosing cells, apoptosis is considered as an inflammatorily silent cell death (Savill & Fadok, 2000).

On the mechanistic level, there are two main apoptosis pathways: First, the extrinsic, or death receptor pathway and second, the intrinsic or mitochondrial pathway. Even though, the two pathways differ in the activation process they share the same execution phase mediated by the caspase cascade. The activation of the effector proteases Caspase-3 and Caspase-7 rapidly execute the cell death by degrading a define set of cellular components: extensive protein cleavage and organelle removal, DNA fragmentation by activated endonucleases, mRNA decay and the breakdown of the cytoskeleton (Enari et al., 1998; Kothakota et al., 1997; Rao, Perez, & White, 1996).

The extrinsic pathway is activated by extracellular ligand binding to a death receptor (Figure 1A). The two best characterized ligand/receptor pairs are the FasL/FasR and TNF-α/TNFR1 (Elmore, 2007). Binding of Fas ligand to Fas receptor results in the binding of

the adapter protein FADD to the intracellular death domain of FasR. FADD subsequently associates with pro-Caspase-8 via the death effector domain (DED) and forms the death-inducing signaling complex (DISC). At the DISC, the pro-Caspase-8 gets auto-activated and initiates the caspase cascade that executes the cell death. (Jin & El-Deiry, 2005; Wajant, 2002)

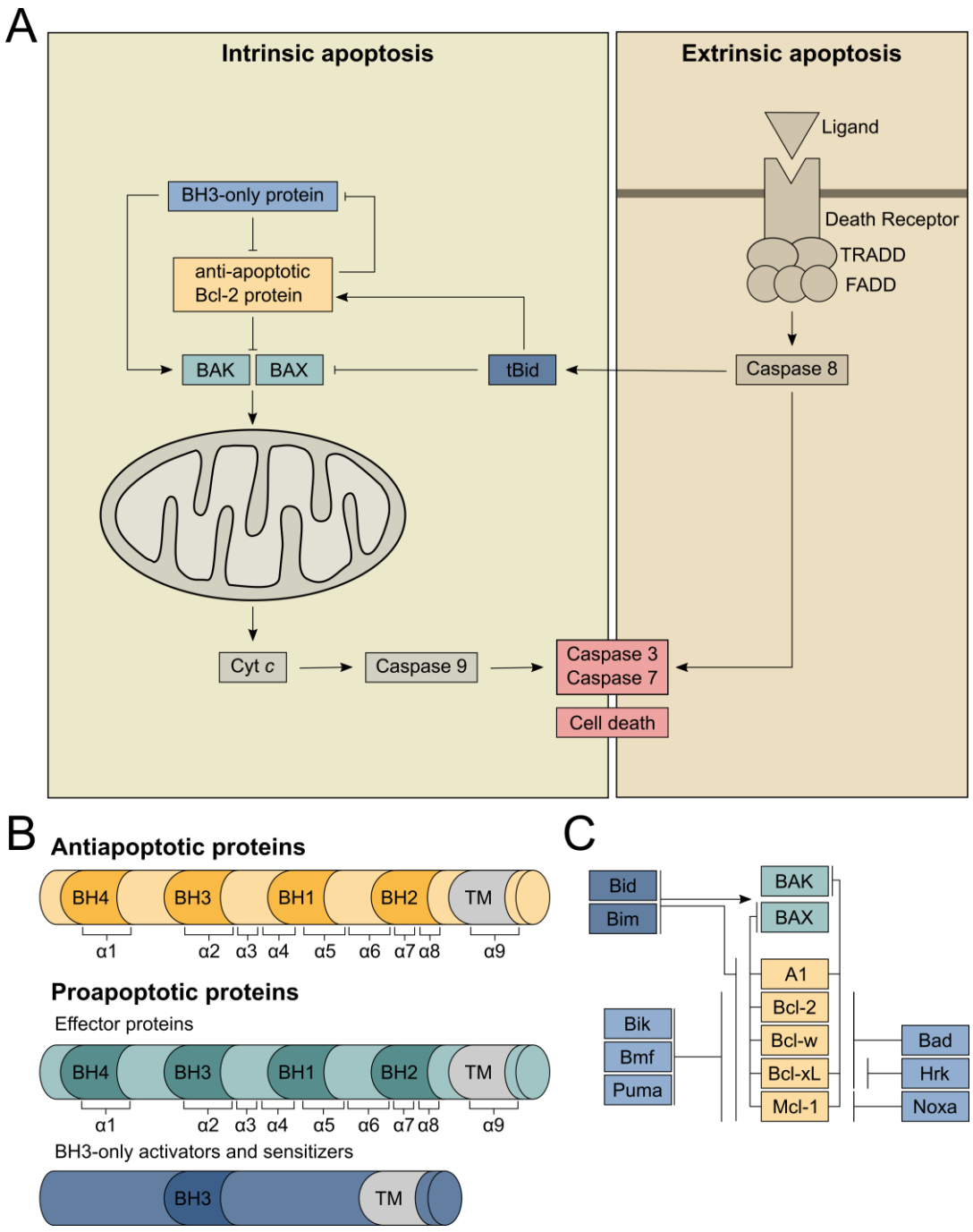

Figure 1: Scheme of the extrinsic and intrinsic apoptosis pathways, of the Bcl-2 family proteins and of their interaction network (previous page). *A) Scheme explaining the process of extrinsic and intrinsic apoptosis. The extrinsic apoptosis pathway is initiated by the binding of a ligand to the extracellular domain of a death receptor. The death receptor together with the adaptor proteins TRADD and FADD forms the death inducing signaling complex (DISC), the platform for the activation of initiator caspase 8. Caspase 8 activates the executor caspases 3 and 7, which execute the cellular demolition. In the intrinsic apoptosis, on the contrary, the mitochondria play a central role. The permeabilization of the mitochondrial outer membrane (MOMP) is regulated by the Bcl-2 protein family members. Stress stimuli activate the BH-3 only proteins which on one hand sequester the anti-apoptotic Bcl-2 family members and on the other hand activate the executor proteins BAK and BAX. Once activated BAK and BAX oligomerize and permeabilize the mitochondrial outer membrane enabling the release of pro-apoptotic factors like cytochrome c from the intermembrane space into the cytoplasm. The released cytochrome c together with Apaf1 and ATP forms the apoptosome, the activation platform of initiator caspase 9. Caspase 9 activates the executor caspases 3 and 7 which execute the cellular demolition. The extrinsic and intrinsic apoptosis pathways are linked via the activation of the BH3-only protein tBID by the caspase 8. B) The members of the Bcl-2 protein family classified by their role in apoptosis. The Bcl-2 family proteins can be subdivided into three groups based on their role in apoptosis and the presence of the Bcl-2 homology (BH) domains into the anti-apoptotic members, the pro-apoptotic effector proteins, and the pro-apoptotic BH3-only proteins that act as activators and sensitizers. The anti-apoptotic and the pro-apoptotic effector proteins adopt an α-helical structure while most of the BH3-only proteins are unstructured. The BH domains and the transmembrane (TM) domain and their positions in the α-helices are marked. C) Scheme of the interaction network of the members of the Bcl-2 protein family.*

Intrinsic apoptosis: The complex interaction network of the Bcl-2 family proteins

The intrinsic or mitochondrial pathway is tightly controlled by the Bcl-2 family proteins. The Bcl-2 family comprise at least 18 different members that share at least one of the four Bcl-2 homology domains (BH1-4). They can be subdivided into anti- and pro-apoptotic members generating a complex interaction network to regulate apoptosis induction (Chipuk, Moldoveanu, Llambi, Parsons, & Green, 2010; Youle & Strasser, 2008). The anti-apoptotic members like Bcl-2, Bcl-xL and Mcl-1 prevent apoptosis by inhibiting the pro-apoptotic proteins (Cheng et al., 2001; Opferman & Kothari, 2018). The pro-apoptotic proteins can be subdivided into the multi-domain effector proteins BAK and BAX and the BH3-only proteins, which solely contain a BH3 domain. The BH3-only proteins act as direct activators and sensitizers. They either directly activate the two executor proteins (e.g. Bid, Bim) or they indirectly activate BAK and BAX by blocking the anti-apoptotic members (e.g. Bad, Bik) (Kuwana et al., 2005; Letai et al., 2002) (Figure 1B). BAK and BAX execute the crucial step of the intrinsic apoptosis pathway (Chittenden et al., 1995; Oltvai, Milliman, & Korsmeyer, 1993). After their activation, BAK and BAX oligomerize and permeabilize the mitochondrial outer membrane (MOM). The permeabilization of the mitochondrial outer membrane (MOMP) is considered the point-of-no-return of the intrinsic apoptosis pathway (Wei et al., 2001). MOMP allows the release of pro-apoptotic factors from the intermembrane space (IMS) of mitochondria to the cytoplasm like Smac/DIABLO and cytochrome *c*. The release of Smac/DIABLO from mitochondria antagonizes the inhibitory effect of the IAPs towards the caspases and cytochrome *c* together with Apaf-1 and ATP

forms the activation platform for the initiator Caspase-9, the apoptosome (C. Du, Fang, Li, Li, & Wang, 2000; P. Li et al., 1997; Verhagen et al., 2000). The activated Caspase-9 subsequently initiates the caspase cascade (Figure 1A).

Interestingly, some cell types require for efficient cell death that both pathways are activated. After activation of the extrinsic apoptosis pathway also the intrinsic pathway gets activated. Linking the two pathways, Caspase-8 cleaves and activates the BH3-only protein Bid which directly activates the initiators of intrinsic apoptosis BAK and BAX (H. Li, Zhu, Xu, & Yuan, 1998).

The Bcl-2 family proteins control the intrinsic apoptosis pathway by forming a highly complex interaction network (García-Sáez, 2012). Different models have been described to define their molecular mechanism: The ‘direct activation’, the ‘neutralization’, the ‘embedded together’, and the ‘unified’ models (Shamas-Din, Brahmbhatt, Leber, & Andrews, 2011).

The ‘direct activation’ model emphasizes that even though the sensitizer BH3-only proteins sequester the anti-apoptotic proteins, direct activation of the effector proteins BAK and BAX by the direct activator proteins is required for MOMP execution. This model suggests that the anti-apoptotic proteins primarily inhibit the direct activator proteins to prevent apoptosis. (E. H. Cheng et al., 2001; Moreau et al., 2003)

On contrary, the ‘neutralization’ model assumes that in healthy cells activated forms of the executor proteins BAK and BAX are constitutively active and inhibited by the anti-apoptotic family members. Upon apoptosis induction, the BH3-only proteins bind to and neutralize the anti-apoptotic proteins, “freeing” activated BAK and BAX which oligomerize and permeabilize the MOM. (Willis et al., 2005; Willis et al., 2007)

The ‘embedded together’ model highlights the importance of the mitochondrial outer membrane for the interaction and activation of BAK and BAX. It suggests that the anti-apoptotic proteins inhibit both the activator proteins as well as BAK and BAX under healthy conditions. Upon apoptotic stimulation, the sensitizer BH3-only proteins sequester the anti-apoptotic proteins leading to a competition between the activators and anti-apoptotic proteins for the binding of BAK and BAX. (Leber, Lin, & Andrews, 2007, 2010)

The ‘unified’ model combines the ideas of the previously described models and rates the efficiency of interactions between the anti-apoptotic Bcl-2 family members with pro-apoptotic ones. It suggests that the anti-apoptotic proteins bind and inhibit the BH3-only activators (MODE1) with lower efficiency than the executors BAK and BAX (MODE2). BAK and BAX in healthy cells are inactive and unbound while the direct activators are

sequestered (MODE1). Apoptosis induction results in a release of the BH3-only activators from the anti-apoptotic proteins and the activation of BAK and BAX. The BH3-only sensitizer proteins compete with the anti-apoptotic proteins for the interaction with BAK and BAX due to the higher interaction efficiency of MODE2. (Hockings et al., 2018; Llambi et al., 2011) Additionally, the retro-translocation of activated BAX from the mitochondrial membrane to the cytoplasm by anti-apoptotic members has been described (MODE0) (Edlich et al., 2011; Schellenberg et al., 2013; Westphal, Kluck, & Dewson, 2014).

The more recent 'interconnected hierarchical' model proposes a stepwise activation of BAK and BAX. In a first step, the effectors BAK and BAX are converted from an inactive form into active 'BH-3 exposed' monomers by the direct activators. In a subsequent step, the activators prevent the anti-apoptotic Bcl-2 family members from sequestering the 'BH3-exposed' BAK and BAX monomers, allowing them to homo-oligomerize. The anti-apoptotic Bcl-2 members inhibit both steps of the activation process: In a front-line protection, they inhibit the activators and as second line of defense they sequester the 'BH-3 exposed' BAK and BAX monomers. (H. C. Chen et al., 2015)

The 'integrated' model similar as the 'embedded together' model highlights the role of the membrane for the interactions between different Bcl-2 family members. In minimal model membrane systems Bleicken et al. demonstrated that Bcl-xL interacts with cBid in both solution and membrane, with the latter interaction being more stable. Only in the absence of cBid, Bcl-xL interacts with BAX in the membrane due to the lower affinity. Moreover, membrane bound BAX is able to recruit Bcl-xL from the cytoplasm and thereby promote retro-translocation of BAX from the membrane into the cytoplasm. (Bleicken, Hantusch, Das, Frickey, & Garcia-Saez, 2017)

The different affinities of the Bcl-2 family members towards each other increases the complexity of the interaction network. The direct activators and anti-apoptotic proteins possess different preferences for either BAK or BAX. For example, it has been reported that Bim preferentially activates BAX, while tBid preferentially activates BAK (Sarosiek et al., 2013). Furthermore, Mcl-1 preferentially sequesters BAK and Bcl-b BAX. In contrast, no preference for BAK or BAX was observed for Bcl-2, Bcl-xL, or Bcl-w. (Zhai, Jin, Huang, Satterthwait, & Reed, 2008) Additionally to the different preferences towards the effector molecules, not all BH3-only proteins interact with all anti-apoptotic proteins. The interaction of the BH3-only proteins with the anti-apoptotic proteins is specified by a unique binding profile which is defined by the peptide sequence of the BH3-domain of the BH3-only proteins and the hydrophobic groove of the anti-apoptotic proteins (Moldoveanu, Follis, Kriwacki, & Green, 2014). Here, for example, Noxa was reported to exclusively interact

with Mcl-1, Bad with Bcl-xL, Bcl-2 and Bcl-w, while Bid interacts with all anti-apoptotic proteins. (L. Chen et al., 2005) (Figure 1C)

In addition to their interaction with the other members of the Bcl-2 family, BAK and BAX interact with multiple MOM proteins. The voltage-dependent anion channel 2 (VDAC2), for example, has been shown to be critical for the regulation of BAK and BAX mitochondrial localization and apoptosis sensitivity. VDAC2 functions as molecular platform for the retro-translocation of BAX (Lauterwasser et al., 2016). It determines the specific localization of BAX to the MOM and regulates the levels of mitochondria-resident BAX. In healthy cells, BAX exists in a supramolecular complex with VDAC2 (Ma et al., 2014). However, it is unclear whether BAX interacts directly with VDAC2. VDAC2 is critical for BAX-driven apoptosis because loss of VDAC2 abolishes BAX-mediated apoptosis (Chin et al., 2018). Moreover, in VDAC2 deficient cells, the specific targeting of BAX to the mitochondria is lost and BAX associates with multiple organelles.

In contrast to BAX, VDAC2 has an inhibitory effect on BAK. Lack of VDAC2 exhibits enhanced BAK oligomerization and higher apoptosis susceptibility (Cheng, Sheiko, Fisher, Craigen, & Korsmeyer, 2003). In healthy cells, BAK is incorporated into a complex with VDAC2 and Metatxin 2 and kept in an inactive state. Upon apoptosis induction, BAK translocates from this complex and interacts with Metatxin 1. (Cartron, Petit, Bellot, Oliver, & Vallette, 2014)

BAK and BAX: Transformation from harmless monomers to oligomeric killers

BAK and BAX are the executors of MOMP, the crucial step in intrinsic apoptosis. The two executors share high sequence and structural homology and are considered to be redundant due to their compensatory effect after knockout of the other one (Youle & Strasser, 2008). Knockout mice of either BAK or BAX showed only mild defects while the majority of double knockout mice died perinatally. BAX knockout mice were viable with mild neuronal overgrowth and mild lymphoid hyperplasia but male mice were sterile. Severe defects in spermatogenesis occurred because of BAX-dependency. BAK knockout mice showed even less abnormalities and were fertile with normal tissue phenotype only showing increased numbers of platelets due to defects in platelet turnover. (Lindsten et al., 2000) Interestingly, age-dependent BAK expression in the brain was reported with high BAK levels in fetus and elderly subjects but no expression in young adults showing differential roles of BAK in development and aging of mice (Obonai, Mizuguchi, &

Takashima, 1998). The majority of mice with double knockout of BAK and BAX died perinatally with less than 10% of the mice surviving to adulthood. These mice show multiple phenotypical abnormalities including webbed paws, imperforated vaginas in female adults, bigger brains due to increased number of neurons in multiple brain areas, deafness and circling behavior, accumulation of lymphoid cells and splenomegaly. (Lindsten et al., 2000)

In their inactive form, BAK and BAX possess a globular structure comprising nine α-helices. The hydrophobic α5-helix in the core is surrounded and protected from the aqueous environment by a bundle of amphipathic α-helices. This Bcl-2 fold generates the hydrophobic groove, a surface motif that is composed of residues from α2-α5 and is required for interaction with the BH3-domain of other Bcl-2 proteins, for example during the activation by BH3-only proteins and dimer formation (Moldoveanu et al., 2006; Suzuki, Youle, & Tjandra, 2000). The C-terminal α9-helix is the transmembrane fragment that for BAK is inserted in the MOM. In contrast, for BAX the α9 is buried in the hydrophobic groove which leads to its cytoplasmic localization (Youle & Strasser, 2008). For the dimer formation, the BH3-domain in α2 inserts into the hydrophobic groove of another BAK or BAX molecule. In a non-activated state, the BH3-domain is hidden and gets exposed after interaction with a BH3-only activator protein (Kim et al., 2009; Walensky et al., 2006) (Figure 1B). Strikingly, structurally the pro-apoptotic BAK and BAX are similar to their anti-apoptotic counterparts and it is unclear why they differ functionally (Suzuki et al., 2000). For the inhibition, the BH3-domain of BAK and BAX is inserted into the groove of an anti-apoptotic protein.

For the efficient dimerization and oligomerization of BAK and BAX, they become activated by interaction with the direct activators. BAK and BAX differ in their initial step of activation because of the different localization of the proteins. For the activation, BAX first needs to be recruited to mitochondria (Wolter et al., 1997). The binding of a BH3-domain of a direct activator to a ‘rear’ activation site in α1 of BAX results in an exposure of the α9 and subsequently membrane insertion (Kim et al., 2009) (Figure 2A). The MOM-localized BAK constitutively exposes its α9 and bypasses this step. However, non-activated BAK is phosphorylated at several residues, most of them located in the hydrophobic groove, and requires partial dephosphorylation for its activation. The phosphorylations block the hydrophobic groove and prevent the binding of the BH3-domain of activator molecules or other BAK molecules. Dephosphorylation of Y108 and S117 has been reported to be critical for BAK activation. Y108 is highly conserved between species, located in α4 and solvent exposed. S117 is located in the BH1-domain in the hydrophobic groove. The dephosphorylation is the initial step of the activation and critical but not sufficient to activate

BAK. Therefore, dephosphoryated BAK is called ‘activation competent’ (Azad, Fox, Leverrier, & Storey, 2012; Fox et al., 2010).

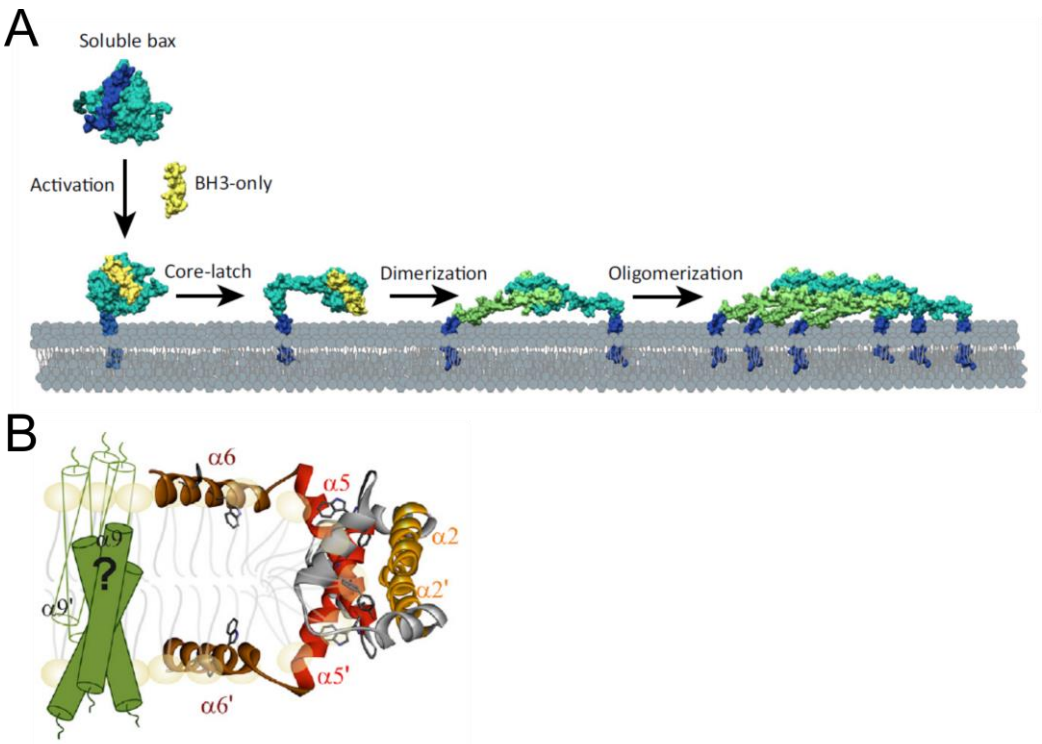

Figure 2: Transition of BAK and BAX from harmless monomers to deadly oligomers. *A) Scheme explaining the transition process of BAK and BAX from a monomer to a membrane permeabilizing oligomer. In the initial activation step of BAX, the BH3-domain of an activator molecule binds to its α1-helix triggering the release of the transmembrane helix from the hydrophobic groove and subsequent membrane insertion. BAK bypasses this step due to its mitochondrial localization. Afterwards, the BH3-domain of the activator transiently binds to the hydrophobic groove of BAK and BAX causing the separation into the ‘core’ (α2-α5) and ‘latch’ (α6-α8) domain. The BH3-domain of one BAK or BAX molecule inserts into the hydrophobic groove of another BAK or BAX molecule, respectively, forming a symmetric dimer. The dimers further assemble into oligomers by inter-dimer interactions. (adapted from (Peña-Blanco & García-Sáez, 2018)) B) BAX structure according to the ‘clamp’ model. The BAX dimer core lines the rim of the pore while the two α6-helices lying on the surface of the two membrane leaflets. The position of the α9-helices in the membrane is unknown. (adapted from (Bleicken et al., 2014))*

After α9 exposure or dephosphorylation, the hydrophobic face of the BH3-domain of an activator protein binds transiently within the hydrophobic groove of BAK or BAX (Gavathiotis et al., 2008; Lovell et al., 2008). For the interaction of the BH3-domain of tBid with BAK, four central residues within the groove has been described for the interaction resulting in a conformational change (Moldoveanu et al., 2013). The destabilization of the contacts between the BH1- and BH3-domain results in an opening of the occluded hydrophobic groove. Moreover, this interaction dissociates BAK and BAX into two domains, the ‘core’ (α2-α5) and the ‘latch’ (α-6-α8) domain by a partial opening of the α5-α6 hairpin. (Figure 2A) The ‘core’ domain is involved in dimerization, while the latch domain may play a role in membrane destabilization and piercing (Bleicken et al., 2014; Brouwer et al., 2014; Czabotar et al., 2013). In agreement with a ‘hit-and-run’ mechanism (Dai et

al., 2011), the activator BH3-domain within the hydrophobic groove gets subsequently replaced by the BH3-domain (α2) of another BAK/BAX molecule. The insertion of the exposed BH3-domain of BAK/BAX into the hydrophobic groove of another BAK/BAX molecule is a critical step of dimer formation (Bleicken et al., 2010; Czabotar et al., 2013; Dewson et al., 2008; Dewson et al., 2012). It results in the formation of symmetric dimers where the core domain of one BAK/BAX molecule interacts with the latch domain of the other. For the topology of the dimer in the membrane, different models have been proposed (Annis et al., 2005; Bleicken et al., 2014; Westphal, Dewson, et al., 2014). In the 'clamp' model the core of the dimer lines the rim of the pore with the two α6-helices lying on the surface of the two membrane leaflets parallel to each other (Bleicken et al., 2014) (Figure 2B).

The higher order oligomers are based on dimer units which assemble into a variety of oligomeric species opening toroidal pores of tunable size (Bleicken, Landeta, Landajuela, Basañez, & García-Sáez, 2013; Subburaj et al., 2015). The interdimer interactions have been reported to be weaker than intradimer interactions due to the fact that these interactions can be broken by 1% digitonin on a blue native page (Uren et al., 2017). Multiple interdimer interaction surfaces have been reported including for BAK oligomers, α6:α6 (Dewson et al., 2009) and α3:α5 (Mandal et al., 2016) interaction surfaces, suggesting the formation of disordered clusters (Uren et al., 2017). Toroidal pores of the size of a few to hundreds of nanometers allowing the release of 2MDa-dextran have been described (Gillies et al., 2015; Kuwana et al., 2002). The number of BAK and BAX molecules that are required to open a pore is unknown. Cryo-EM imaging of BAX in lipid nanodiscs showed that one BAX monomer might be sufficient to open a small pore of approximately 3.5 nm (Xu et al., 2013). This cryo-EM study as well as atomic force microscopy experiments of recombinant BAX on supported lipid bilayers visualized BAX pores that were not completely lined by BAX molecules reassure the toroidal pore model (Salvador-Gallego et al., 2016). In toroidal pores both proteins and lipids contribute to the pore wall. The lipids bend to avoid the exposure of the hydrophobic part to the aqueous environment creating a connection between the two leaflets with high membrane curvature. This high curvature at the membrane edge creates a high line tension that might be reduced by the clamp-like conformation of BAK and BAX stabilizing the opening of the pore. (Bleicken, Landeta, et al., 2013; Qian, Wang, Yang, & Huang, 2008)

Mitochondria in apoptosis

Mitochondria are intracellular organelles that form a highly dynamic network and are essential in almost all mammalian cells. They play pivotal roles in many physiological processes including oxidative phosphorylation and ATP synthesis (Saraste, 1999), the generation of iron-sulfur clusters and cofactors (Braymer & Lill, 2017), as well as in apoptosis (Desagher & Martinou, 2000). Mitochondria cannot be generated *de novo* and need to be transferred from mother to daughter cells. Due to their two membranes, the mitochondrial outer and inner membrane (MOM and MIM, respectively), the mitochondria are organized in four compartments (Perkins & Frey, 2000). The innermost, the matrix, contains the mitochondrial DNA (mtDNA). The mtDNA codes for 37 genes: 22 tRNAs, 2rRNAs and 13 proteins (Anderson et al., 1981). 99% of the mitochondrial proteome is encoded in the nuclear DNA and requires to be transported to and imported into the mitochondria (Bolender, Sickmann, Wagner, Meisinger, & Pfanner, 2008). The mitochondrial inner membrane (MIM) separates the matrix and the intermembrane space (IMS). It has a high protein to lipid ratio and is enriched in the lipid cardiolipin (Comte, Maïsterrena, & Gautheron, 1976). The MIM contains more than 150 different proteins, including proteins of the respiratory chain, the ATP-production, the import machinery and metabolite transporters. The MIM forms cristae invaginations that expand the surface of the MIM extremely and contain among others the assembled complexes of the respiratory chain (Mannella, 2006). The narrow openings of the cristae, the cristae junctions, sequester its content and enable a controlled transfer of substrates between the cristae and the IMS. The MIM is highly impermeable only allowing transport through selective channels and generates thereby a membrane potential between the matrix and the IMS that is essential for the proper mitochondrial function and ATP generation. The MOM, on the contrary, is highly permeable due to porins of the VDAC family. (Comte et al., 1976)

The mitochondrial network undergoes continuously fusion and fission events depending on the cell cycle, energy state and cellular health (Hoppins, Lackner, & Nunnari, 2007). These processes are mediated by a group of large GTPases. Mitochondrial fission requires the dynamin-related protein 1 (Drp1) which is recruited to the division sites on the MOM by several adaptor proteins including Mff and MID49/51 (Osellame et al., 2016). Interestingly, specialized endoplasmic reticulum (ER) tubules seem to be required to mark and preconstrict the division sites at mitochondria (Friedman et al., 2011). Drp1 is thought to organize into spiral supramolecular complexes, wrapping around a mitochondrion, constricting it by its GTPase activity and finally executing the scission of mitochondria suggesting a multi-step process involving the ER, Drp1 and microtubules (Kamerkar, Kraus, Sharpe, Pucadyil, & Ryan, 2018).

Mitochondrial outer membrane fusion is executed by Mitofusin1 and 2 (Mfn1 and 2), while the fusion of the inner membrane is executed by optic atrophy 1 (OPA1) (Pernas & Scorrano, 2016). Mnf1 and Mfn2 have a high sequence identity and contain a N-terminal GTPase domain required for the fusion, a transmembrane domain for MOM insertion and two predicted heptad repeats that might mediate the tethering of two adjacent mitochondria (Cohen & Tareste, 2018). However, the structure as well as the mechanism of fusion is not solved yet. In addition, it is unclear whether or how the fusion of the MOM and MIM are coordinated. OPA1, the executor of MIM fusion, is located at the MIM with the GTPase domain facing the IMS and exists in multiple long and short isoforms. In addition to its MIM fusion function, OPA1 has been linked to the remodeling of the cristae morphology (Cipolat, Martins de Brito, Dal Zilio, & Scorrano, 2004).

In apoptosis, mitochondria undergo several reorganization processes: extensive fragmentation, mitochondrial outer membrane permeabilization, the loss of the membrane potential and cristae remodeling (Sun et al., 2007). The fragmentation of mitochondria is a universal early event in intrinsic apoptosis. However, the link between apoptosis and mitochondrial fragmentation is insufficiently understood. It is executed by Drp1 that is massively recruited and stabilized on mitochondria under apoptotic conditions (Frank et al., 2001). Drp1 has been found to colocalize in apoptotic foci together with BAK and BAX (Karbowski et al., 2002) and gets stabilized on the MOM during apoptosis by a BAK/BAX-promoted sumoylation via MAPL (Prudent et al., 2015; Wasiak, Zunino, & McBride, 2007). Knockout of Drp1 restricted apoptotic mitochondria fragmentation and delayed but not prevented apoptosis progression, demonstrating that fragmentation and apoptosis can be uncoupled (Oettinghaus et al., 2016; Sheridan, Delivani, Cullen, & Martin, 2008). It was suggested that the mitochondria division sites by Drp1 provide favored oligomerization sites for BAK and BAX with high membrane curvature and optimal lipid mixture (Karbowski et al., 2002). BAK and BAX foci at the tips of mitochondria and in assigned division sites by ER tubules in Drp1 knockout cells supported this assumption (Bleicken, Hofhaus, Ugarte-Uribe, Schröder, & García-Sáez, 2016; Montessuit et al., 2010). In addition to the interaction of BAK and BAX with Drp1, it has also been reported that they interact with the fusion proteins Mfn1 and Mfn2. Immunoprecipitation demonstrated the interaction of BAK with Mfn1 and Mfn2 and BAX with Mfn2 (Brooks et al., 2007; Cleland et al., 2011). Furthermore, under healthy conditions BAX stimulates Mfn2-dependent membrane fusion, however, membrane-bound activated BAX loses the ability to stimulate fusion suggesting that activation of BAX probably inhibits fusion events (Hoppins et al., 2011).

The permeabilization of the MOM by BAK and BAX causes the release of pro-apoptotic factors like Smac/DIABLO and cytochrome *c* from the IMS of mitochondria into the

cytoplasm (Goldstein, Waterhouse, Juin, Evan, & Green, 2000). Cytochrome *c* exists in two populations: a minor population is free in the IMS but the major population, approximately 85%, is trapped in the cristae (Scorrano et al., 2002). While the cytochrome *c* in the IMS is sufficient for apoptosis progression, an efficient release of cytochrome *c* requires the remodeling and opening of the cristae. Disassembly of OPA1 oligomers results in an opening of the cristae junction and efficient release of cytochrome *c (Yamaguchi et al., 2008)*. Interestingly, Drp1 seems to be required for cristae remodeling. Knockout of Drp1 results in delayed and incomplete release of cytochrome *c* while IMS-located Smac/DIABLO was fully released (Große et al., 2016; Oettinghaus et al., 2016). Moreover, it has been suggested that apoptosis-related cristae remodeling might be independent of OPA1 and mediated by Drp1 and its adaptor MID49/51 (Otera, Miyata, Kuge, & Mihara, 2016).

Additionally, in 2018 it has been proposed that BAK and BAX pores not only permeabilize the MOM but also lead to MIM permeabilization by yet unknown mechanisms. The permeabilization of the MIM allows the release of the mtDNA from the matrix enabling the activation of the cGAS-STING pathway and an inflammatory cell death under caspase deficient conditions. (McArthur et al., 2018; Riley et al., 2018; Rongvaux et al., 2014; White et al., 2014)

Mitochondria-ER membrane contact sites

The compartmentation into membrane-bound organelles enables eukaryotic cells to generate different reaction compartments and to distribute tasks. However, for optimal cell function the different organelles need to communicate and transfer substrates. This communication and transfer are achieved by vesicular transport and by membrane contact site between two organelles. One of the best characterized contact sites are the mitochondria-ER membrane contact sites (MERCs). The MERCs are important for many pivotal cellular processes including calcium homeostasis and signaling (Rizzuto et al., 1998), lipid biosynthesis (Vance, 2014; Voelker, 2005), autophagy (Hamasaki et al., 2013), mitochondrial morphology (Friedman et al., 2011; Phillips & Voeltz, 2016) and apoptosis (Grimm, 2012; Pinton, Giorgi, Siviero, Zecchini, & Rizzuto, 2008). In addition, alteration in MERCs seems to be connected with several human diseases such as cancer (Kerkhofs et al., 2017; Morciano et al., 2018), metabolic (Rieusset, 2018; Tubbs & Rieusset, 2017) and neurodegenerative diseases (Area-Gomez & Schon, 2016; Paillusson et al., 2016).

The endoplasmic reticulum

The endoplasmic reticulum (ER) is an organelle that consists of one highly dynamic inter-connected network. The ER forms one continuous membrane system that includes the outer nuclear envelop and the peripheral ER network that spans the whole cell. It is organized in tubular and sheet structures, known as cisternae (Schwarz & Blower, 2016; Shibata, Voeltz, & Rapoport, 2006). This structures are shaped and preserved by proteins and the microtubule cytoskeleton (Y. Du, Ferro-Novick, & Novick, 2004). However, how different cellular signals coordinate changes in the ER structure is still elusive. The ER sheets are flat structures of two lipid membranes with an interjacent lumen only possessing curved regions on the edges. Even though, the sheets vary in size the luminal thickness is consistent with approximately 50 nm (Bernales, McDonald, & Walter, 2006). The sheets often organize in stacks that are connected via twisted helical membrane regions. They are covered by ribosomes and termed the ‘rough ER’. The rough ER functions as site for the biosynthesis and post-translational modifications of proteins (West, Zurek, Hoenger, & Voeltz, 2011). The docking of the ribosomes to the ER membrane enables co-translational insertion of integral proteins into the ER membrane. (Jan, Williams, & Weissman, 2014) The tubular structures, in contrast, are not covered by ribosomes and are termed the ‘smooth ER’. The ER tubules have a high membrane curvature and are involved in lipid, steroid and steroid hormone biosynthesis. In addition, the ER functions as major calcium

storage in the cell with a calcium concentration of 100-800 µM. (Fagone & Jackowski, 2009; Hu, Prinz, & Rapoport, 2011)

The structure and proteins of the MERCs

The MERCs, the sites of contact between mitochondria and the ER, were first observed in 1969 by Ruby et al. using electron microscopy (Ruby, Dyer, & Skalko, 1969). However, for a long time these contact sites were considered to be fixation artifacts. First, in 1990 the MERCs were discovered as biochemical entities. Vance et al. purified an ER-like membrane fraction that was highly associated with mitochondria (Vance, 1990). MERCs are subdomains of the ER membrane that physically interact with the mitochondrial outer membrane (MOM). A distance of 10-20 nm between the MOM and the smooth ER and 20-35 nm between the MOM and the rough ER was measured. Moreover, 3D-reconstructions using electron tomography showed that only small areas of the ER approximately 5-20% are in close contact with mitochondria (Csordás et al., 2006; Mannella, Buttle, Rath, & Marko, 1998). The MERCs are dynamic and vary in their number, the distance between the organelles and the contact area depending on the cellular state. Protein tethers are required for the stability of the MERCs (Csordás et al., 2006) and they remain tethered even during the movement of mitochondria along the microtubule network (Korobova, Ramabhadran, & Higgs, 2013; Manor et al., 2015). Furthermore, proteomic studies identified more than 1000 different proteins that are located at MERCs (Hung et al., 2017; Poston, Duong, Cao, & Bazemore-Walker, 2011; Sala-Vila et al., 2016). However, the characterization of the MERCs proteome proves to be challenging due to the difficulty to isolate pure MERCs and to changes in the protein composition of the MERCs depending on cellular state. MERCs have been shown to be enriched in proteins of the lipid biosynthesis and transport compared to the bulk ER (Vance, 2014).

In yeast, the ERMES (Endoplasmic Reticulum-Mitochondria Encounter Structure) complex has been described as the proteinaceous tether of MERCs. The ERMES-complex is composed of the mitochondrial proteins Mdm10 and Mmm2, the integral ER-membrane protein Mmm1 and the cytosolic protein Mdm12 (Kornmann et al., 2009; Kornmann & Walter, 2010) (Figure 3A). This tether seems to be involved in the biosynthesis and transport of phospholipids and in calcium homeostasis. Knockout of one of the ERMES components results in uncoupling of the membranes, impaired phospholipid metabolism and calcium transport (Kawano et al., 2018). In mammalian cells, however, no homologous complex was found and several proteins have been described to be involved in the tethering and the regulation of MERCs tethering.

Interestingly, in 2017 Hirabayashi et al. reported that the ER protein PDZD8 acts as a MERCs tether (Hirabayashi et al., 2017). It contains a SMP domain with a high structural correspondence to that of Mdm12 and Mmm1, two components of the ERMES complex. Mouse PDZD8 and Mmm1 containing the SMP domain of PDZD8 failed to rescue the defects in mitochondrial morphology, mitochondrial inheritance and loss of mtDNA of Mmm1 deficient yeast cells. Mmm1 containing a chimeric SMP domain of PDZD8 and Mmm1 partially recovered the defects indicating that the PDZD8 SMP domain is functionally orthologous to the SMP domain of yeast Mmm1. In mammalian cells, PDZD8 seems to be critical for proper calcium transfer from ER to mitochondria, especially in neuronal synapses. Knockout of PDZD8 not only causes an uncoupling of MERCs but also an impaired transfer of calcium (Hirabayashi et al., 2017) (Figure 3A).

Mitofusin 2 (Mfn2) was the first protein that was suggested as a proteinaceous MERCs tether in mammals. Mfn2 is present on the MOM as well as on the ER-membrane and was proposed to form homo- and heterotypic dimers with MOM-resident Mfn1 and Mfn2 (Eura, Ishihara, Yokota, & Mihara, 2003) (Figure 3A). Even though the involvement of Mfn2 in MERCs is accepted, its role is still under debate. First, Mfn2 was described as a tether because of the fact that knockout of Mfn2 resulted in a decreased co-localization of the ER with the mitochondria by confocal microscopy, decreased contamination of the mitochondrial fraction with ER and decreased transfer of ER calcium to mitochondria (de Brito & Scorrano, 2008; Naon et al., 2016). However, several electron microscopy studies revealed that the knockout of Mfn2 caused a stronger coupling of the ER with mitochondria. The Mfn2 knockout cells showed an increased number of contacts and a closer distance between the organelles. Due to these findings, Mfn2 was proposed to act as a spacer between the ER and mitochondria, keeping them at the correct distance (Cosson, Marchetti, Ravazzola, & Orci, 2012; Filadi et al., 2015; Leal et al., 2016). This model was reassured by more recent studies using a split-GFP-based reporter which showed a higher number of contact sites in Mfn2 knockout cells (Harmon, Larkman, Hardingham, Jackson, & Skehel, 2017). Up to date, the role of Mfn2 in MERCs is still intensely debated. In addition, multiple proteins have been reported to modulate the contacts mediated by Mfn2 including Trichoplein/mitostatin (TpMs) (Cerqua et al., 2010) and the ubiquitin ligases MITOL (Sugiura et al., 2013) and Parkin (Basso et al., 2018).

In addition to structurally linking the ER with mitochondria, many MERCs tethering or regulating proteins have been proposed to connect their structural role with function. For example, calcium transfer from the ER to mitochondria is required for the fine tuning of many mitochondrial metabolic processes (McCormack, Halestrap, & Denton, 1990). It appears that this calcium transfer occurs via the MERCs. IP_3R, a ER-resident calcium

receptor, is stabilized at the MERCs by sigma-1 (Hayashi & Su, 2007) and is physically linked with the mitochondrial voltage-dependent anion channel 1 (VDAC1) by the molecular chaperone grp75 to ensure proper calcium transport (Szabadkai et al., 2006) (Figure 3A, B). PERK, a key senor for ER stress by unfolded protein response (UPR), is enriched at the MERCs and mediates ROS-dependent ER stress and sensitizes for intrinsic apoptosis via the contact sites. It has been reported that PERK deficient cells display weaker MERCs, disrupted ER morphology, impaired calcium signaling and less sensitivity to intrinsic apoptosis (Verfaillie et al., 2012). In addition, Mfn2 might act as an upstream regulator of PERK (Muñoz et al., 2013).

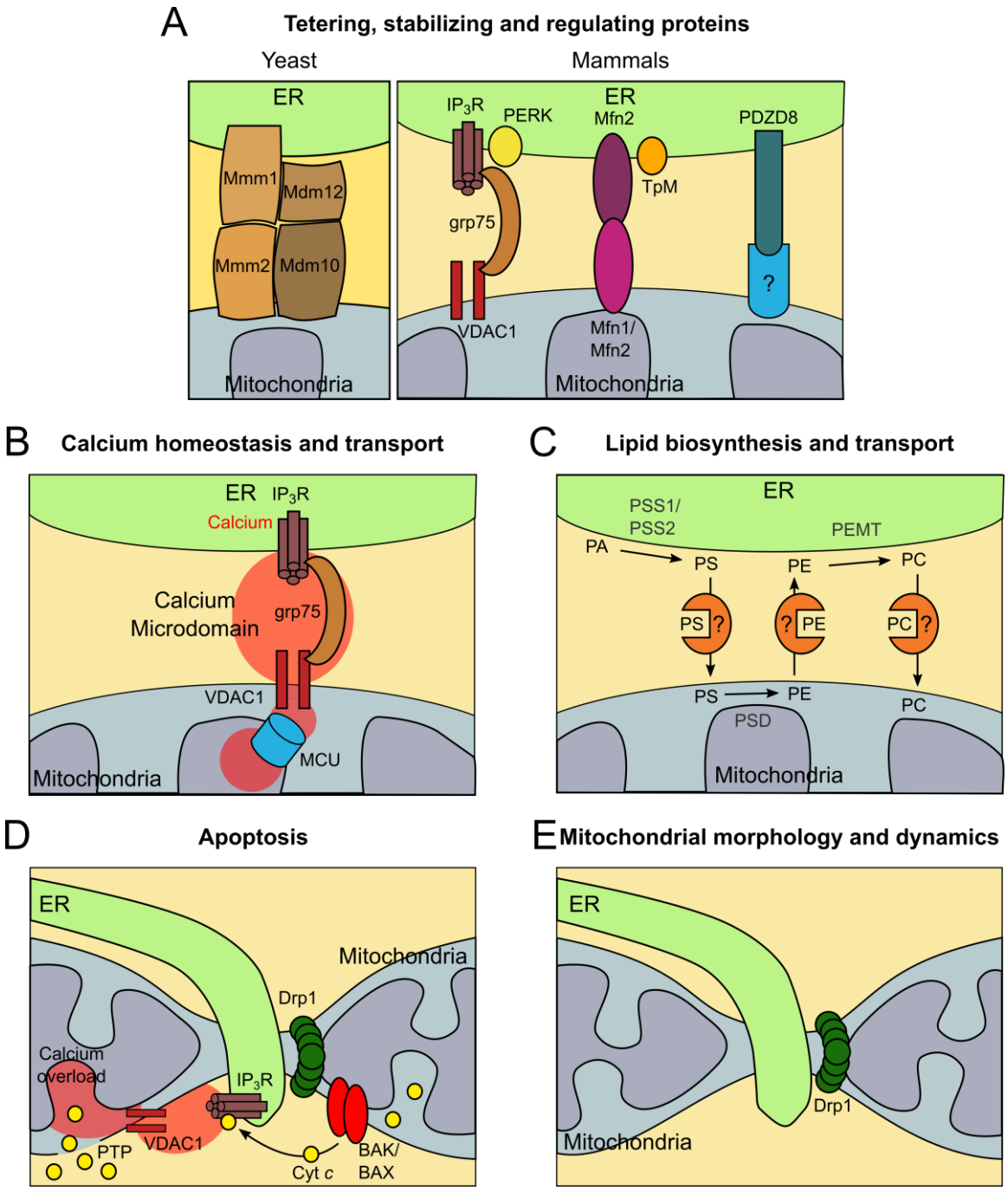

Figure 3: MERCs tethering and regulating proteins and physiological processes at MERCs. (previous page) *A) In yeast, the ERMES complex composed of the mitochondrial outer membrane proteins Mdm10 and Mmm2, the ER-resident protein Mmm1 and the cytoplasmic protein Mdm12 acts as a tethering complex of MERCs. In mammals, multiple proteins have been described to be involved in the tethering and regulation of the MERCs including grp75 that physically links the ER calcium receptor IP_3R and the mitochondrial VDAC1, ER-resident Mfn2 that interacts with mitochondrial Mfn1 or Mfn2, or the ER-resident PDZD8, whose mitochondrial counterpart is not identified yet. B) MERCs facilitate the transfer of ER calcium to mitochondria by generating calcium microdomains with high concentration. The ER calcium receptors release calcium which is taken up by the mitochondrial calcium uniporter (MCU) to fine tune mitochondrial processes. C) MERCs act as a platform for phospholipid biosynthesis and transfer between the two organelles. Phosphatidylserine (PS) is generated at the ER membrane and transferred to mitochondria where the decarboxylation to phosphatidylethanolamine (PE) is catalysed. PE is transferred back to the ER for further catalysis into phosphatidylcholine (PC). D) MERCs are involved in apoptotic cell death. Specialized ER tubules marking mitochondrial fission sites for the dramatic fragmentation occurring during the apoptotic process. Thereby, the ER might generate favourable sites for BAK and BAX assembly. Moreover, the released cytochrome c binds to IP_3R which releases calcium and thereby amplifies the apoptotic signal. Calcium overload of mitochondria might result in the opening of the permeability transition pore (PTP). E) Specialized ER tubules assist with mitochondrial fission. The ER tubules mark and preconstrict division sites by wrapping around mitochondria. Drp1 might be recruited to this site by its adaptor protein Mff, where it forms oligomers and mediates mitochondrial fission.*

Functions of MERCs

The contact sites between the ER and mitochondria are distinct domains that facilitate the communication and substrate transfer between these two crucial organelles. They are involved in multiple critical functions in the cell including calcium transport and homeostasis, lipid biosynthesis and transport, autophagy, inflammasome formation, mitochondria morphology and apoptosis. Here, I briefly highlight the involvement of MERCs in the lipid biosynthesis and transport, the calcium homeostasis and apoptosis.

In the 1990s Vance and coworkers discovered that MERCs are important platforms for the biosynthesis and transport of phospholipids (Vance, 1990). Enzymes involved in lipid biosynthesis like phosphatidylethanolamine N-methyltransferase 2 (PEMT2) (Cui, Vance, Chen, Voelker, & Vance, 1993), diacylglycerol acyltransferase (DGAT2) (Stone et al., 2009) and long-chain fatty acid CoA ligase 4 (FALC4) (Lewin, Kim, Granger, Vance, & Coleman, 2001) are enriched and phosphatidylserine synthase (PSS) is exclusively located at MERCs (Stone & Vance, 2000). The majority of phospholipids are synthesized in the ER. Phosphatidylethanolamine (PE), however, is mainly generated in mitochondria by the enzyme phosphatidylserine decarboxylase (PSD) that catalyzes the decarboxylation of phosphatidylserine (PS) (Shiao, Lupo, & Vance, 1995; Voelker, 2003). For the production of PE, the precursor PS needs to be transported from the ER to mitochondria. This transport is assumed to occur at MERCs since decoupling of the MERCs results in a decreased transfer of PS from the ER to mitochondria which is the rate limiting step in the production of PE (Kawano et al., 2018; Voelker, 1989). Moreover, impaired contact sites have been reported to modify the phospholipid composition of mitochondria (Kornmann et al., 2009). (Figure 3C)

The ER is the major calcium storage of the cell. The calcium concentration of the ER varies between 100-800 µM and is considerably higher than in the cytoplasm (10-100 nM) (Pozzan, Rizzuto, Volpe, & Meldolesi, 1994). Mitochondria in the resting state have a similar calcium concentration as the cytoplasm but upon stimulation the calcium concentration is able to increase by 100-fold (Bonora et al., 2013; Somlyo, Bond, & Somlyo, 1985). Multiple mitochondrial enzymes are activated or fine-tuned by calcium. For example, calcium directly activates the enzymes isocitrate dehydrogenase, α-ketoglutarate dehydrogenase and the enzyme pyruvate dehydrogenase is activated by a calcium dependent dephosphorylation (Cárdenas et al., 2010; Denton, 2009). As previously mentioned, the transfer of calcium from the ER to mitochondria is mediated by the ER calcium receptor IP_3R that is physically linked to VDAC1 at the MOM by grp75 at MERCs (Szabadkai et al., 2006). The uptake of calcium into the matrix of mitochondria is executed by the mitochondrial calcium uniporter (MCU) (Baughman et al., 2011; Kirichok, Krapivinsky, & Clapham, 2004). It has been demonstrated that the MCU possesses a relatively low affinity for calcium and that for efficient uptake microdomains with high calcium concentrations are generated (Csordás et al., 2010; Rizzuto, Brini, Murgia, & Pozzan, 1993). (Figure 3B)

Calcium is not only required for physiological processes but also to modulate cell death. Extensive transfer of calcium to mitochondria is highly toxic and can result in overload. Overload with calcium was first associated with necrotic cell death. Calcium triggered massive activation of proteases and phospholipases, swollen mitochondria and loss of cell integrity. (Pinton et al., 2008) Later, it was proposed that milder, more controlled increased calcium levels can also initiate mitochondrial apoptosis (Csordás et al., 2006; Szalai, Krishnamurthy, & Hajnóczky, 1999). The calcium signaling seems to be involved in early and late stages of apoptosis. Several proteins of the Bcl-2 family have been reported to modulate calcium transfer, including Bcl-2 and Bcl-xL, or initiating ER-stress induced apoptosis (Bravo et al., 2011; Lewis, Hayashi, Su, & Betenbaugh, 2014; Williams et al., 2016). Bcl-2 seems to modulate calcium levels since overexpression of Bcl-2 resulted in decreased ER calcium levels and calcium transfer to mitochondria in resting state and after apoptosis stimulation (Murphy, Bredesen, Cortopassi, Wang, & Fiskum, 1996; Pinton et al., 2000). Moreover, double knockout of the pro-apoptotic Bcl-2 family members BAK and BAX showed a reduction in the ER calcium levels. In contrast, overexpression of BAX causes initially an increase in ER calcium levels and calcium transfer but the normal levels were restored over time (Nutt et al., 2002; Oakes et al., 2005; Scorrano et al., 2003). Calcium overload in mitochondria might open the permeability transition pore (PTP) in the MOM which allows the release of pro-apoptotic factors like cytochrome *c* from the

intermembrane space and subsequently caspase activation and cell death (Crompton, 1999; Hurst, Hoek, & Sheu, 2017). Cytochrome c has been shown to bind to and activate the ER calcium receptor IP_3R and thereby amplify the apoptotic signaling by calcium (Boehning et al., 2003). (Figure 3D) This function of cytochrome *c* also enables additional apoptotic signal amplification by calcium even for calcium independent apoptosis forms. In contrast, Caspase-3 might limit the calcium signaling and stop the amplification by inactivating the IP_3R (Hirota, Furuichi, & Mikoshiba, 1999). In addition to the Bcl-2 family members, several other proteins have been proposed to modulate calcium levels to initiate intrinsic apoptosis. For example, the promyelocytic leukemia (PML) tumor suppressor that is frequently lost in solid tumors and hematopoietic malignancies has been shown to be a modulator of apoptosis. PML knockout protects against apoptosis triggered by multiple stimuli. PML is enriched at MERCs and induces apoptosis via calcium transfer from the ER to mitochondria (Giorgi et al., 2010).

In addition to inducing the apoptotic signaling, high calcium levels, higher than 1 µM, have been shown to tighten MERCs and reduce the movement of mitochondria (Yi, Weaver, & Hajnóczky, 2004). The number of MERCs is increased and the distance between the organelles is decreased under apoptotic conditions (Csordás et al., 2006). Furthermore, MERCs not only modulate apoptosis by calcium transfer but also by generating favorable sites for BAK and BAX oligomerization and optimal lipid mixture. Extensive fragmentation of mitochondria is an early step of apoptosis (Ugarte-Uribe & García-Sáez, 2014). It has been demonstrated that specialized ER tubules mark the division sites by wrapping around mitochondria (Friedman et al., 2011). (Figure 3D, E) These division sites provide a high membrane curvature which might provide favorable sites for BAK and BAX oligomerization. This assumption was reinforced by the finding that many BAK and BAX foci are formed at the tip of mitochondria. Moreover, the close apposition at MERCs might enable lipid exchange between the ER and mitochondria that generates an optimal lipid mixture for BAK and BAX assembly (Cosentino & García-Sáez, 2014).

Methodology for MERCs investigation

Multiple techniques have been used for the structural, biochemical and functional investigation of MERCs. Here, I highlight some of these techniques and discuss their advantages, drawbacks and limitations.

Electron microscopy was the first method used to investigate the MERCs (Ruby et al., 1969). It offers the highest possible resolution of the available microscopy techniques. With a resolution up to approximately 0.2 nm electron microscopy enables the imaging of the organelles and MERCs structure, as well as the number and distance of MERCs (Collado

& Fernández-Busnadiego, 2017). In addition, the more recent electron tomography allows 3D-reconstruction of the mitochondrial and ER network and provides three-dimensional structural information of MERCs (Csordás et al., 2006; Perkins et al., 2010). Electron microscopy provides the advantage of quantitative analysis of MERCs and comparisons between different cell types and treatments. However, it is time consuming and the fixation, dehydration and staining generates artifacts and prohibits live-cell imaging. Thereby, electron microscopy is unable to provide dynamic live cell data.

Fluorescence microscopy, on the contrary, enables the imaging of dynamic processes in live cells. However, due to the diffraction of light the resolution is limited to approximately 200 nm. Thereby, fluorescence microscopy is not able to provide structural information of MERCs. Fluorescence and confocal microscopy are often used to study the morphology of mitochondria and the ER network and estimate the area or volume of contact using co-localization algorithms like Pearson's correlation and Mander's overlap coefficient (Dunn, Kamocka, & McDonald, 2011; Marchi, Bonora, Patergnani, Giorgi, & Pinton, 2017). This analysis usually provides results that are in agreement with structural information obtained with EM. However, in some cases due to morphological changes of the ER or mitochondria, like fragmentation, there are discrepancies. One example is the opposite results that were obtained for Mfn2 knockout cells. While fluorescence microscopy showed a higher contact area after knockout, electron microscopy obtained the opposite. These results led to the two different hypotheses about the Mfn2 functions. The results of the fluorescence microscopy indicated a tethering function for Mfn2 while electron microscopy results suggested an antagonizing, spacer, function of Mfn2 (de Brito & Scorrano, 2008; Filadi et al., 2015).

Additionally, multiple fluorescent microscopy-based methods have been developed including proximity ligation assays (PLA), dimerization-dependent ddGFP, FRET-based and splitGFP approaches (Huang, Jiang, Yu, & Yang, 2020).

PLA depends on highly specific primary antibodies for mitochondria and the ER and requires fixation of the sample. Comparable protein expression levels have been shown to be critical for reliable results (Fredriksson et al., 2002; Tubbs & Rieusset, 2016). One of the first FRET-based approaches was described by Csordás et al (Csordás et al., 2010). They demonstrated the existence of MERCs in live cells with their generated bifunctional linkers targeted either to the ER membrane or the MOM containing a CFP/YFP FRET-pair and a FKBP/FRP heterodimerization system. The interaction between the two linkers was induced using rapamycin. While this system allowed live cell analysis of the MERCs structure, the difficulty to quantify FRET results, the forced interaction between the

organelles by rapamycin and the use of the drug rapamycin itself that was reported to induce autophagy were several drawbacks.

More recently, a splitGFP reporter was described for the analysis of MERCs. For the splitGFP reporter, the two non-fluorescent GFP parts, GFP1-10 and GFP11, are anchored to the ER membrane or MOM, respectively. Only if they assemble together they form a fluorescent protein that can be used for the visualization of the number and extension of the MERCs (Pinaud & Dahan, 2011; Yang, Zhao, Xu, Shang, & Tong, 2018). The addition of a short and long linker to these reporters allows the analysis of the abundance of different MERCs. For example, using this approach Domenico Cieri et al. showed that Mfn2 knockdown causes an approximately 40% increase of short-range MERCs (8-10 nm) while the long-range MERCs (40-50 nm) were decreased by approximately 30% (Cieri et al., 2018). The splitGFP reporter offered multifaceted possibilities for the investigation of MERCs in live cell using confocal microscopy. However, disadvantages of this approach are the irreversibility of the GFP complementation that might also force the interaction and the limited resolution of fluorescent microscopy that might complicate the analysis (Pedelacq & Cabantous, 2019).

In addition to microscopic approaches that mainly describe the structural properties of MERCs, also biochemical or functional studies were used for the characterization. Fractionation of the different compartments using ultracentrifugation were used to purify MERCs form mitochondrial and ER fractions (Vance, 1990; Wieckowski, Giorgi, Lebiedzinska, Duszynski, & Pinton, 2009). However, due to the tight association the pure isolation of MERCs proved to be challenging. The isolation of MERCs was often combined with subsequent mass spectrometry to identify the proteome (Hung et al., 2017; Poston et al., 2011; Sala-Vila et al., 2016). However, the protein composition of MERCs varied because of changes in the MERCs during cell cycle or cellular stress. For the functional investigation, the calcium transfer between the ER and mitochondria was regularly measured using genetically encoded calcium indicators, calcium probes or chemical dyes (Samtleben et al., 2013; Whitaker, 2010).

Objectives

CHAPTER 2:

BAK and BAX are the executors of the mitochondrial outer membrane permeabilization (MOMP), the crucial step of the intrinsic apoptosis pathway. The oligomerization of BAK and BAX on the mitochondrial outer membrane causes its permeabilization and subsequent cell death. The MOMP is considered as the point-of-no-return. Therefore, it is critical to understand the mechanism underlying the BAK and BAX oligomerization and pore formation.

The aim of this chapter was to **investigate the architecture and kinetics of BAK apoptotic foci and to compare them to its homolog BAX to study whether BAK and BAX follow the same molecular mechanism.**

The goals of this chapter were:

1) Analyze the structure of BAK apoptotic foci using super-resolution microscopy
    - Characterize the structures of BAK foci and their properties
    - Investigate temporal development of BAK structures during apoptosis progression
    - Compare the characterized structures of BAK to the ones described for BAX previously
    - Study the influence of endogenous BAX on BAK assemblies

2) Analyze the functional consequences of the differences between BAK and BAX assemblies
    - Investigate the difference in completeness and kinetics of mtDNA release for BAK or BAX deficient conditions

CHAPTER 3:

Mitochondria-ER membrane contact sites (MERCs) are distinct subdomains of close apposition between the mitochondrial outer membrane and the ER membrane that act as platforms for pivotal cellular processes including lipid biosynthesis and transport, calcium homeostasis, mitochondrial morphology and apoptosis. Multiple investigation methods have been used to structurally, functionally or biochemically characterize MERCs.

We aimed to **develop a novel BRET-based biosensor (MERLIN) for the investigation of MERCs that only relies on proximity and does not establish the formation of physical links between the two organelles and therefore enables the study of MERCs dynamics and molecular composition.**

The goals of this chapter were:

1) Optimize MERLIN systematically
   - Verified the correct targeting of the biosensors and the negligible effect of MERLIN expression on cell viability and MERCs
   - Systematically test for MERLIN functionality and optimal linker length

2) Validate MERLIN by conditions or treatments known to affect the MERCs
   - Test for MERCs changes in apoptotic cells or in cells after drug treatments known to affect MERCs
   - Study MERCs changes after knockdown or overexpression of the known tether PDZD8 or after addition of an artificial tether

3) Demonstrate the applicability of MERLIN
   - Study MERCs in single-cells using FLIM-FRET with a FRET biosensor based on the MERLIN design
   - Investigate the dynamics and reversibility of MERCs after the addition of different treatments
   - Investigate the role of the mitochondrial machinery on MERCs

CHAPTER 2.

BAK assembles into smaller yet functional pores than BAX

Authors

Vanessa Hertlein[1], Katia Cosentino[1,2], Andreas Jenner[1,3], John Danial[1], Markus Mund[4], Jonas Ries[4], Ana J. García-Sáez[1,3]

[1] Interfaculty Institute of Biochemistry, University of Tübingen, Tübingen, Germany

[2] Department of Biology and Center for Cellular Nanoanalytics (CellNanOs), University of Osnabrück, Germany

[3] Institute for Genetics and Cologne Excellence Cluster on Cellular Stress responses in Aging-Associated Diseases (CECAD), Cologne, Germany

[4] European Molecular Biology Laboratory, Heidelberg, Germany

Authors Contribution

Vanessa Hertlein performed experiments and analyzed data (except stoichiometry analysis, atomic force microscopy and GUV assays). Katia Cosentino performed and analyzed data of atomic force microscopy. Katia Cosentino and Andreas Jenner performed and analyzed data of the stoichiometry analysis and GUV assays. John Danial and Markus Mund assisted with dSTORM imaging. Jonas Ries provided material and supervised dSTORM imaging. Vanessa Hertlein wrote this thesis chapter. Ana J. García-Sáez conceived the project and supervised the research.

RESULTS

BAK and BAX execute the pivotal step during intrinsic apoptosis, the permeabilization of the mitochondrial outer membrane. The oligomerization of BAK and BAX leads to pore formation in the mitochondrial outer membrane and eventually cell death. However, the underlying mechanism of BAK oligomerization and the architecture of the pores it forms are not well understood. Here, we investigated the spatial organization of BAK at the nanoscale and the kinetics of BAK foci formation in apoptotic cells using single-molecule localization microscopy, atomic force microscopy and stoichiometric analysis. We show that, in apoptotic cells, BAK assembles into distinct structures including rings, arcs and lines. The architecture of these structures is similar to those formed by BAX. Interestingly, however, the structures formed by BAK are smaller and more uniform than those of Bax and the kinetics of BAK foci formation is faster indicating a difference in the mechanism of oligomerization. Furthermore, we observed a reciprocal contribution of BAK and BAX towards each other's assembly. The presence of BAK accelerates the kinetics of BAX pore formation. On the contrary, BAX presence slows down BAK foci formation and increases the foci size slightly. In agreement with the faster kinetics of BAK foci formation, BAK foci enable a faster release of mitochondrial DNA upon mitochondrial permeabilization.

BAK assembles into distinct structures in apoptotic cells

For apoptosis execution, BAK needs to be activated and to oligomerize in order to permeabilize the mitochondrial outer membrane. Using confocal microscopy, we showed that BAK in healthy cells is homogeneously distributed at the mitochondrial network. Upon apoptosis induction, BAK re-organized into foci, which correlated in time with Smac release from mitochondria. (Figure 4A, B). However, the resolution of confocal microscopy is not sufficient to resolve the structural organization of the BAK apoptotic foci. To overcome the diffraction limit of light and achieve higher resolution imaging we used the super-resolution microscopy technique dSTORM (direct Stochastic Optical Reconstruction Microscopy). dSTORM imaging is based on the stochastic activation and precise localization of spatially separated individual photo-switchable fluorophores and in our experimental setup, it enables a spatial resolution in cells of approximately 20 nm (Figure 4C).

For the investigation of BAK foci architecture by dSTORM, we transfected cells with GFP-BAK, induced apoptosis with staurosporine (STS) and labelled GFP-BAK with an anti-GFP

Alexa Fluor 647 nanobody. The use of a nanobody assured high labelling efficiency with minimal displacement between target and a dye with better photophysical properties for dSTORM than GFP. Cell lines with double knockout (DKO) of the two executors BAK and BAX were used to ensured that no endogenous BAK and BAX was present and involved in the formed foci. HCT116 DKO Bax$^{-/-}$/Bak$^{-/-}$ (human colon carcinoma) and U2OS DKO Bax$^{-/-}$/Bak$^{-/-}$ (human osteosarcoma) were used in this study.

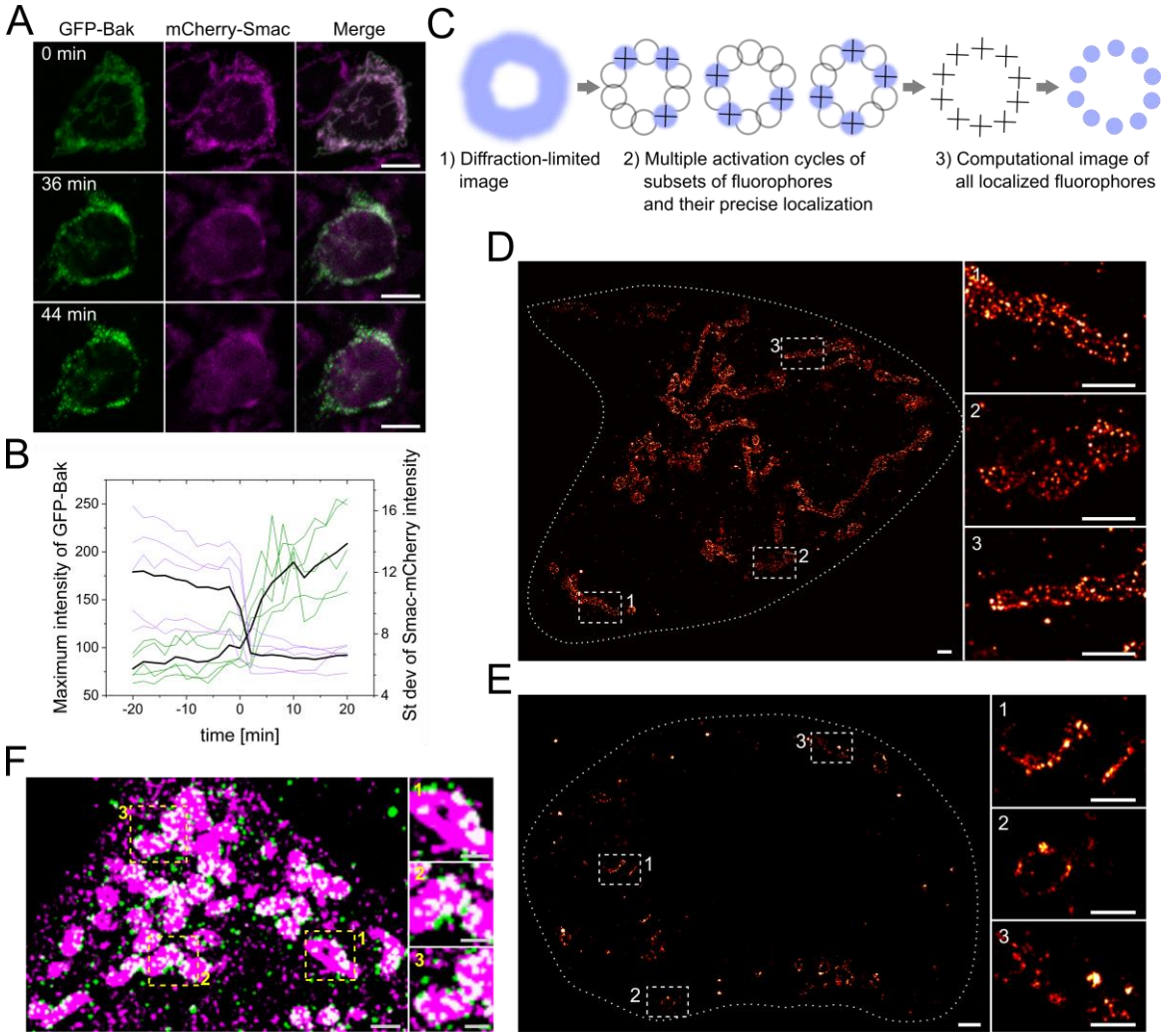

Figure 4: BAK assembly into distinct structures correlates with mitochondrial outer membrane permeabilization. *A) Exemplary images of a HCT116 DKO BAK$^{-/-}$/BAX$^{-/-}$ cell transfected with GFP-BAK (green) and Smac-mCherry (magenta) 0, 36 and 48 min after apoptosis induction with 1 µM STS. Scale bar 10 µM. B) Maximum fluorescent intensity of GFP-BAK and standard deviation of Smac-mCherry for individual cells (n=5). Time point 0 min corresponds to the normalized time point of Smac release. C) Scheme explaining the functional principles of dSTORM. D+E) Representative dSTORM images of GFP-BAK labelled with nanobody anti-GFP Alexa-647 in a HCT116 DKO BAK$^{-/-}$/BAX$^{-/-}$ cell under healthy (D) and apoptotic conditions (E). Panels on the right are zoomed images corresponding to the white boxes. Scale bar 1 µM for the main images and 500 nm for the zoomed images. F) Dual-color dSTORM image of GFP-BAK labelled with anti-GFP Alexa-647 (green) and mito-mMaple (magenta). Panels on the right are zoomed images corresponding to the yellow boxes. Scale bar 1 µM for the main images and 500 nm for the zoomed images.*

To determine the optimal time point for cell fixation after apoptosis induction, we measured the kinetics of TMRE loss as a proxy for apoptosis induction and identified the time point at which 50% of the GFP-BAK transfected cells had lost TMRE fluorescence. The loss of TMRE staining was analyzed by FACS measurement and showed that after 3 h 50% of the GFP-BAK positive cells lost their membrane potential, corresponding to the MOMP executed by BAK.

As a control, super resolution of BAK in healthy cells confirmed homogenous distribution of BAK on the mitochondrial network. Individual BAK fluorophores and very small BAK structures were found under this condition (Figure 4D). The small structures might also be individual fluorophores that are located at a closer proximity than the resolution limit of 20 nm. In apoptotic condition, however, BAK undergoes a dramatic reorganization into foci structures (Figure 4E). Dual colour dSTORM imaging of BAK and mitochondria verified the mitochondrial localization of the BAK structures (Figure 4F). Interestingly, BAK seems to be regularly located at the rim of the mitochondria forming a ring of small structures around a mitochondrion and often more intense and bigger BAK structures were found at the border between two mitochondria. It is tempting to speculate that these structures are located at the mitochondrial division sites because BAK co-localizes with Drp1 in confocal imaging of apoptotic cells and it has been previously proposed that BAK and BAX oligomerize preferentially at positions with high membrane curvature like Drp1-induced membrane hemifusion intermediates (Montessuit et al., 2010).

BAK organizes into rings, arcs and lines

dSTORM imaging demonstrated that in apoptotic cells BAK organized into foci with distinct architecture. BAK assembled into linear, arc-shaped and ring structures, as well as dots and aggregates (Figure 5A). The biggest fraction of structures consists of dots (37%) and aggregates (25%). Arcs (18%), lines (15%) and rings (6%) represented smaller, but significant fractions (Figure 5B).

It is important to note that 2-dimensional dSTROM imaging was performed to visualize the 3-dimensionally organized cells and their mitochondrial network. Mitochondria and associated BAK structures can adopt different orientations in the cell but only structures imaged perpendicular to the observation plane and within the focus can be detected correctly. Localizations that are out of focus would appear blurred and are eliminated partially during the reconstruction process. Structures that are orientated in a different angle to the observation plane would appear tilted. Due to this reason, it cannot be excluded that some of the observed BAK structures correspond to defined supramolecular assemblies that cannot be correctly annotated.

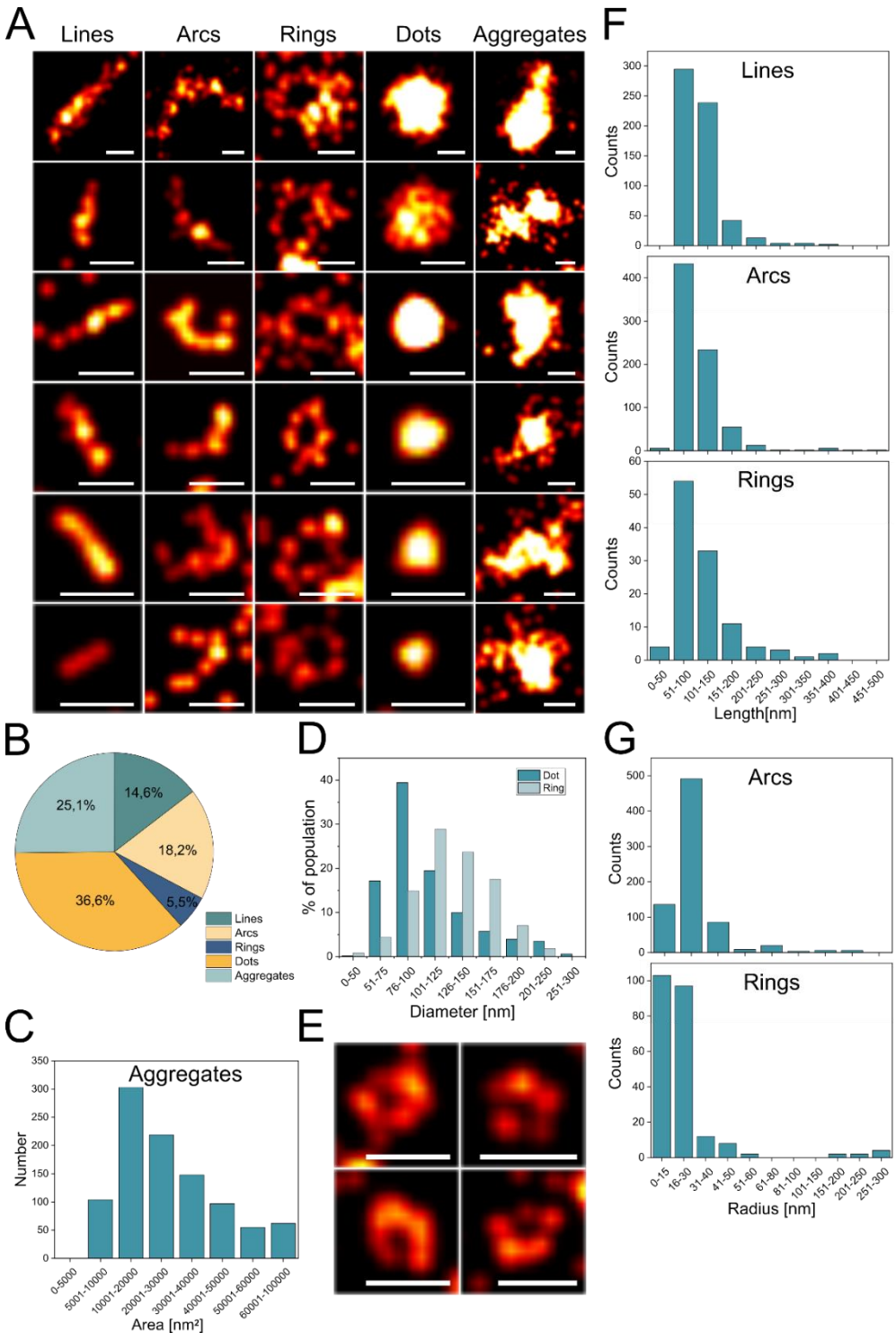

Figure 5: Structural analysis of BAK apoptotic assemblies. *A) Gallery of BAK structures in apoptotic HCT116 DKO BAK$^{-/-}$/BAX$^{-/-}$ cells. Scale 100 nm. B) Percentage distribution of the BAK structure types detected corresponding to the total number of the different structures found in all measured cells (n=12, total numbers: lines: 604; arcs: 753; rings: 230; dots: 1518; aggregates: 1044). C) Quantification of the area of aggregates of the total number of aggregates found in all measured cells (n=12, no. of aggregates: 1044). D) Quantification of the diameter of dots (blue) and outer diameter of rings (light blue) in percentage. (n=12, total numbers: dots: 1518; rings: 230). E) Exemplary images representing the fraction of dots with less intensity in the center. Scale bar 100 nm. F) Quantification of the line length, arc length and the ring perimeter. Graphs represent the total number of the different structure types found in individual cells (n=12, total numbers: lines: 604; arcs: 753; rings: 230). G) Quantification of the arc and ring radius. Graphs represent the total number of the different structure types found in individual cells (n=12, total numbers: arcs: 753; rings: 230).*

Characterizing the structural parameters, we found that the aggregates had no particular form and represent a wide distribution of sizes with areas of 5,000-100,000 nm^2 (Figure 5C). We cannot exclude the possibility that the observed aggregates are fixation or labelling artifacts, or fusions of multiple structures that cannot be resolved. The diameter of the dots varied between 50-200 nm. Interestingly, the outer diameter of the rings had a comparable size (Figure 5D). The observation of dots with lower intensity in the center and elliptic rings allows the speculation that some of the dots could be rings. It is possible that the hole in the center of the dot couldn't be visualized because of a lack of sufficient resolution or a non-perpendicular orientation to the observation plane (Figure 5E). The lines had a length between 50-150 nm, with an average length of 109 nm ± 32 nm. Interestingly, also arcs and rings had a similar arc length and perimeter between 50-150 nm and the average arc length of 103 nm ± 36 nm and average perimeter of 106 nm ± 40 nm (Figure 5F). For the arc and ring radius and their average, the same similarity was obtained. An arc and ring radius between 10-40 nm was measured with an average arc radius of 24 nm ± 8 nm and an average ring radius of 18 nm ± 9 nm (Figure 5G).

The presence of the different structures and the structural parameters could be confirmed in two different cell lines (Figure 6A-C) and in a minimal model membrane system using AFM of recombinant BAK on supported lipid bilayers. Activated recombinant BAK assembled into rings, arcs and lines of comparable size. Furthermore, AFM revealed that all of the rings and some arcs were able to perforate the lipid membrane (Figure 6D-F).

The average pore diameter of the rings was approximately 20 nm. To test whether the small size of the pores allows an efficient intake of differently sized proteins, we investigated the intake of fluorescently labelled cytochrome c and allophycocyanine (APC) in the model membrane system giant unilamellar vesicles (GUVs) after the incubation with different concentrations of activated recombinant BAK. Cytochrome c is a small intermembrane space protein with a molecular weight of 12.5 kDa and a hydrodynamic diameter of approximately 3 nm while APC is a large protein of 104 kDa and a hydrodynamic diameter of approximately 8 nm. The results showed that cytochrome c was efficiently internalized in a concentration dependent manner, while no efficient intake of APC was observed up to 1 µM of BAK (Figure 6G, H). The efficient intake of cytochrome *c* induced by BAK indicates that the individual pore size is bigger than 3 nm, the hydrodynamic diameter of cytochrome *c*, while under the used conditions of this experiment the pore size seems to be smaller than 8 nm, the hydrodynamic diameter of APC.

In summary, in apoptotic cells BAK assembles to linear, arc-shaped and ring structures of similar size and all rings and some of the arcs seem to be able to permeabilize the MOM.

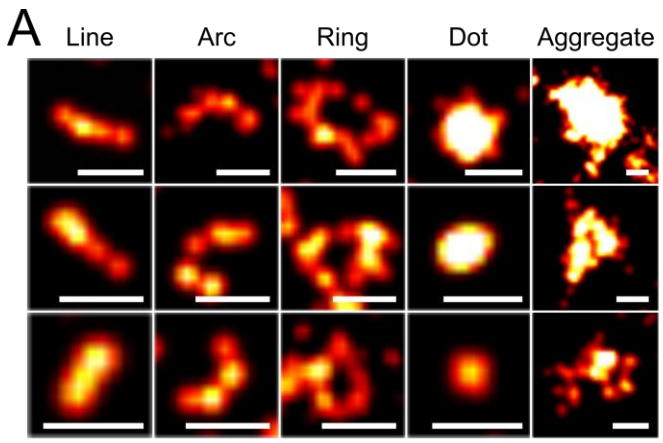

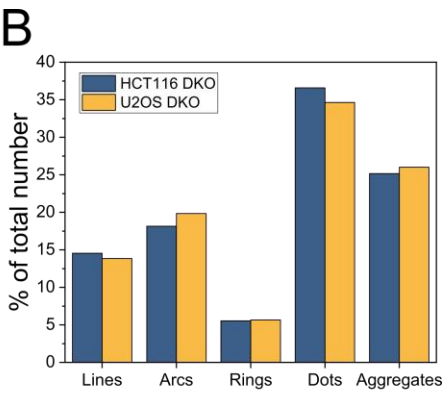

C

	HCT116 DKO	U2OS DKO
Line length	109 nm ± 32 nm	107 nm ± 37 nm
Arc length	103 nm ± 36 nm	101 nm ± 33 nm
Perimeter	106 nm ± 40 nm	104 nm ± 31 nm
Arc radius	24 nm ± 8 nm	25 nm ± 9 nm
Ring radius	18 nm ± 9 nm	17 nm ± 7 nm

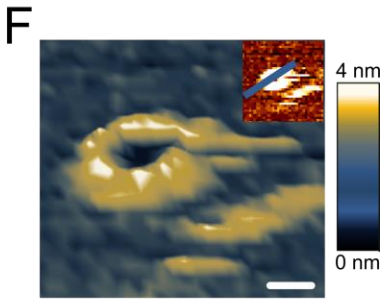

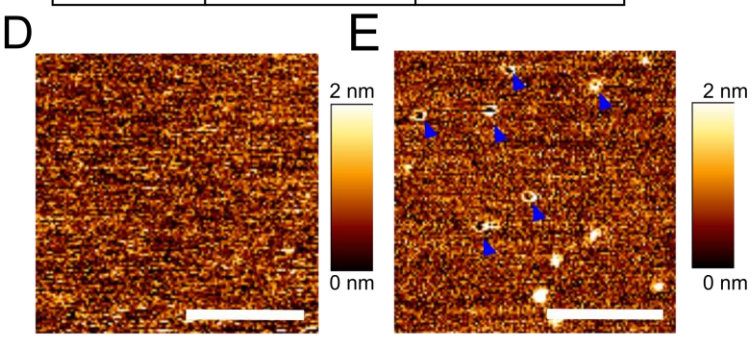

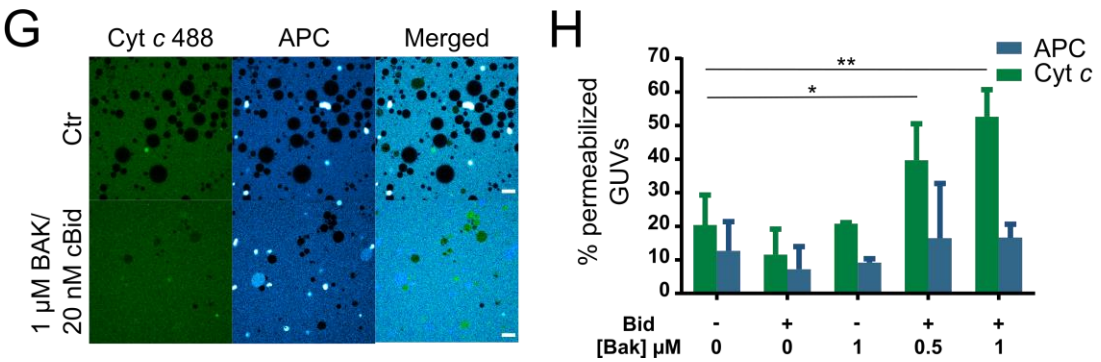

Figure 6: BAK pores perforate the membrane and allow the efficient release of small but not bigger proteins in artificial model membrane systems (previous page). *A) Gallery of BAK structures in apoptotic U2OS DKO BAK$^{-/-}$/BAX$^{-/-}$ cells. Scale 100 nm. B) Distribution of the different BAK structure types found in HCT116 DKO BAK$^{-/-}$/BAX$^{-/-}$ (n=12) and U2OS DKO BAK$^{-/-}$/BAX$^{-/-}$ (n=7) cells. C) Average size of the different parameters in HCT116 DKO BAK$^{-/-}$/BAX$^{-/-}$ and U2OS DKO BAK$^{-/-}$/BAX$^{-/-}$ cells. D,E) Representative atomic force microscopy images of EPC:CL (80:20) membranes without (D) and with BAK pores (E). Pores are indicated by the blue arrows. Scale bar 200 nm. F) Representative 3D image of a BAK pore and its height profile. The blue line corresponds to the line in the 2D image inset. Scale bar 20 nm. G) Representative images of EPC:CL (80:20) GUVs without and with addition of BAK and cBid. Scale bar 10 µm. Quantification of the percentage of permeabilized GUVs with APC (blue) and cytochrome c (green) for the different BAK concentrations. Experiments E-H performed by Katia Cosentino and Andreas Jenner.*

BAK structures evolve from lines to rings over time

Next, we tackled the question whether the linear and arc-shaped structures are intermediate assemblies evolving into final rings. The observation that lines, arcs and rings have a similar average size supported this assumption. Alternatively, these structures could be kinetically trapped states. We investigated whether we can detect a change in distribution of the different structure types or a growth in size of the structures using time-resolved dSTORM imaging. However, dSTORM imaging doesn't offer the possibility of live cell imaging because the cells need to be fixed and labelled for microscopy and the long imaging time is not feasible to image fast processes like apoptosis. To overcome these problems, we established correlative live-cell confocal and super-resolution microscopy. Here, we first imaged the apoptosis process at the single, living cell level using confocal microscopy, stopped the apoptosis progression after different time points of first BAK foci appearance in the monitored individual cells by fixation, performed immunostaining and imaged the same cell under the super-resolution microscope (Figure 7A, B). To do so, we took advantage of special gridded microscopy dishes containing a coordinate system to relocate the same cell in the different microscopy setups. Due to the coordinate system and the imaging of the apoptosis progression the position of the cell and their time since MOMP induction were known. This allowed us to image cells at different time points during apoptosis progression and investigate changes of BAK structures over time using super-resolution microscopy.

For correlative confocal and super-resolution microscopy HCT116 Bax$^{-/-}$/Bak$^{-/-}$ DKO cells were transfected with GFP-BAK and apoptosis was induced with the BH3-mimetic ABT-737 and the Mcl-1 inhibitor S63845. Cells 5 min, 10 min, 15 min and 30 min after first BAK foci appearance were imaged by dSTORM.

Comparing the percentage of the different structure types for the time points measured, we detected that 5 min after first BAK foci appearance more linear structures were present while at later time points more rings. We observed a 11% reduction of linear structures (5 min: 46% to 30 min: 35%) from 5 min to 30 min and an increase of 10% (5 min: 5% to 30

min: 15%) for the ring structures. The percentage of arcs was constant by approximately 50% over time (Figure 7C). This result suggests that BAK structures evolve over time and support a model in which they change from linear structures to rings over time. We cannot discard that the observed lines and arcs could be also kinetically trapped intermediates in the formation of full rings. However, the high percentage of arcs for all time points and their ability to perforate membranes might indicate that also the arc-shaped structures are important functional entities. In addition, as mentioned previously, it is also possible that some linear and arc structures are arc-shaped or ring structures that are wrongly oriented with respect to the observation plane.

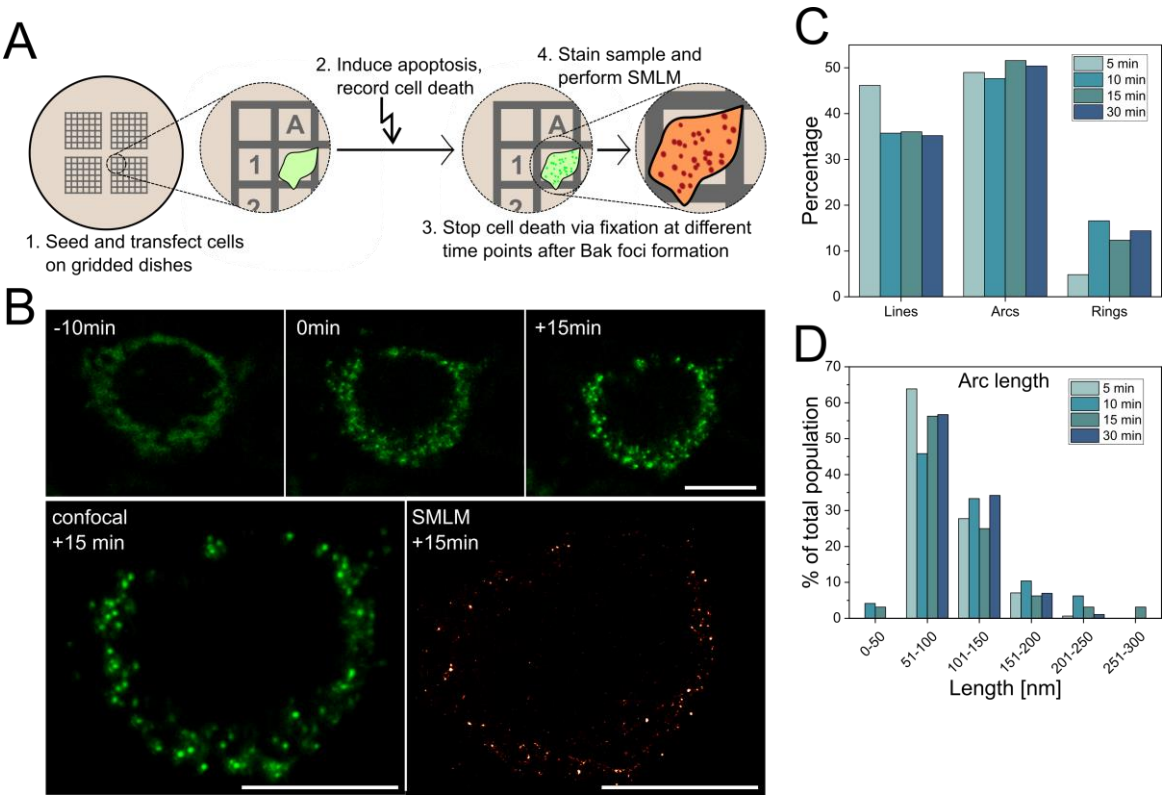

Figure 7: BAK structures evolve over time from linear to ring structures but do not increase more in size. *A) Scheme explaining the principles of correlative confocal and super-resolution microscopy. B) Upper panel: Images of a HCT116 DKO BAK$^{-/-}$/BAX$^{-/-}$ cell transfected with GFP-BAK 10 min before foci formation (-10 min), at the time point of first foci appearance (0 min) and 15 min after foci formation (+15 min). Lower panel: Comparison of the same cell in confocal microscopy (left) and dSTORM (right). Scale bar 10 µm. C) Percentage distribution of lines, arcs and rings at different times after first foci appearance (n=3 cells; no. of lines: 5 min: 229, 10 min: 84, 15 min: 108, 30 min: 132; no. of arcs: 5 min: 243, 10 min: 112, 15 min: 146, 30 min: 189; no. of rings: 5 min: 24, 10 min: 39, 15 min: 29, 30 min: 54). D) Distribution of the arc length at the different time points after first foci appearance (n=3 cells; no. of arcs: 5 min: 243, 10 min: 112, 15 min: 146, 30 min: 189).*

However, it seems that the temporal resolution of correlative confocal and super-resolution microscopy is not sufficient to measure the initial, more interesting steps of growth of the structures. We observed that for the earliest tested time point, 5 min after BAK foci appearance, the size of the structures and even the size distribution for the different

parameters measured were comparable with the later time points measured. For example, the linear and arc-shaped structures had a length of 50-150 nm for all measured time points and the average line and arc length showed no significant difference (line: 5min: 101 nm ± 24 nm, 30 min: 109 nm ± 31 nm; arc: 5min: 100 nm ± 28 nm, 30 min: 102 nm ± 31 nm). (Figure 7D) This result indicates that the assembly of the BAK foci is a fast process and the lines, arcs and rings are stable structures.

In summary, using correlative confocal and super-resolution microscopy we found that BAK assemblies seem to evolve from linear structures to ring structures over time. In addition, the growth of BAK foci appears to be a fast process occurring in the first few minutes after foci formation.

BAK assembles faster, but into foci with lower molecularity than BAX

The executor protein BAK presents a high sequence and structural homology with the second executor BAX, but differs in the main localization in the inactive form. BAX is predominantly cytoplasmic, translocating between the mitochondrial outer membrane (MOM) and the cytoplasm, while BAK is mainly localized at the MOM. Yet, they are believed to be redundant in executing the mitochondrial outer membrane permeabilization (MOMP). After activation, both form symmetric homodimers and oligomerize to higher species to permeabilize the MOM.

Comparing the obtained super-resolution microscopy results of BAK to the previously reported results of BAX demonstrated that BAK and BAX assemble to the same types of structures but the BAK structures are smaller and more uniform. The difference in the average size of the structural parameters for BAK and BAX are shown in Figure 8A.

The difference in the size of BAK and BAX structures raised the question whether the two executors also differ in the kinetics of foci assembly. To test whether BAK and BAX also differ in their kinetics of foci assembly and the molecularity of the formed foci, we examined their stoichiometry over time in living cells.

U2OS $Bax^{-/-}$/$Bak^{-/-}$ DKO cells were transfected with Smac-mCherry to define the time point of MOMP and GFP-BAX or GFP-BAK (Figure 8B). Cells transfected with GFP-BAX showed a higher fluorescence intensity than cells transfected with GFP-BAK (Figure 8C). This might result from the different localization of the constructs and is in line with the higher expression levels of endogenous BAX. Apoptosis was induced with a combination of ABT-737 and the Mcl-1 inhibitor S63845 and apoptosis progression in single cells was imaged every 5 min by confocal microscopy. The intensity of the BAK or BAX foci was

analyzed over time and the molecularity of the foci was calculated by normalizing to the intensity of Nup96 foci, which exhibit a known molecularity of a 32-mer.

The stoichiometry analysis showed that GFP-BAK foci assemble with faster kinetics than GFP-BAX (Figure 8G). This faster kinetics might be due to the MOM localization of BAK while BAX first requires recruitment to the MOM. To test this assumption, we used the BAX mutant BAX(S184V), which is constitutively located at the MOM (Figure 8B). Cells transfected with GFP-BAX(S184V) showed similar expression levels as GFP-BAK (Figure 8C) indicating that the difference in localization seems to be important for the expression levels. Moreover, in line with the assumption that the mitochondrial localization is important for the assembly kinetics, we observed that the MOM located BAX mutant GFP-BAX(S184V) possesses a faster kinetics of foci assembly than cytoplasmic BAX (Figure 8G). Interestingly, the assembly kinetics of BAX(S184V) is still slower than the kinetics of BAK suggesting that even mitochondrial localization is not sufficient for BAX to oligomerize as fast as BAK. This might result from a difference in the oligomerization process of BAK and BAX or an impaired oligomerization due to the mutation.

BAK and BAX differ not only in their kinetic of assembly but, also in the maximum molecularity of their foci. While BAK assembled quickly to a maximum average molecularity of the foci of approximately 200 molecules and reaching a plateau phase after approximately 10 min, BAX assembled slower but the foci grew larger over time in a linear fashion not saturating in the maximum average molecularity even after 60 min of measurement. The molecularity of BAX foci exceeded those of BAK after approximately 25 min (Figure 8D-G). The difference in kinetics is also detectable by the number of BAK or BAX foci with a molecularity of more than 200 or 400 molecules over time. While the number of foci with over 200 or 400 molecules for BAK is constant over time, the number of those foci is increasing for BAX (Figure 8I, J). Interestingly, the mitochondrial localization and the lower expression levels of BAK seem not to be the reason for the different growth behavior of the foci. Also, the mitochondria-located BAX(S184V), which is expressed at similar levels as GFP-BAK, showed a faster assembly kinetics due to its mitochondrial localization, and yet slower than BAK but exhibited the same growth behavior as BAX (Figure 8G). BAX(S184V) assembled fast but in a linear fashion indicating that the mitochondrial localization is partially responsible for a faster kinetics, but BAK and BAX differ in their mechanism of assembly.

A

	GFP-BAK	GFP-BAX
Line length	109 nm ± 32 nm	214 nm ± 80 nm
Arc radius	24 nm ± 8 nm	73 nm ± 30 nm
Ring radius	18 nm ± 9 nm	34 nm ± 7 nm

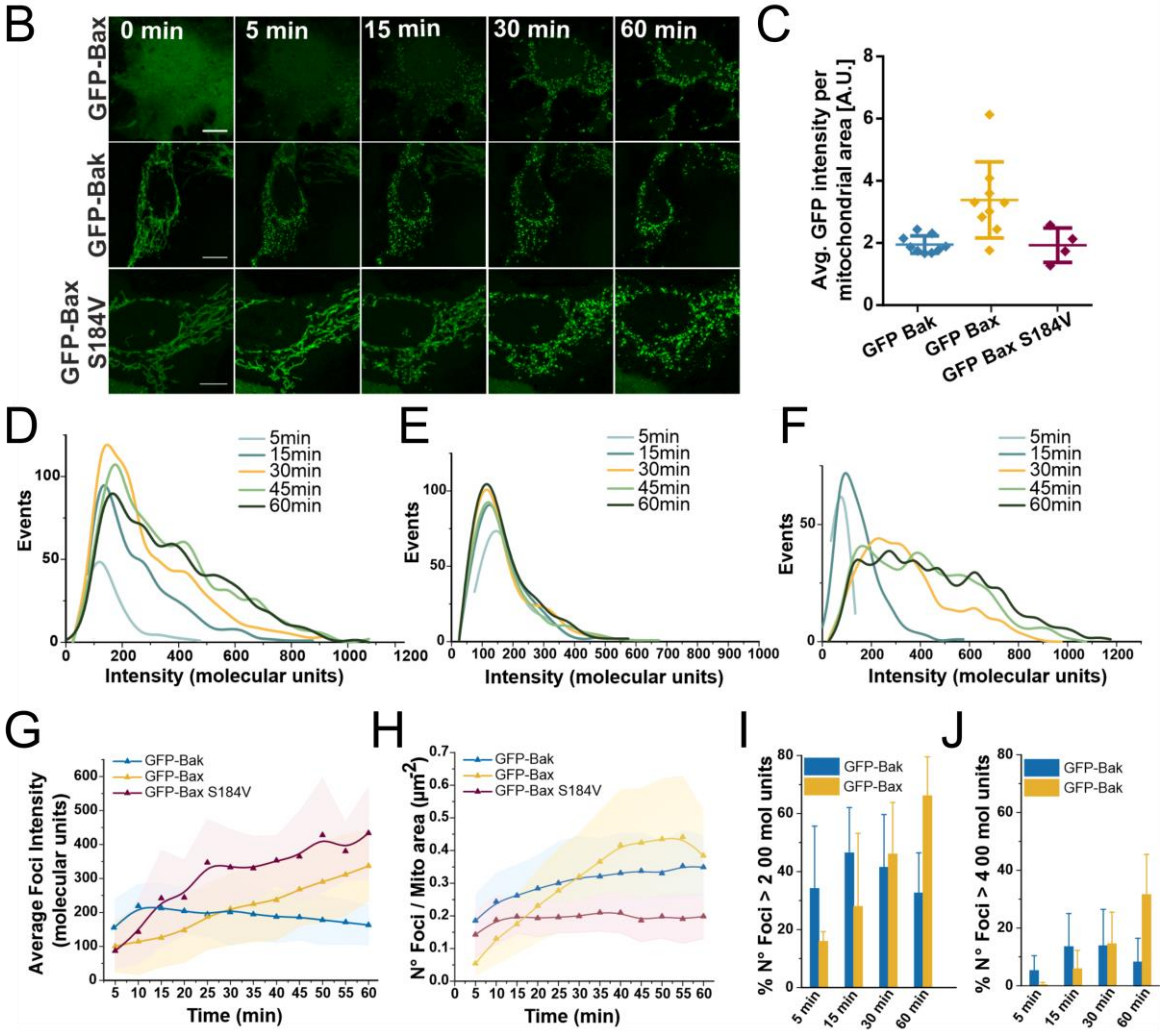

Figure 8: BAK and BAX foci differ in their assembly kinetics and maximal average molecularity. *A) Average size of the different parameters for GFP-BAK and GFP-BAX structures. B) Representative photon-counting confocal images of U2OS DKO BAX$^{-/-}$/BAK$^{-/-}$ cells transfected with GFP-BAK, GFP-BAX or GFP-BAXS184V and treated with 1 µM ABT-737, 1 µM S63845 and 10 µM qVD-Oph for apoptosis induction. Time points are the time after Smac-mCherry release. Scale bar 10 µm. C) Average GFP expression level per mitochondrial area in individual U2OS DKO BAX$^{-/-}$/BAK$^{-/-}$ cells (represented by individual dots in the plot) transfected with GFP-BAK, GFP-BAX or GFP-BAXS184V detected by single-cell fluorescent intensity analysis of GFP signal. D-F) Representative distribution of foci intensity, in stoichiometric units, at different time points in individual apoptotic U2OS DKO BAX$^{-/-}$/BAK$^{-/-}$ cells overexpressing GFP-BAX (D), GFP-BAK (E) or GFP-BAXS184V (F). G) Average foci intensity obtained from the fitting of foci distributions as in D-F at each time point for individual apoptotic cells expressing GFP-BAX (yellow, n= 9), GFP-BAK (blue, n=9) or GFP-BAXS184V (purple, n=4). Lines in the graph correspond to the average values from all measured cells and colored areas correspond to data variability from single cells (mean ± S.D.). H) Number of foci per mitochondrial area for GFP-BAX (yellow, n=9), GFP-BAK (blue, n=9) and GFP-BAX (S184V, n=4) (purple) over time. I+J) Number of foci with higher molecularity than 200 (I) or 400 (J) molecular units for GFP-BAX (yellow) and GFP-BAK (blue) over time. Experiments in B-J performed by Katia Cosentino and Andreas Jenner.*

Furthermore, for BAK and BAX(S184V) a constant number of foci was measured over time while the number of BAX foci increased (Figure 8H). This could be related with the higher expression levels of BAX and the possibility to recruit BAX molecules from the cytoplasm or that the faster assembly kinetics of mitochondrial effectors favors the recruitment of molecules to existing foci over the generation of new foci.

In summary, BAK and BAX differ in their kinetics of assembly, which might be related to their different localizations and also in their behavior of assembly. BAK assembles into foci with lower molecularity than BAX reaching a maximum average molecularity while BAX assemblies grow in a linear fashion. These results indicate a difference in the oligomerization mechanism of BAK and BAX.

Endogenous BAK accelerates the growth of BAX foci while endogenous BAX increases the BAK foci size

Previous studies showed that BAK and BAX are able to form hetero-oligomers (Dewson et al., 2012) and that they co-localize in foci in confocal microscopy. We investigated whether BAK and BAX influence each other's foci molecularity and assembly kinetics. To test this, we performed stoichiometry analysis in U2OS single knockout cells for either BAK or BAX, containing endogenous BAX and BAK, respectively, and compared these results to the ones obtained in U2OS $Bax^{-/-}/Bak^{-/-}$ DKO cells. GFP-BAX and GFP-BAK showed identical protein expression levels and fluorescent intensity in single and double KO cells and the GFP-BAX expression was higher than the one of GFP-BAK (Figure 9B).

In single KO cells a similar assembly behavior for BAK and BAX foci as in the DKO cells was observed. BAK showed a fast growth ending in a plateau phase with foci of a maximal molecularity. For BAX, a slower kinetics than BAK was detected with a linear growth not reaching a maximal molecularity of the foci over the time we measured. BAX exceeded the average molecularity of BAK after approximately 15 min after foci appearance (Figure 9C-E).

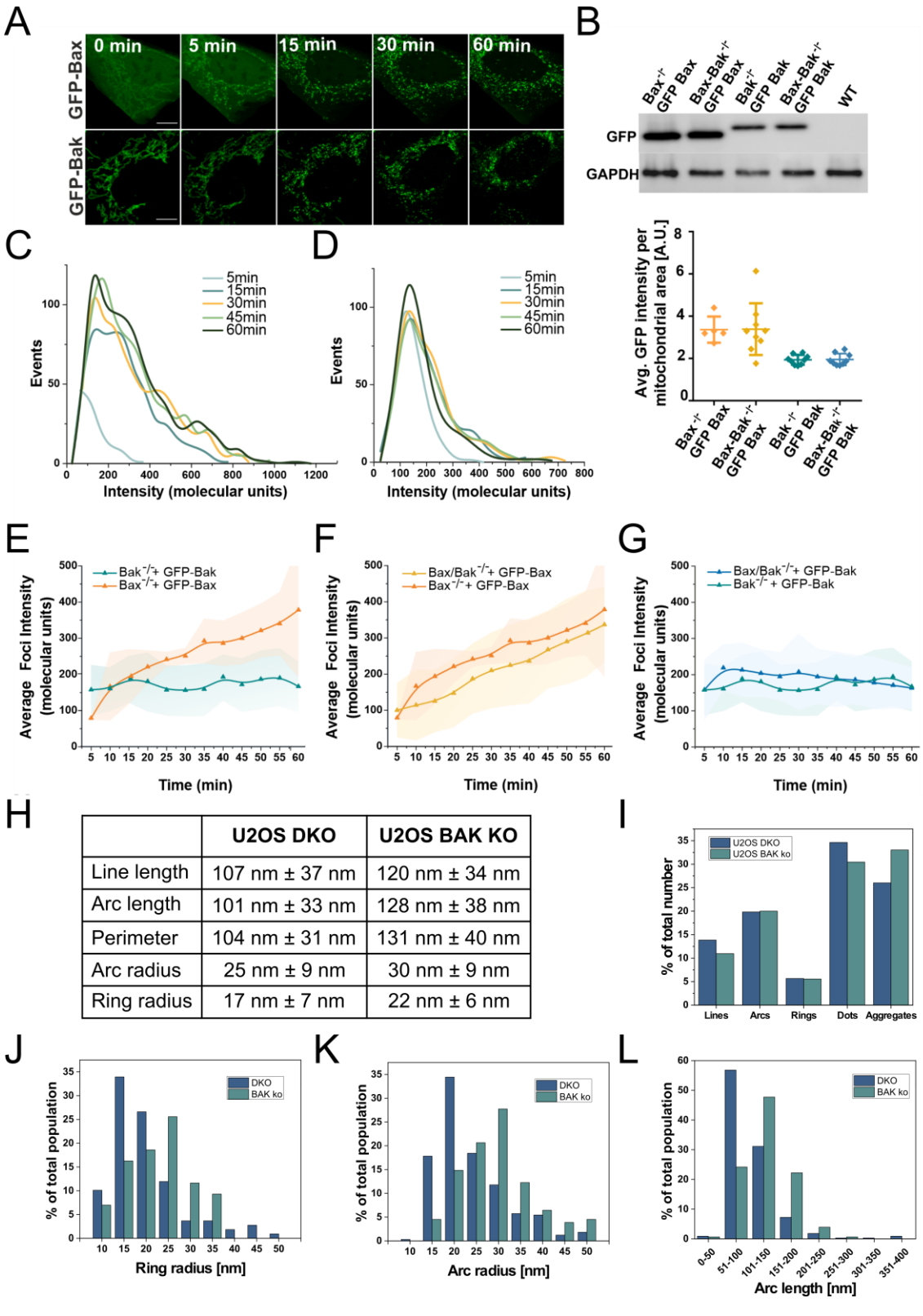

	U2OS DKO	U2OS BAK KO
Line length	107 nm ± 37 nm	120 nm ± 34 nm
Arc length	101 nm ± 33 nm	128 nm ± 38 nm
Perimeter	104 nm ± 31 nm	131 nm ± 40 nm
Arc radius	25 nm ± 9 nm	30 nm ± 9 nm
Ring radius	17 nm ± 7 nm	22 nm ± 6 nm

Figure 9: Reciprocal contribution of BAK and BAX to their assembly kinetics and molecularity (previous page). A) Representative photon counting confocal images of U2OS DKO BAX$^{-/-}$/BAK$^{-/-}$ cells transfected with GFP-BAX and GFP-BAK, respectively, after apoptosis induction by 1 µM ABT-737, 1 µM S63845 and 10 µM qVD-OPh. Time points are after Smac-mCherry release. Scale bar 10 µm. B) Comparison of the expression levels of GFP-BAK and GFP-BAX in single or double BAX$^{-/-}$ and/or BAK$^{-/-}$ U2OS cells detected by western blot (upper) or by single-cell (individual dots in the plot) fluorescent intensity analysis of GFP signal (bottom). WT=wild type. C-D) Representative foci intensity distribution, in stoichiometric units, at different time points in an apoptotic BAX$^{-/-}$ (C) and BAK$^{-/-}$ U2OS (D) cell expressing GFP-BAX and GFP-BAK, respectively. E) Average foci intensity obtained from the fitting of foci distributions as in C-D at each time point for individual apoptotic BAK$^{-/-}$ or BAX$^{-/-}$ U2OS cells expressing GFP-BAX (orange, n= 5) or GFP-BAK (green, n=9). F) Comparison between the average foci intensity of GFP-BAK in U2OS DKO BAX$^{-/-}$/BAK$^{-/-}$ (blue, n=9) and U2OS BAK$^{-/-}$ (green, n=9) cells over time. G) Comparison between the average foci intensity of GFP-BAX in U2OS DKO BAX$^{-/-}$/BAK$^{-/-}$ (yellow, n=9) and BAX$^{-/-}$ U2OS (orange, n=5) cells over time. In F and G *P < 0.1 (unpaired t-test with Welch´s correction). H) Number of GFP-BAX (orange, n=5) and GFP-BAK (green, n=9) foci per mitochondrial area in single KO U2OS cells over time (total number of events as in D-F). For E-H, lines in the graph correspond to the average values from all measured cells and colored areas correspond to data variability from single cells (mean ± SD). I) Average size of the different structural parameters for GFP-BAK assemblies in U2OS DKO BAX$^{-/-}$/BAK$^{-/-}$ (n=7) and U2OS BAK$^{-/-}$ (n=6) cells measured by SMLM. J) Distribution of the different BAK structure types found in U2OS DKO BAX$^{-/-}$/BAK$^{-/-}$ (n=7) and U2OS BAK$^{-/-}$ (n=6) cells (minimum number of analyzed structures = 86). K-M) Comparison of the quantifications of the ring radius (K), arc radius (L) and arc length (M) in U2OS DKO BAX$^{-/-}$/BAK$^{-/-}$ (blue) and U2OS BAK$^{-/-}$ (green) cells. Number of analyzed structures in single and double KO cells, respectively: 86 and 109 (K), 310 and 363 (L), 310 and 363 (M). Experiments in A-G performed by Katia Cosentino and Andreas Jenner.

The comparison of the kinetics of BAX foci assembly between the DKO and KO cell line showed that endogenous BAK accelerates the initial assembly of BAX foci, while the rate of growth at later stages is comparable in both cell lines (Figure 9F). In contrast, we detected a decrease in the assembly speed and the molecularity of BAK foci in the presence of endogenous BAX. BAK showed a lower maximum molecularity in KO cells than in DKO cells, which might be due to the participation of unlabeled BAX molecules into the BAK foci (Figure 9G). It is tempting to speculate that BAK and BAX molecules form part of the same foci. In that scenario, small BAK oligomers, due to their faster assembly kinetics, could act as seeding points and recruit BAX from the cytoplasm, thereby accelerating its assembly. In support of this idea, we detected BAK foci before the BAX foci in some of the cells we imaged with dual-color live confocal microscopy during apoptosis progression, but never the opposite. Furthermore, the fluorescent intensity of GFP-BAX foci increased over time while the intensity of mCherry-BAK foci was constant during the measurement which is in agreement with the assembly behavior and the slower kinetics of BAX. (Figure 10)

dSTORM imaging of BAK in U2OS Bak$^{-/-}$ KO cells containing endogenous BAX showed an identical distribution of BAK structure types, that were however bigger compared to those in DKO cells (Figure 9H-L). For example, the average radius of rings increased from 17 nm ± 7 nm in DKO to 22 nm ± 6 nm in Bak$^{-/-}$ KO cells and the average arc length from 101 nm ± 33 nm in DKO to 128 nm ± 38 nm in Bak$^{-/-}$ KO cells. Altogether, our results indicate that the presence of endogenous BAX increases the size of BAK structures.

In summary, our results indicate that there is a reciprocal contribution between the two executor proteins BAK and BAX. BAK accelerates the kinetics of BAX foci assembly maybe by providing seeding points for BAX recruitment from the cytoplasm, while BAX increases the size of the BAK apoptotic structures.

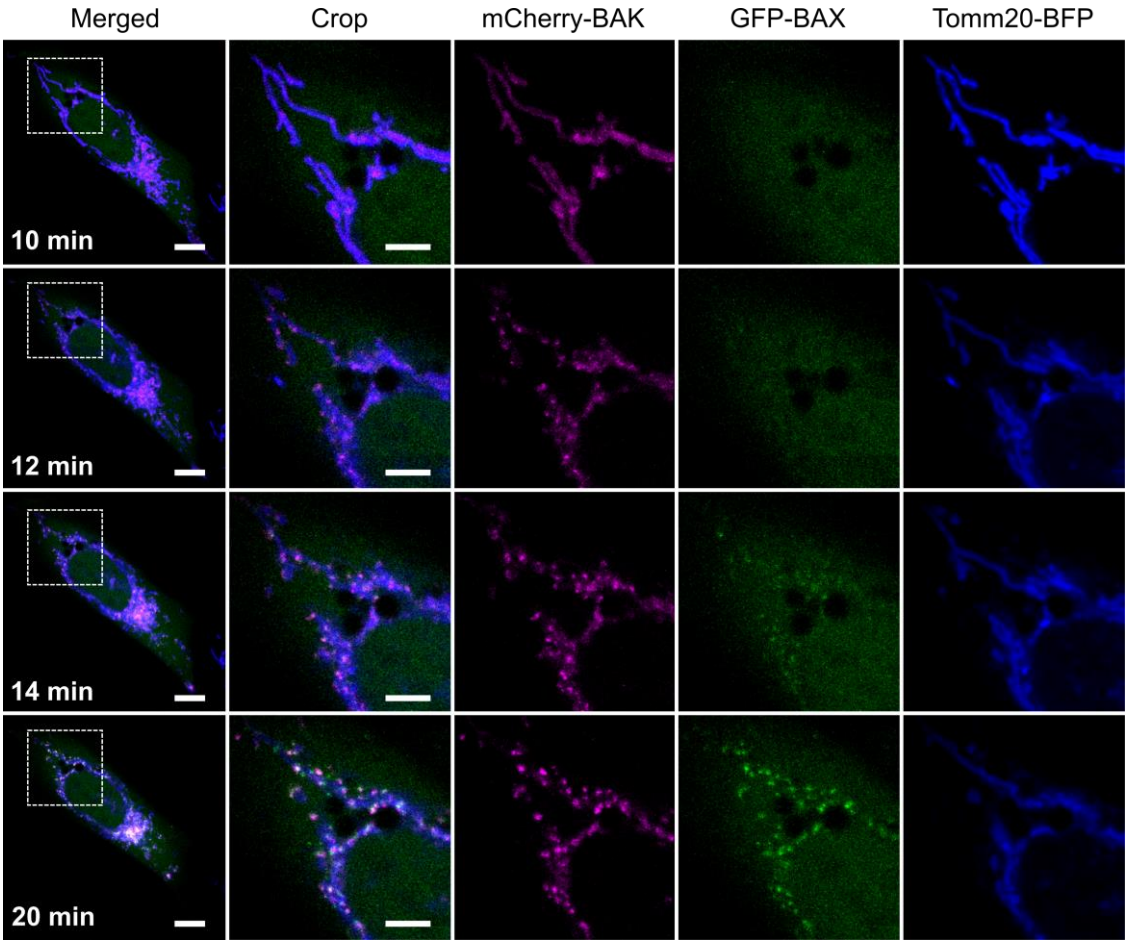

Figure 10: BAK accumulates prior to BAX in apoptotic foci. *Representative images of U2OS DKO BAK$^{-/-}$/BAX$^{-/-}$ cells transfected with mCherry-BAK (magenta), GFP-BAX (green) and Tomm20-BFP (blue) after the induction of apoptosis with ABT-737 and the Mcl-1 inhibitor S63845. The white box in the first column represents the zoomed area (crop) in the second column. Scale bar 10 µm for the left column and 5 µm for the other columns.*

BAK pores release mtDNA faster than BAX pores

In 2018, it was reported that BAK and BAX pores not only permeabilize the mitochondrial outer membrane (MOM) but also the mitochondrial inner membrane (MIM). The permeabilization of the MIM allows the release of the mitochondrial DNA (mtDNA) from the matrix. The presence of the mtDNA in the cytoplasm activates the STING-cGAS pathway and leads to inflammatory signaling under caspase deficient conditions. (McArthur et al., 2018; Riley et al., 2018; Rongvaux et al., 2014; White et al., 2014)

We studied whether BAK and BAX pores differ in their efficiency or kinetics to release mtDNA. We assumed that the smaller size of the BAK pores or the faster kinetics of the BAK pore assembly could influence the release of the huge mtDNA molecules.

For the investigation of the mtDNA release we used a similar experimental approach as for the correlative live-cell fluorescence confocal and super-resolution microscopy (Figure 11A). U2OS BAX$^{-/-}$ ko or U2OS BAK$^{-/-}$ ko cells, containing only endogenous BAK or endogenous BAX, respectively, or wild type (WT) U2OS cells containing both were seeded on the special cell culture dishes with the coordinate system. The cells were transfected with Smac-mCherry for the detection of the MOMP and TFAM-GFP for the labelling of the mtDNA. Apoptosis was induced with the BH3-mimetic ABT-737 and the Mcl-1 inhibitor S63845 and apoptosis progression was stopped by fixation after different time points of Smac release, which correlates with the formation of BAK or BAX pores. For AiryScan detection the mitochondria were immunostained with an α-Tomm20 antibody and Tomm20 and TFAM were imaged.

Control cells without induction of apoptosis and cells fixed 5 min, 10 min, 15 min, 30 min and 60 min after MOMP were analyzed for the release of mtDNA from mitochondria. The control cells confirmed the complete matrix localization of the mtDNA in all three cell lines. We observed that both BAK- and BAX- induced MOMP enables efficient mtDNA release. For both cell lines containing either BAX or BAK, a mtDNA release of up to 100% was detected. However, the cell lines showed differences in the kinetics of mtDNA release. For the cell line containing only endogenous BAK, a complete mtDNA release (90-100%) was found after 10 min, while for the cell line containing endogenous BAX a complete mtDNA release was observed after 30 min (Figure 11B, C). These results suggest that the smaller BAK pore is sufficient to efficiently release mtDNA and that the faster kinetics of assembly of BAK high-molecular oligomers enables an earlier release of mtDNA. Interestingly, and in line with the previous results, U2OS WT cells containing both endogenous BAK and BAX showed an intermediate kinetics, indicating a reciprocal modulation of the two executor proteins. The presence of BAX seems to slow down the kinetics of BAK.

In summary, both executors BAK and BAX enable an efficient mtDNA release, however with a faster kinetics for BAK, which is in line with the faster assembly kinetics of the BAK foci. This difference might lead to differences in inflammatory output for BAK- or BAX-dependent apoptosis pathways.

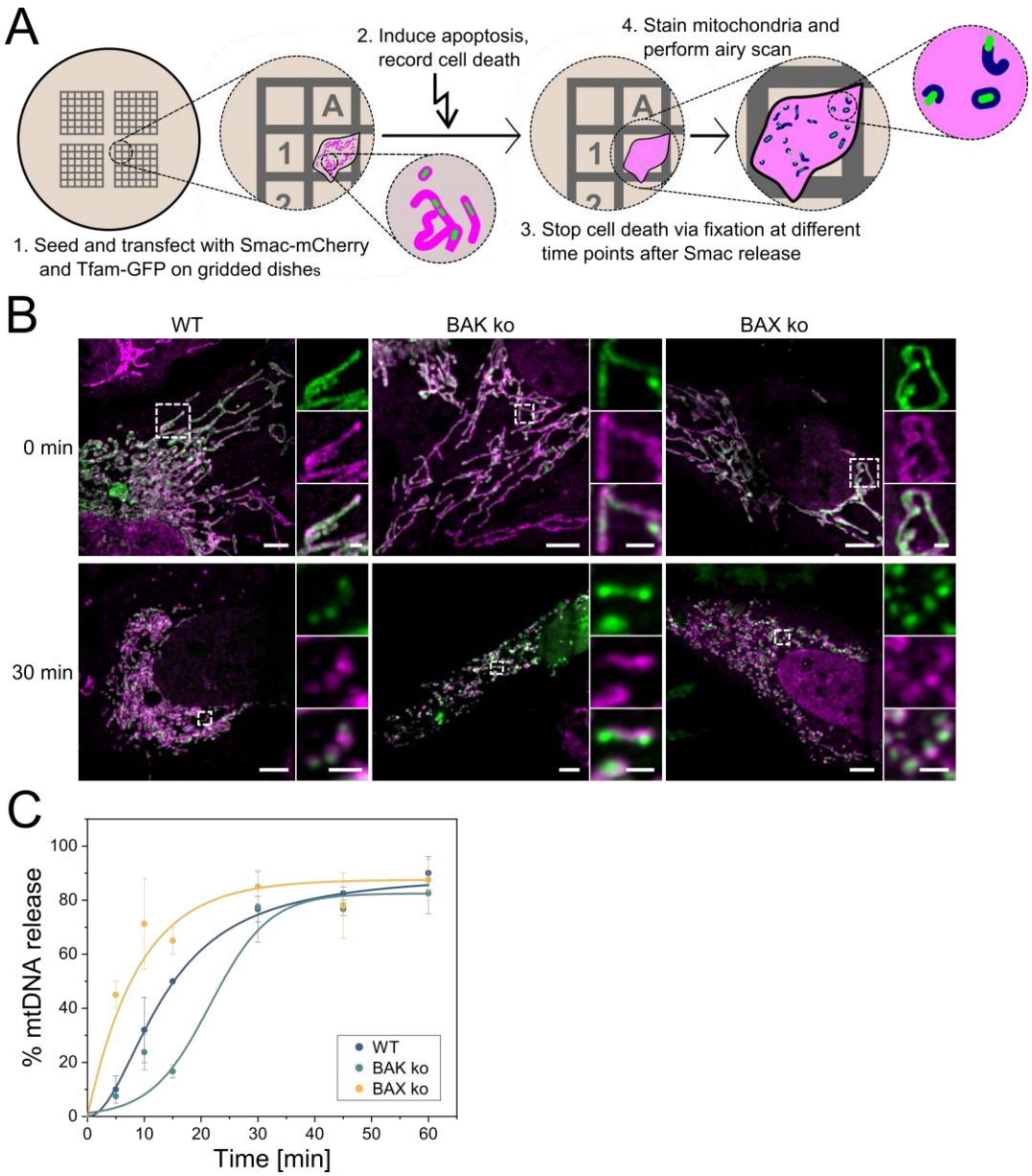

Figure 11: Both BAK and BAX pores enable an efficient mtDNA release with a faster kinetics for the BAK pores. *A) Scheme explaining the experimental setup to investigate the mtDNA release. B) Representative images of U2OS WT, BAK$^{-/-}$ KO, and BAX$^{-/-}$ KO cells transfected with TFAM-GFP (green) and immunostained with α-Tomm20 antibody (magenta) without induction of apoptosis (upper panel; 0 min) and 30 min after pore formation (lower panel; 30 min). Smaller panels on the right represent zoomed region of the white box in the main image. Scale bar 5 µm for the main image and 1 µm for the zoomed region. C) Percentage of mtDNA release in U2OS WT (blue), BAK$^{-/-}$ KO (turquoise), and BAX$^{-/-}$ KO (yellow) cells over time. Graph shows the mean ±SD of individual cells (n=3-5 per time point). Experiments performed in collaboration with Katia Cosentino.*

DISCUSSION

The permeabilization of the mitochondrial outer membrane by BAK and BAX is the crucial step of intrinsic apoptosis and is considered the point-of-no-return. The two homologs BAK and BAX are believed to play redundant roles in mediating this process. To date, the mechanism underlying the assembly and the pore formation is still elusive. In this thesis, we showed that BAK and BAX differ in the assembly kinetics of their apoptotic pores, the pore size and that they regulate each other via co-assembly. Furthermore, we demonstrated that the faster assembly kinetics of BAK causes an earlier release of mtDNA.

We visualized the supramolecular organization of BAK apoptotic foci using super-resolution microscopy and showed that BAK assembled into distinct apoptotic structures on mitochondria. These structures included dots and aggregates and a smaller yet significant portion of rings, arcs and lines. The 2-dimensional dSTORM imaging method used, does not consider the 3-dimensional nature of the cell, their mitochondria and the associated BAK structures. Only structures that are oriented perpendicular to the observation plane were detected correctly. Structures oriented in other angles might not be visualized accurately. For example, a ring that was not oriented perpendicular to the observation plane might appear tilted as an arc or even line. Furthermore, the resolution limit of dSTORM imaging in cells is about 20 nm. Since the size of some structures was close to this limit, it might be possible that they were not resolved properly. We detected a portion of dots, possessing a similar diameter than rings, that showed lower intensity in the center. It might be possible that due to the resolution limit some rings were wrongly identified as dots.

All super-resolution results were verified in a second cell line showing same structures, size and distribution of the structures. Moreover, atomic force microscopy of BAK structures in supported lipid bilayers also identified ring, arc-shaped and linear structures reassuring that those are the functional entities of BAK assemblies. In addition, all rings and some arcs were able to perforate the membrane. This supports the idea of BAK and BAX forming toroidal pores in which not only the proteins line the pore rim but also the lipids participate in the pore formation. The opening of a pore requires the reduction of the line tension, which in the case of BAK can also be achieved by partial coverage of the pore rim as the arc-shaped pores demonstrate. This is in agreement with previous reports for BAX in lipid nanodiscs where an individual BAX molecule was sufficient to open a small

pore and atomic force microscopy results showing that arc-shaped BAX structures are able to stabilize a pore opening (Salvador-Gallego et al., 2016; Xu et al., 2013).

The detected rings, arcs and lines possessed a length mainly between 50-100 nm and the rings and arcs had similar radii of approximately 15-30 nm. Due to the similar size of BAK rings, arcs and lines, we speculated that lines and arcs might be intermediates that evolve into full rings. To test this hypothesis, we used correlative live-cell confocal and super-resolution microscopy. With this approach, we showed that the assembly of the BAK structures is a fast process. No differences in structure lengths or radii could be detected between 5 to 60 min after foci formation with 5 min being the shortest time point that could be measured with this method due to the fact that the cell death process is detected by the formed BAK foci and the time that is required to fix the cells. Nonetheless, a small difference in the percentage of lines and rings was detected. The number of lines declined over time while the number of rings increased. The number of arcs was constant. This supports the idea that indeed BAK structures are able to evolve over time according to our hypothesis, but also arc-shaped structures seem to be functional entities.

Next, comparing the visualized BAK structures with those that have previously been reported for BAX we found that BAX structures are bigger and less uniform. This difference might be due to a difference in the assembly mechanism or concentration. In most of the cells, BAX is more abundant than BAK most likely due to its cytosolic localization. Furthermore, BAK and BAX assemblies form by the oligomerization of dimer units. It might be that BAK and BAX differ in their oligomerization mechanism with different oligomerization surfaces and different intra-dimer interaction strengths, which might allow BAX to oligomerize into bigger structures.

In addition to the size of their supramolecular structures, BAK and BAX also differ in their assembly kinetics and foci molecularity. BAK oligomers assembled faster than BAX which might be at least partially related to the difference in localization. While BAK is located directly at the mitochondrial outer membrane, BAX first needs to be recruited from the cytoplasm to mitochondria. BAK assembled fast into foci of an average maximum molecularity reaching a plateau phase after about 10 min. BAX, however, assembled slower but with a nearly linear increasing molecularity not reaching an average maximum molecularity during the time of measurement. Hence, the BAX molecularity exceeded the one of BAK after approximately 25 min. Possible explanations for the difference in foci growth could be, first, that BAK and BAX differ in their oligomerization domains. BAK might have more defined oligomerization surfaces, limiting the options of oligomerization and maybe forming stronger intra-dimer connections. BAX might have less defined, looser

interaction surfaces allowing freer oligomerization and more flexible pore size. Second, due to the difference in localization BAK might form initially a higher number of seeding points for foci which would keep the molecularity lower, while BAX that is recruited from the cytoplasm might prefer to assemble to preexisting foci than creating a new seeding point. Third, related with the previous point, the difference in localization of BAK and BAX results in different protein levels, with BAX having higher expression levels. The smaller number of BAK molecules might cause the lower molecularity.

Evidence against this last point is provided by the finding that the mitochondria-located BAX mutant BAX S184V was expressed at similar levels than BAK, but the molecularity still increased in a linear fashion similar to the wild type BAX. While there was no difference in the assembly mechanism between BAX and BAX S184V, BAX S184V showed a faster initial assembly kinetics than the cytosolic BAX, which confirms that the mitochondrial localization increases the initial assembly kinetics by bypassing the recruitment step. The assembly kinetics of BAX S184V was still slower than the one of BAK, which either might be a side effect of the mutation or because of a more efficient assembly of BAK molecules, suggesting a difference in the assembly mechanism. The number of BAX foci was growing over time. In contrast, the number of foci was constant for BAK and BAX S184V which suggests that the change in number might be due to the higher protein concentration of BAX and/or the recruitment from the cytoplasm.

Fluorescent microscopy of BAK and BAX in apoptotic cells by us and by others as well as the purification of mixed dimers revealed that BAK and BAX co-localize in foci and are able to interact with each other (Dewson et al., 2012). Hence, we examined the influence of the two proteins towards each other. The use of single knockout cell lines enabled us to investigate the assembly kinetics and foci molecularity of BAK or BAX with the other protein being present in the cell at endogenous protein levels.

In cells expressing BAK, the initial assembly kinetics of BAX was significantly increased compared to the BAK deficient cell line. It is tempting to speculate that BAK might form the initial seeding points for the shared foci due to its mitochondrial localization and its therefore faster kinetics. BAX subsequently gets recruited to those pre-formed foci which accelerates the initial recruitment. In agreement with this hypothesis, we detected using confocal microscopy that BAK foci preceded the formation of BAX foci in some cells.

Endogenous BAX, on the other hand, seemed to slow down the initial BAK foci formation and reduce the foci molecularity slightly. This might be explained by the recruitment of endogenous BAX molecules to the BAK seeding points which might cause a competition between BAK and BAX for oligomerization sites and might also cause that BAK is forming

more seeding points than it would in BAX deficient cells. The higher ability of BAK than BAX to activate other BAK or BAX molecules, as previously reported by Iyer et al., supports the idea that BAK might provide the initial seeding points for both BAK and BAX foci (Iyer et al., 2020). Super-resolution microscopy of BAK apoptotic structures in cells with endogenous BAX levels showed that the size of the supramolecular assemblies increased slightly which might be caused by the co-assembled BAX molecules.

These findings clearly demonstrate that BAK and BAX influence each other and that regulation of BAK and BAX protein levels or the preferential activation of one of them by the BH3-only proteins could be a way to control the progression of the pore formation and subsequent cell death.

Recently, it was reported that BAK and BAX not only perforate the mitochondrial outer membrane but also the inner membrane which subsequently leads to the release of the mtDNA from the matrix into the cytoplasm, activation of the STING-cGAS pathway and IFN production (McArthur et al., 2018; Riley et al., 2018; Rongvaux et al., 2014; White et al., 2014). We hypothesized that the difference in kinetics or pore size could give rise to a difference in kinetics or completeness of mtDNA release. We assumed that either the smaller pore size of BAK hinters the release of mtDNA and formation of bigger pores together with BAX are required or that the superior assembly kinetics of BAK might cause a faster release of the mtDNA which might be independent of the increase in pore size by BAX. We showed that pores created solely by BAK are sufficient for an efficient mtDNA release. The faster assembly kinetics enabled a nearly complete release in approximately 10 min after mitochondrial outer membrane permeabilization while BAX requires 30 min.

The efficient and fast release of huge macromolecules like the mtDNA by small BAK pores raises the question of the necessity and function of the continuous growth of the BAX foci. Ader et al. reported that in late apoptotic cells BAX molecules form big sponge-like meshwork close to the mitochondrial outer membrane which seems to contain molecules, structures and even lipids originating from all different mitochondrial comportments and from the cytoplasm. These structures might be related to the outer membrane rupture and inner membrane flattening. (Ader et al., 2019)

In summary, we discovered core differences in the oligomerization process and kinetics of BAK and BAX during apoptosis. We showed that apoptotic BAK assembled into distinct supramolecular structures, which are similar to those formed by BAX, however smaller and more uniform in size. Moreover, we demonstrated that the interplay between BAK and BAX regulates the growth rate of the apoptotic pores and thereby modulates the release of the mitochondrial content. The mitochondrial localization of BAK gives rise to the faster

assembly kinetic and supports a model in which BAK forms the initial seeding points of the apoptotic pores to which BAX molecules get recruited and facilitate a slow growth. Finally, the balance between BAK and BAX assembly tuned the relative kinetic of Smac and mtDNA release, which might affect the immunogenic impact of apoptosis.

MATERIALS AND METHODS

Reagents

Product	Concentration	Source	Catalog no.
ABT-737	1 µM	MedChemExpress	HY-50907
DMEM		Sigma	D6046
DMEM phenol red free		Sigma	D5921
ECL Developer		Perkin Elmer	NEL103001EA
FBS	10%	Thermofisher	10270106
Lipofectamine 2000		Invitrogen	11668019
McCoy		Sigma	M9309
McCoy phenol red free		Sigma	SH30270.01
MitoTracker™ Deep Red	100 nM	Thermofisher	M22426
OptiMEM		Thermofisher	31985070
Paraformaldehyde	4%	VWR	PIER28908
PBS		Sigma	D8537
Penicillin/Streptomycin	1%	Sigma	P4333
Ponceau S		Carl Roth	5938.2
Protease inhibitor cocktail	1x	Sigma	4693159001
PVDF membrane		Merck Millipore	IPVH00010
QVD-OPh	10 µM	ApexBio	A8165
S63845	1 µM	MedChemExpress	HY-100741
Staurosporine	1 µM	LC Laboratories	S3900
TMRE	200 nM	Thermofisher	T669
Trypsin (10x)	1x	Sigma	59418C

Table 1: Reagents used in the "BAK assembles into smaller yet functional pores than BAX" study

Antibodies

Product	Dilution	Source	Catalog no.
AF488-anti mouse	1:200 (IF)	Thermofisher	A-11008
AF633-anti mouse	1:200 (IF)	Thermofisher	A-21052
AF633-anti rabbit	1:200 (IF)	Thermofisher	A-21070
FluoTag-Q anti-GFP Alexa Fluor 647	1:2000 (IF)	NanoTag Biotchnologies	N0301
Anti-mouse HRP-conj	1:10000 (WB)	Jackson Immuno	115-035-003
Anti-rabbit HRP-conj	1:10000 (WB)	Jackson Immuno	111-035-003
BAK	1:1000 (WB)	Cell signalling	12105
BAX	1:1000 (WB)	Cell Signalling	5023
CoxIV	1:200 (IF)	Thermofisher	MA5-15078
GAPDH	1:1000 (WB)	Abcam	Ab9485
Tomm20	1:100 (IF)	Cell signalling	42406

Table 2: Antibodies used in the "BAK assembles into smaller yet functional pores than BAX" study

Buffers

Name	Composition
6x Loading Buffer	4% SDS, 10% ß-mercaptoethanol, 20% glycerol, 0.004% bromophenol blue, 0.125 M Tris HCl pH 6.8
Blinking Buffer	50 mM Tris/HCl pH 8, 10 mM NaCl, 10% (v/w) glucose, 35 mM cysteamine (MEA), 0.5 mg/mL glucose oxidase, 40 g/ml catalase
Blocking Buffer (IF)	1% BSA in PBS
Blocking Buffer (WB)	TBS buffer supplemented with 5% (w/v) non-fat dry milk (Roth)
Blotting Buffer	20 mM Tris, 150 mM glycine, 0.02 % (w/v) SDS, 20 % (v/v) methanol in purified water
Quenching Buffer	50 mM NH_4Cl in PBS
RIPA Buffer	50 mM Tris, pH 7.5, 150 mM NaCl, 0.1% SDS, 0.5% sodium deoxycholate and 1% Triton X-100, supplemented with 1x protease inhibitor cocktail
TBST	5 mM sodium acetate, 1 mM EDTA, 20 mM Tris HCl, 135 mM NaCl, 1 M HCl pH 7.6, 0.1% Tween 20

Table 3: Buffers used in the "BAK assembles into smaller yet functional pores than BAX" study

Plasmids and cloning

All plasmids were generated using standard restriction digest and T4 DNA ligation except for the GFP(A207K)-plasmids and GFP-Bax(S184V) which were generated using site-directed mutagenesis PCR and DpnI digest. The CRISPR/Cas9 plasmids were generated according to the provided protocol by Feng Zhang (Addgene).

Plasmid	Features	Cloning details
GFP(A207K)-BAK	GFP(A207K)-Bak-Stop	GFP was mutated using mutagenesis PCR
GFP(A207K)-BAX	GFP(A207K)-Bax-Stop	GFP was mutated using mutagenesis PCR
GFP-BAK	GFP-Bak-Stop	Bak was inserted into Bax-GFP vector using HindIII and EcoRI enzymes
GFP-BAX	GFP-Bax-Stop	Provided by Dr. N Brady
GFP-BAX(S184V)	GFP-Bax(S184V)-Stop	Bax was mutated using mutagenesis PCR
mCherry-BAK	mCherry-Bak-Stop	Bak was inserted into pcDNA3.1 (-)-mCherry vector using HidIII and NheI enzymes
Mito-mMaple	Mito-mMaple-Stop	Previously generated in the lab
mTagBFP2-Tomm20-N-10	mTagBFP2-Tomm20-Stop	Addgene #55328
pSpCas9(BB)-2A-Puro (PX459)	hSpCas9-2A-Puro-Stop + cloning site for gRNA	Addgene # 48139
pSpCas9(BB)-2A-Puro (PX459) + BAK ko gRNA	hSpCas9-2A-Puro-Stop + BAK gRNA	BAK gRNA was introduced using BbsI enzyme
pSpCas9(BB)-2A-Puro (PX459) + BAX ko gRNA	hSpCas9-2A-Puro-Stop + BAX gRNA	BAX gRNA was introduced using BbsI enzyme
Smac-mCherry	Smac(aa-1-60)-mCherry-Stop	Provided by Dr. S. Tait
Tfam-GFP	Tfam-GFP-Stop	Previously generated in the lab

Table 4: Plasmids used in the "BAK assembles into smaller yet functional pores than BAX" study

Following procedure was used for the cloning with restriction digest and T4 DNA ligation.

(i) The cDNA of the insert was amplified Q5 High-Fidelity DNA Polymerase. The PCR reaction and settings for the amplification were (Table 5, 6):

cDNA	50 ng
5x Q5 Reaction Buffer	10 µl
5x Q5 high GC Enhancer	10 µl
10 mM dNTPs	1.5 µl
10 µM forward Primer	2.5 µl
10 µM reverse Primer	2.5 µl
Q5 DNA Polymerase	0.5 µl
Nuclease free water	Up to 50 µl

Table 5: General composition of a PCR reaction

Step	**Temperature**	**Duration**
Initial Denaturation	98°C	30 sec
1. Denaturation: 35 Cycles	98°C	10 sec
2. Annealing: 35 Cycles	60°C	30 sec
3. Elongation: 35 Cycles	72°C	30 sec
Final Elongation	72°C	2 min

Table 6: PCR program

(ii) The PCR product was purified using the GeneJET PCR purification kit (VWR).

(iii) The PCR product and the destination vector were digested with the restriction enzymes. Digestion was usually performed at 37°C for 2h, otherwise NEB instructions were followed. Afterwards, PCR product and vector were purified using an agarose gel and the gel purification kit (Qiagen) and their concentration was determined.

(iv) Ligation of the PCR product and destination vector was performed in a 1:3 or 1:7 molar ratio of vector:insert using T4 DNA ligase. The ligation reaction was incubated for 1 h at room temperature and 4°C overnight.

(v) The ligation reaction was transformed into electro-competent DH5α and incubated at 37°C overnight on LB agar plates with antibiotics.

(vi) Single colonies were selected from the LB agar plates and the plasmid DNA was isolated using E.N.Z.A. ® Plasmid Mini Kit II (VWR). The concentration of the isolated DNA was determined and it was sent for sequencing (GATC) to verify correct insertion of the cDNA into the destination vector.

Following steps were used for cloning using site-directed mutagenesis PCR:

(i) Overlapping primers containing the desired mutation were designed and mutagenesis PCR was performed with the following reaction composition and settings:

Plasmid	100 ng
5x Q5 Reaction Buffer	10 µl
5x Q5 high GC Enhancer	10 µl
10 mM dNTPs	1.5 µl
10 µM forward Primer	2.5 µl
10 µM reverse Primer	2.5 µl
Q5 DNA Polymerase	0.5 µl
Nuclease free water	Up to 50 µl

Table 7: Composition for site-directed mutagenesis PCR reaction

Step	**Temperature**	**Duration**
Initial Denaturation	98°C	3 min
i. Denaturation: 35 Cycles	98°C	10 sec
ii. Annealing: 35 Cycles	60°C	30 sec
iii. Elongation: 35 Cycles	72°C	2-3 min
Final Elongation	72°C	2 min

Table 8: Program for site-directed mutagenesis PCR

(ii) The PCR product was digested using the restriction enzyme DpnI at 37°C for 4h.

(iii) After digestion, the PCR product was purified using an agarose gel and the gel purification kit (Qiagen).

(iv) The PCR product was transformed into electro-competent DH5α and incubated at 37°C overnight on LB agar plates with antibiotics.

(v) Single colonies were selected from the LB agar plates and the plasmid DNA was isolated using E.N.Z.A. ® Plasmid Mini Kit II (VWR). The concentration of the isolated DNA was determined and it was sent for sequencing (GATC) to verify correct mutagenesis.

Mammalian cell culture

HCT116 and U2OS cells were maintained in McCoy's 5A and Dulbecco's Modified Eagle's Medium (DMEM), respectively, supplemented with 10% fetal bovine serum (FBS) and 1% Penicillin/Streptomycin at 37°C and 5% CO_2.

Transfection of expression plasmids in mammalian cell culture

For all cell experiments, HCT116 and U2OS cells were seeded two or one day before transfection, respectively. Cells were transfected at a confluency of 80%, exact cell numbers and the composition of the transfection mix are listed in table 9.

Well size	Cell number (seeded)	µg of DNA	µl of Lipofectamine	Volume OptiMEM (one mix)
µ-Slide 8 Well (IBIDI)	0.08-0.12x10^5	0.05	0.15	25
µ-Dish 35 mm (IBIDI)	1-1.5x10^5	0.1-0.3	0.3-0.9	50
12-well plate	0.5-0.8x10^5	0.1-0.2	0.3-0.6	50
6-well plate	1-2x10^5	0.1-0.5	0.3-1.5	100

Table 9: Cell numbers and transfection mix compositions

For transfection the following steps were performed:

(i) The medium in the wells for transfection was aspirated and new medium was added.

(ii) In tube one the plasmid DNA was diluted in OptiMEM (mix 1) and in a second tube the Lipofectamine 2000 was diluted in OptiMEM (mix 2). The exact amount of DNA and Lipofectamine 2000 are listed in table X. DNA and Lipofectamine 2000 was used in a 1:3 ratio (1 µg of DNA = 3 µl of Lipofectamine 2000).

(iii) The mixes were incubated for 5 min at room temperature and combined afterwards.

(iv) The combined mixture was incubated for 20 min at room temperature and added dropwise to the well.

(v) The cells were incubated at 37°C and 5% CO_2 for 16 h before testing for transgene expression and experiment performance.

Apoptosis induction

For apoptosis induction, cells were incubated in 1 µM staurosporine (STS) at 37°C and 5% CO_2 for 3h. For Correlative Fluorescence and Super-resolution microscopy and Airyscan detection a combination of 1 µM ABT-737, 1 µM S63845 and 10 µM qVD-OPh was used as an apoptotic trigger.

Mitochondria staining

Cells were incubated with MitoTracker™ Deep Red (100 nM) for 30 min and washed afterwards three times with PSB. For the measurement of the mitochondrial membrane potential cells were stained with TMRE (200 nM) for 30 min and afterwards washed three times with PBS.

CRISPR/Cas9 knockout of BAK or BAX

To generate a knockout of either BAK or BAX in HCT116 cells the following protocol was used. HCT116 cells were seeded in a 6-well plate two days before transfection. For the generation of a HCT116 BAK ko cell line, the gRNA “ACGGCAGCTCGCCATCATCG” was used and for HCT116 BAX ko the gRNA “CTGCAGGATGATTGCCGCCG”. The CRISPR/Cas9 plasmids were generated according to the provided protocol by Feng Zhang (Addgene). The following steps were performed to generate knockout cell lines:

(i) HCT116 cells were transfected with pSpCas9(BB)-2A-Puro (PX459) + Bak ko gRNA to generate a HCT116 BAK ko cell line or pSpCas9(BB)-2A-Puro (PX459) + BAX ko gRNA to generate a HCT116 BAX ko cell line. 500 ng of plasmid and 1 µl of Lipofectamine 2000 was used for one 6-well. 2 h after transfection the medium was replaced by new medium.

(ii) 48 h after transfection, the cells were trypsinized and transferred to a 15-cm dish and selection medium containing 0.5 µg/ml puromycin was added. The optimal puromycin concentration for the selection of transfected cells was determined beforehand. 15-cm dishes were chosen because they granted single colony dilution after selection.

(iii) The selection medium was changed every other day for 7-10 days until the single colonies were big enough to be picked and transferred to a 12-well plate. Single colonies were picked using glass cylinders and trypsinization.

(iv) The different cell clones were tested for correct knockout by Western blotting and genomic sequencing.

Fluorescence microscopy

Confocal microscopy was performed in a Zeiss LSM 710 ConfoCor3 microscope (Carl Zeiss Microimaging). For Airyscan detection, a Zeiss LSM 780 NLO equipped with an Airyscan module was used. Transmitted light and fluorescence images were acquired through a Zeiss C-Apochromat 40x, NA 1.2 water immersion objective or 63x, NA 1.4 oil immersion objective onto the sample. The samples were excited using 405 nm, 488 nm and 561 nm lasers. The microscope is equipped with an incubator for live cell imaging (37°C and 5% CO_2). Image analysis was performed using ImageJ.

Live-cell microscopy of apoptosis in single cells

HCT116 or U2OS cells were seeded in a µ-Slide 8-well (IBIDI) two and one day before transfection, respectively. For the quantification of the time point of Smac release and BAK foci formation, 50 ng of GFP-BAK and 50 ng Smac-mCherry were transfected. For the investigation of temporal and spatial co-localization of BAK and BAX, 50 ng of mCherry-BAK and 50 ng of GFP-BAX was transfected. The mitochondria were either visualized using MitoTracker™ Deep Red staining (100 nM) or using transfection with mTagBFP2-Tomm20. Transfection was performed 16 h before microscopy. For live-cell imaging, Zeiss LSM 710 ConfoCor3 microscope equipped with an incubator (37°C and 5% CO_2) was used. The images were acquired through a Zeiss C-Apochromat 40x, NA 1.2 water immersion objective. The µ-Slide 8-well was placed under the microscope and a cell with desired transfection was chosen. After the cell was chosen, the microscopy medium was replaced by apoptosis-inducing medium containing 1 µM staurosporine. The cell was imaged every two minutes until apoptotic cell death and cell breackdown.

GUV permeabilization assay

GUVs were produced by electro-formation and the experiments were done as described in (Bleicken, Wagner, & García-Sáez, 2013). Briefly, 2.5 µl of a 2 mg/ml Egg PC:CL 80:20 lipid mixture solution, doped with the lipophilic membrane dye DiI (ThermoFisher) and

dissolved in chloroform, were spread on each platinum electrode of an electro-formation chamber and immersed in 300 mM sucrose. Electro-formation proceeded for 2 h at 10 Hz, followed by 30 min at 2 Hz. 50 µl of the GUVs suspension was added to a solution of PBS buffer mixed with the appropriate concentrations of the proteins of interest in Lab-Tek 8-well chamber slides (NUNC) to a final volume of 200 µl. To measure membrane permeabilization in steady-state conditions, a Cytc488/APC mixture solution was added after 1-hour incubation with cBid-activated Bak. Images were collected 30 min later. The percentage of GUVs internalizing the fluorescent probes was determined by the GUVdetector software described in (Hermann, Bleicken, Subburaj, & García-Sáez, 2014).

Airyscan detection of mitochondrial DNA release

For Airyscan detection, U2OS cells were seeded in a µ-Dish$^{35\ mm,\ high}$ Grid-500 Glass Bottom (IBIDI) and transfected with 100 ng of Smac-mCherry and TFAM-GFP 16 h before experiment. The following procedure was used for Airy scan detection of mitochondrial DNA release:

(i) The confocal microscope was used to choose cells that were double transfected with Smac-mCherry and TFAM-GFP within the grid.

(ii) The microscopy medium was replaced by apoptosis-inducing microscopy medium containing 1 µM ABT-737, 1 µM S63845 and 10 µM QVD-OPh.

(iii) An image of the chosen cells was taken every 2 min. The time point of Smac release from the mitochondria to the cytoplasm was noted.

(iv) After some/most of the chosen cells released the Smac but latest after 60 min after the first cell released their Smac, cells were fixed by incubation with 4% paraformaldehyde in DMEM. Cells were washed three times with PBS and stored in PBS at 4°C if not proceeded with the experiment directly.

(v) For the immunostaining of the mitochondria, the cells were permeabilized with 0.25% Triton-X in PBS for 8 min. Afterwards, cells were washed three times for 5 min with PBS and incubated in Blocking Buffer (IF) for 45 min. Cells were incubated with α-Tomm20 (1:100 dilution in Blocking Buffer (IF)) for 45 min. Cells were washed three times for 5 min with PBS. Cells were incubated in the secondary antibody AF633 anti-rabbit 1:200 diluted in Blocking Buffer (IF) for 45 min. Cells

were washed three times for 5 min with PBS. If not proceeded directly with microscopy, samples were stored at 4°C.

(vi) For the Airyscan detection, the Zeiss LSM 780 NLO equipped with an Airyscan module was used. The images were acquired using a 63x, NA 1.2 water immersion objective. The cells chosen before were relocated using the grid position. For image processing the ZEN software and for image analysis ImageJ was used.

Photon counting confocal microscopy and assembly kinetics

Confocal microscopy was performed on a LSM 710 (Carl Zeiss Microimaging) inverted microscope equipped with a Plan-Apochromat 63x/1.4 oil immersion objective (Zeiss) and an Argon LASER (LGN 3001, Lasos Lasertechnik). Pinhole size was adjusted to yield a depth of field of 1 Airy unit (~800 nm for GFP emission). Before imaging, the growth medium was changed to 200 µl of phenol-red free DMEM and cells were maintained at 37 °C and 5% CO 2 during imaging. Cells were imaged by selecting a region of interest (ROI) and finding the focal plane of the cell using the 'fast' scanning mode of the microscope with a greatly reduced laser power. Then, z-stacks of 8 images were collected with an interval of 300 nm, which was set based on the point-spread function analysis of fluorescent beads as the maximum interval required to record at least 80% of the maximum possible intensity from any point source. Images of 44.98 x 44.98 µm (512x512 pixel, pixel size 0.9 µm) were acquired with a laser pixel dwell of 3.15 µsec and an averaging of 2 images. Single emission photons were detected on an Avalanche Photodiode (APD) detector. Kinetics analysis of GFP-BAK or GFP-BAX oligomerization was performed by photon-counting fluorescence microscopy acquiring z-stacks every 35 seconds for initial time point experiments (for a maximum duration of 5 minutes), or every 5 minutes (for a time series of 60 minutes) after MOMP. MOMP was indicated by the release of Smac-1-60-mCherry from mitochondria to the cytosol.

Stoichiometry analysis by a ratiometric approach

Single-particle detection and brightness analysis were performed on maximum intensity z-projections of individual time points, using an in-house python algorithm. Selected particles were defined by a region of interest (ROI) of defined pixel size (2 pixels in radius) and fitted to two-dimensional (2D) Gaussians. Background subtraction was performed by defining a ROI around the particle´s ROI having a larger pixel size (3 pixels in radius). Localized particles were filtered based on the width of the 2D Gaussian, which is indicative of the presence of multiple particles in the same ROI. Specifically, we implemented a method that allows detecting two or more adjacent particles in one ROI by measuring the full width

at half maximum (σ) of the fitted 2D Gaussian curves. After plotting σ values of all ROIs as a normal distribution, those ROIs whose σ fell out the 95th percentile of the distribution were excluded, as the bigger σ value is likely indicative of the presence of more particles in these ROIs. Importantly, particles whose intensity was maximum in the outer frames were also discarded, as intensity information could be lost. The stoichiometry (or molecularity) of GFP-BAX or GFP-BAK foci M_p were quantified by ratiometric comparison of their fluorescence intensity Ip to the fluorescence intensity of a standard I_s, of known stoichiometry M_s, tagged with the same fluorescent dye as the protein of interest, according to the formula:

$$Mp = Ip\ Ms / Is$$

As an internal standard, we used the 32-mer EGFP-tagged nuclear pore complex protein Nup96, endogenously expressed in the same cell line (Thevathasan et al., 2019). We additionally confirmed the validity of this standard by ratiometric comparison of the fluorescent intensity of Nup96-mGFP complexes with the one of recombinant mEGFP-ferritin, which assembles as a 24-mer (Liße et al., 2017). For each cell, the standard fluorescence intensity i_s was obtained as the mean value of the Gaussian-fitted fluorescence intensity distribution of Nup96-mGFP oligomers within the cell. I_s represents the average value of i_s from at least 5 different imaged cells, measured on the same day of the experiment. For a given cell, at each time point, the values in molecular units for detected GFP-BAX or GFP-BAK foci were plotted as a probability density function or as cumulative counts. Exponential decay fitting of the cumulative distribution provided the average molecularity of mGFP-BAX or mGFP-BAK foci of individual cells at each time point.

Single-molecule localization microscopy

For the SMLM imaging, a 100 mW 647 nm Coherent Obis Solid State Laser was collimated and focused at the Back Focal Plane of a 100 x Apochromatic TIRF objective lens to deplete and excite ATTO 647 labelled entities within a 12 um circular region. Activation of depleted molecules was controlled by manually tuning the power of a 405 nm laser to achieve constant density of active molecules throughout the acquisition period. Focus was maintained to +/- 20 nm in the lateral position with the aid of a back-reflected IR solid state laser and a piezo-stage interfaced through a PID circuit. The resulting fluorescence emission was filtered using a 700 / 75 nm band pass filter and imaged on the chip of an Electron Multiplying Charge Coupled Detector (EMCCD). Acquired images were analyzed

using thunderSTORM ®. Spots were detected using a difference of Gaussians and fitted to Gaussian profiles using the Least Square method. The uncertainty in the fitting procedure combined with the sigma of the fitted Gaussians were both used to improve the quality of the image and discard false and / or unsatisfactory localizations.

Preparation for SMLM

HCT116 or U2OS cells were seeded on µ-Dish$^{35\ mm,\ high}$ (IBIDI) and transfected with 300 ng of the GFP-Bak plasmid 16 h before the experiment. Apoptosis was induced by incubating the cells with 1 µM STS for 3 h. The following procedure was used to prepare the samples for Single Molecule Localization Microscopy (SMLM):

(i) For cell fixation, cells were incubated with 4% paraformaldehyde in DMEM for 10 min

(ii) Cells were washed twice with PBS and incubated in Quenching Buffer for 15 min

(iii) For cell permeabilization, cells were incubated with 0.25% Triton-X in PBS for 8 min. Afterwards, cells were washed three times for 5 min with PBS

(iv) Cells were incubated in Blocking Buffer (IF) for 45 min

(v) Cells were incubated with the nanobody FluoTag-Q anti-GFP Alexa Fluor 647 in a 1:1000 dilution in Blocking Buffer (IF) for 1.5 h. Cells were washed three times for 5 min with PBS. If not used directly afterwards for imaging, samples were stored in PBS at 4°C.

(vi) For imaging, PBS was replaced by Blinking Buffer

Correlative live cell confocal and super-resolution microscopy

HCT116 or U2OS cells were seeded on µ-Dish$^{35\ mm,\ high}$ Glass Bottom (IBIDI) and transfected with 300 ng of the GFP-Bak plasmid 16 h before the experiment. The following steps were performed:

(i) The confocal microscope was used to choose cells with GFP-BAK transfection within the grid.

(ii) The microscopy medium was replaced by apoptosis-inducing microscopy medium (containing 1 µM ABT-737, 1 µM S63845 and 10 µM QVD-OPh) and an image of

the chosen cells was taken every 2 min. The time point of Bak foci formation was noted.

(iii) After some/most of the chosen cells show BAK foci but latest after 60 min after the first cell showed BAK foci, cells were fixed by incubation with 4% paraformaldehyde in DMEM. Cells were washed three times with PBS and stored in PBS at 4°C if not proceeded with the experiment directly.

(iv) Immunostaining with the nanobody FluoTag-Q anti-GFP Alexa Fluor 647 was performed as described above (Preparation for SMLM).

(v) After nanobody staining, the samples were put under the super-resolution microscope and the chosen cells were relocated by their position in the grid.

Atomic force microscopy

SLBs were imaged using a JPK NanoWizard II system (JPK Instruments, Berlin, Germany) mounted on an Axiovert 200 Inverted Microscope (Carl Zeiss). Intermittent contact (IC or tapping) mode images were taken using V-shaped silicon nitride cantilevers with a typical spring constant of 0.09 N/m (SNL-10 Bruker). The cantilever oscillation was tuned to a frequency between 3 and 10 kHz, and the amplitude was set between 0.2 and 1 V. The amplitude was varied during the experiment to minimize the force of the tip on the bilayer. The scan rate was set between 0.5 and 1 Hz. The height, deflection and phase-shift signals were collected, simultaneously, in both trace and retrace directions. Roughness was measured as the average peak-to-peak distance in a cross-section of a bilayer. Images were processed by the JPK processing software, applying a smoothing function. Bilayer thickness was measured based on the height profiles from the mica (membrane defects or pores) to the membrane bulk. The height of the structures around the pores was measured based on the height profile from the membrane bulk.

Protein purification

Full-length mouse Bid and single-cysteine, full-length human Bax mutant (S4C, C62S and C126S), were expressed in Escherichia coli and purified as described elsewhere (Bleicken et al., 2010; Desagher et al., 1999). Caspase-8 was used to cleave Bid (cBid). Protein quality was checked by SDS–polyacrylamide gel electrophoresis. Mouse Bak carrying a

modified, more hydrophilic C-terminus (L192K, F193S, Y196D) (Leshchiner, Braun, Bird, & Walensky, 2013) and mutated to single-cysteine (C154S), was transformed into BL21 (DE3) RIPL cells (Stratagene, La Jolla, CA). Cultures were grown at 37°C in LB medium containing ampicillin (100 µg/ml) and chloramphenicol (35 µg/ml). Gene expression was induced by 1 mM IPTG (isopropyl-1-thio-β-D-galactopyranoside) at OD (600 nm) of 0.7. The temperature was lowered to 20°C, cells were harvested after an additional 16 h, frozen in liquid nitrogen and stored at -20°C. For purification, cells were resuspended in buffer A (1 M NaCl, 20 mM Tris, pH 8), ruptured by French press and separated by centrifugation. The Bak-containing supernatant was purified by incubation with chitin beads and treated for intein cleavage as described by the manufacturer (NEB) and further purified by size exclusion chromatography. Protein purity was analyzed by SDS-PAGE, LC-MS and western blot. For protein labelling, Atto 488 (Attotec, Siegen, Germany) dye was covalently attached to the single cysteine of Bax or Bak as described by the manufacturer. Excess of the label was removed by size exclusion chromatography. The activity of the unlabeled protein was tested by calcein assay as performed in (Bleicken, Wagner, et al., 2013). The activity of labelled proteins was controlled by giant unilamellar vesicle membrane permeabilization assay (Hermann et al., 2014). Labelling efficiency was calculated to be 75-82% for Bak and 84% for Bax by comparing protein and label concentrations with Bradford and spectrophotometer measurements.

Western Blot

The following steps were performed:

(i) To generate protein lysates of cells the cells were trypsinized and the cells and transferred to a centrifugation tube. The cells were pelleted (1500 rpm, 5 min, 4°C). The cell pellet was resuspended in RIPA buffer and incubated on ice for 20 min. The cell suspension was centrifuged (14000 rpm, 20 min, 4°C) and the supernatant was transferred to a new tube. The protein concentration of the supernatant was determined using Bradford.

(ii) 50 µg of protein was boiled (95°C) in protein loading buffer for 10 min and afterwards separated on a 12% polyacrylamide gel (120 V).

(iii) The gel was transferred to a PVDF membrane using semi-dry blotting (220mA, 1 h).

(iv) The membrane was stained with Pounceau S solution to check for successful blotting and equal protein loading. The membrane was incubating in destained by deionized water for some minutes.

(v) The membrane was blocked by incubating in 5% milk in TBST for 1 h. Afterwards, the membrane was incubated with the first antibody in TBST either for 1 h at room temperature or overnight at 4°C. The membrane was washed three times with TBST for 5 min and then incubated with the secondary HRP-conjugated antibody diluted in TBST for 1 h. The membrane was washed three times with TBST for 5 min.

(vi) The membrane rinsed with ECL solution (manufactory protocol) and was developed.

CHAPTER 3.

MERLIN: A novel BRET-based proximity biosensor for studying mitochondria-ER contact sites

Authors

Vanessa Hertlein[1], Hector Flores-Romero[1,2], Kushal K. Das[1], Sebastian Fischer[3], Michael Heunemann[4], Katharina Hipp[5], Klaus Harter[4], Julia C. Fitzgerald[6], Ana J. García-Sáez[1,2]

[1] Interfaculty Institute of Biochemistry, University of Tübingen, Tübingen, Germany

[2] Institute for Genetics and Cologne Excellence Cluster on Cellular Stress responses in Aging-Associated Diseases (CECAD), Cologne, Germany

[3] University of Heidelberg, Heidelberg, Germany

[4] Center for Plant Molecular Biology, University of Tübingen, Tübingen, Germany

[5] Max Planck Institute for Developmental Biology, Tübingen, Germany

[6] Hertie-Institute for Clinical Brain Research, University of Tübingen and German Centre for Neurodegenerative Diseases (DZNE), Tübingen, Germany

Authors Contribution

Vanessa Hertlein performed all experiments (except electron microscopy imaging, PDZD8 and neuron experiments) and analyzed all the data (except for PDZD8 and neuron experiments). Hector Flores-Romero performed and analyzed data of PDZD8 experiments and apoptotic and dynamic BRET assays. Ana J. Garcia and Sebastian Fischer designed MERLIN. Kushal K. Das and Sebastian Fischer cloned MERLIN constructs. Michael Heunemann assisted with FLIM-FRET imaging. Katharina Hipp performed and supervised electron microscopy imaging. Klaus Harter supervised FLIM-FRET imaging. Julia C. Fitzgerald provided material and supervised neuron experiments. Vanessa Hertlein wrote this thesis chapter based on the published article (Hertlein et al., 2020). Ana J. García-Sáez conceived the project and supervised the research.

RESULTS

Mitochondria and the endoplasmic reticulum (ER) are highly dynamic networks. They share subdomains of close proximity that are termed mitochondria-ER membrane contacts sites (MERCs). MERCs possess a distinct subset of proteins and act as platforms for many pivotal processes of the cell including calcium homeostasis and signaling, lipid biosynthesis, autophagy, mitochondrial dynamics and apoptosis. They are dynamic entities and several proteins have been described to be involved in the tethering of the contact sites and their regulation. Moreover, it has been reported that MERCs are altered in several human disorders including cancer, metabolic and neurodegenerative disease. Due to their importance for crucial cellular functions and their involvement in human disease, there is the requirement for the development of new techniques which enable the investigation of the spatiotemporal regulation and the molecular composition of MERCS. Here, we present a novel BRET-based biosensor termed MERLIN (Mitochondria-ER Length Indicator Nanosensor). The advantage of MERLIN over alternative tools is that MERLIN relies only on close proximity between the two organelles and not physical interaction that might create artifacts, affect viability or force the generation of contact sites. The applicability of MERLIN is demonstrated by the reversibility of changes in MERCs after drug treatment and by the characterization of the role of the mitochondrial dynamics machinery in MERCs regulation.

MERLIN correctly localizes at mitochondria and the ER

For the investigation of the spatiotemporal changes in MERCs and their molecular architecture, genetically encoded bifunctional BRET-based biosensors, termed MERLIN, were generated. The MERLIN biosensors are composed of two constructs made of a membrane targeting sequence, a linker system and one part of the complementary BRET pair (Figure 12A). The targeting of the biosensor to the mitochondrial membrane is achieved using the C-terminal domain (1-33 aa) of Bcl-xL (further termed B33C short for Bcl-xL-33-C). For the targeting of MERLIN to the ER membrane a truncated non-functional version of calnexin (further termed sCal) containing the ER-targeting sequence and the cytoplasmic C-terminus but lacking most of the luminal N-terminus, is used. To bridge the distance between the two organelles at the contact sites and to ensure proper energy transfer, the biosensors contain linkers of several lengths. A fully synthetic linker system consisting of $A(EAAAK)_nA$ repeats forming an α-helical structure is used. The α-helical structure is stabilized by salt bridges between the lysine and glutamate residues forming a quite rigid structure. This linker has been used in previous studies and were

demonstrated to be able to separate protein domains (Kolossov et al., 2008; Marqusee & Baldwin, 1987). To span different lengths up to a total distance of 24 nm, which should theoretically allow to cover the estimated MERCs distance, three linkers with different lengths were designed. Linker 1 (L1) is composed of four repeats corresponding to a theoretical length of 3 nm. Linker 2 and 3 (L2 and L3, respectively) consist of eight repeats with a theoretical length of 6 nm. While L1 and L2 can be used on their own, L3 needs to be combined with either L1 or L2. Combination of L1 and L3 results in a theoretical linker length of 9 nm and combination L2 and L3 in a length of 12 nm. To measure the close apposition between mitochondria and the ER, the MERLIN biosensors contain the BRET pair *Renilla* Luciferase 8 (RLuc) and mVenus (mVen) separated in each of the constructs targeted to mitochondria or the ER.

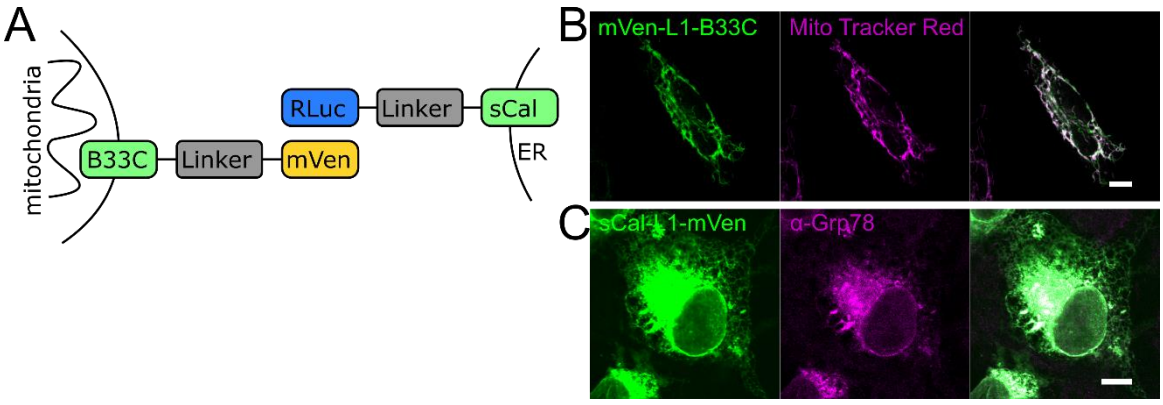

Figure 12: Rational design of MERLIN and subcellular localization of its components. A) *Scheme illustrating the structure of MERLIN. MERLIN is composed of a mitochondrial or ER targeting domain (green), a fully synthetic linker system (grey) and one part of the BRET pair Renilla Luciferase 8 (Rluc, blue) and mVenus (mVen, yellow) on each of the constructs. The mitochondrial part is targeted to the MOM by the C-terminal domain of Bcl-xL (B33C) while ER localization is achieved by a truncated non-functional version of calnexin (sCal). The membrane targeting domain and the BRET pair are separated by a synthetic linker system which can be combined in different ways to span a distance of up to 24 nm.* ***B)*** *Representative image of a Cos1 cell transfected with the mitochondrial MERLIN component, mVen-L1-B33C (green), and stained with MitoTracker Red (magenta). Scale bar 10 µm.* ***C)*** *Representative image of a Cos1 cell transfected with the ER-located MERLIN component, sCal-L1-mVen (green), and immunostaining against the ER-resident Grp78 (magenta). Scale bar 10 µm.*

Bioluminescence resonance energy transfer (BRET) follows the same physical principles as the more familiar Förster resonance energy transfer (FRET). Briefly, non-radiative energy transfer via dipole-dipole interaction occurs between two chromophores if the emission spectrum of the donor overlaps with the excitation spectrum of the acceptor, and the distance between donor and acceptor is smaller than 10 nm. The MERLIN setup hereby allows to detect close proximity between the two organelles without relying on the interaction of the two parts of the biosensor which is one of the main advantages of MERLIN. In contrast to FRET, where the two chromophores are fluorescent proteins, in BRET the donor is the enzyme luciferase, that oxidizes a substrate, the bioluminophore. The oxidation turns the substrate into its electronic excited state and the release of a

photon results in the return to the ground state. Hence, BRET does not rely on an external excitation, preventing photobleaching, phototoxicity and cross-excitation of the acceptor.

In a first step, we validated the correct localization of the MERLIN parts. To investigate the localization of the MERLIN constructs, Cos1 cells were transfected with either the mitochondrial or ER-resident MERLIN biosensor. mVen-biosensors were directly imaged using confocal microscopy while the RLuc ones were immunostained using an α-*Renilla* Luciferase antibody. Mitochondrial localization was confirmed by co-staining with MitoTracker red and ER localization was confirmed by immunostaining of the ER by α-Grp78 antibody. Figure 12B, C shows representative cells transfected with a MERLIN construct and labelled mitochondria or ER and clearly demonstrates the correct localization of the MERLIN constructs.

MERLIN expression has negligible effects on cell viability and MERCs

Next, we confirmed that the expression of MERLIN has negligible effects on cell viability and MERCs. To test for the effect of the MERLIN expression on cell viability, we analyzed the release of Smac from mitochondria. HCT116 WT (wild type) cells and stable MERLIN expressing HCT116 cells were transfected with Smac-mCherry and the release of Smac-mCherry was measured under healthy and apoptotic conditions. No significant difference in Smac release between HCT116 WT and MERLIN-expressing cells could be detected neither under healthy nor under apoptotic conditions.

To study whether the expression of MERLIN alters the abundance of the MERCs we analyzed the number of MERCs and the coverage of mitochondria with MERCs using transmission electron microscopy (Figure 13A). No difference in number and coverage could be detected between HCT116 WT cells and stable MERLIN expressing HCT116 cells. HCT116 WT cells showed 18.6% MERCs per mitochondria and a mitochondrial MERCs coverage of 2.8% while stable MERLIN HCT116 cells showed 19.2% MERCs per mitochondria and a coverage of 2.5%. (Figure 13 B) Of note, Tunicamycin treatment and starvation (Csordás et al., 2006; Yang et al., 2018) that previously have been reported to strengthen the contact between ER and mitochondria also showed an increased number of MERCs in stable MERLIN HCT116 cells. Tunicamycin treatment and starvation increased the percentage of MERCs per mitochondria to 25.8% and 39.7%, respectively. The coverage of mitochondria with MERCs for Tunicamycin-treated cells was comparable with non-treated cells (2.6 %) indicating that the number rather than the size of single

MERCs increased. For starved cells the coverage was drastically increased to 5.8%, the double of the coverage of untreated cells (Figure 13 B).

A

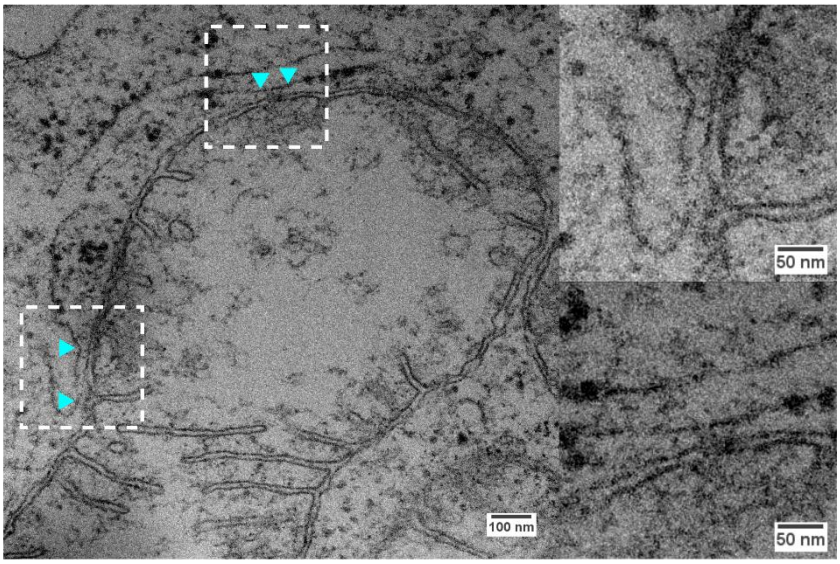

B

sample	no. Mito	no. MERCs	MERCs/Mito %	average length MERCs	coverage
HCT116 WT	167	31	18.6	259	2.8
HCT 116 + MERLIN	213	41	19.2	232	2.5
HCT116 + MERLIN + Tunicamcyin	163	42	25.8	251	2.6
HCT116 + MERLIN + Starvation	262	104	39.7	222	5.7

***Figure 13: MERCs structures visualized by transmission electron microscopy**. **A)** Representative images of mitochondria the ER and the MERCs structure of a HCT116 WT cell. Blue arrows mark the start and the end of a MERCs structure. Smaller panels on the right represent zoomed region of the white boxes in the main image. Scale bar: main image 100 nm, zoomed regions 50 nm. **B)** Number of mitochondria and MERCs as well as their dimensions for the different cell lines and treatments. Electron microscopy performed by Katharina Hipp.*

Systematic analysis of MERLIN performance using a quantitative BRET assay

After the verification of the correct localization and negligible effect of MERLIN expression on cell viability and MERCs, we carried out systematic analysis of MERLIN using saturation BRET assays. For the saturation BRET assay, Cos1 cells were co-transfected with constant amounts of donor biosensor (RLuc) plasmids and increasing amounts of acceptor biosensor (mVen) plasmids.

Before the systematic analysis was performed, several preliminary experiments were carried out for the optimization of the saturation assay and to confirm that it was performed under reproducible and reliable conditions. First, the optimal plasmid amounts for the donor and acceptor biosensor plasmid transfection were determined. A transfection with 100 ng of donor plasmid proved to be the lowest plasmid amount providing reliable protein

expression levels and bioluminescence signal. Acceptor plasmid amounts between 50 and 600 ng were used for the saturation assay and under the used conditions, amounts higher than 300 ng usually resulted in a saturation. Moreover, we verified that the increasing amount of acceptor biosensor plasmid transfection resulted in an increasing fluorescence signal. It was shown for different linker lengths and both organelle localizations that the increasing plasmid transfection indeed correlated linearly with increasing mVenus fluorescence signal (Figure 14A).

After the determination of the plasmid amounts for transfection, we checked whether the BRET ratio was independent of the amount of plasmid and thereby of the expressed protein. The BRET ratio was calculated as the acceptor emission relative to the donor emission and corrected by subtracting the background ratio value detected when only RLuc was expressed. A titration with increasing amounts of donor and acceptor plasmid in a 1:1 ratio demonstrated that the BRET ratio was independent of the plasmid amount over the range used (Figure 14B). Furthermore, using different linker combinations to achieve one specific linker length showed that the maximum BRET signal was independent of the linker combination (Figure 14C). For the following experiments, always the same linker length was used for the mitochondrial and the ER-resident biosensor, meaning for 6 nm linker length 3 nm + 3 nm were used. Coelenterazine H was the substrate used for the bioluminescence reaction. *Renilla* Luciferase 8 oxidizes Coelenterazine H which turns into its electronic excited state and a photon is released when it returns to the ground state. Using titration, it was confirmed that the concentration of Coelenterazine H has no influence on the BRET ratio and a concentration of 5 µM was chosen for all following experiments (Figure 14D).

Next, we performed a systematic analysis to figure out which linker length shows the highest sensitivity of the MERLIN biosensors containing 0, 6, 12 and 24 nm linkers. Both, the donor targeted to the mitochondria and acceptor targeted to the ER and vice versa were tested. All tested conditions showed a saturation curve indicating specificity (Figure 14 E, F). For the MERLIN constructs with the 6 nm and 12 nm linker the highest BRET signal was obtained. Interestingly, for all linker lengths an approximately three times higher BRET ratio was measured when the donor was located at the ER compared to the donor targeted to mitochondria. (Figure 14G) This difference might result from a higher efficiency of the active co-translational insertion of ER membrane proteins compared to the passive post-translational insertion into the MOM.

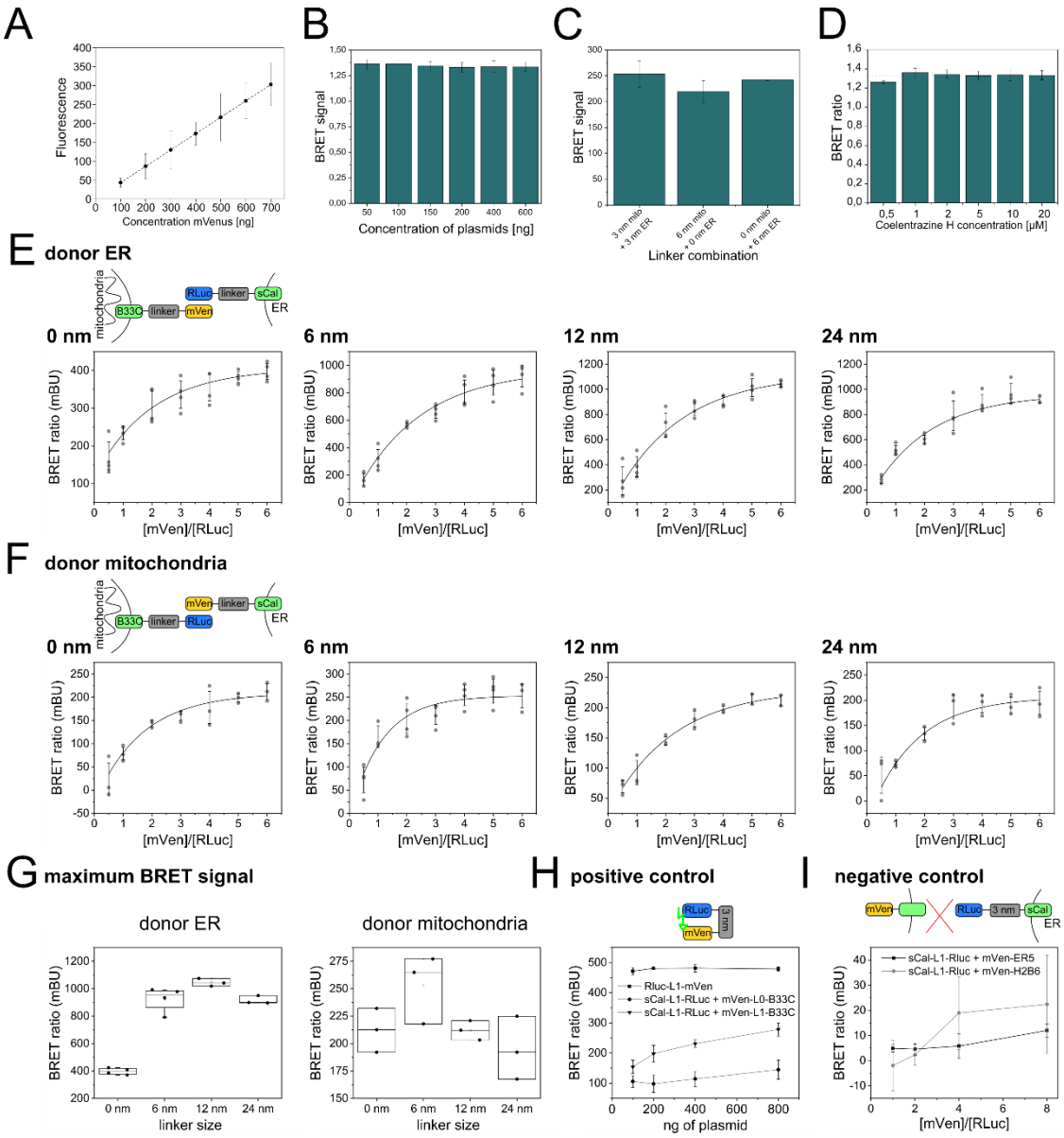

Figure 14: Systematic analysis of MERLIN performance using saturation BRET assays. A) Fluorescence signal of mVenus for different amounts of transfected mVenus plasmid (Mean ± SD, n=4). **B)** BRET signal for different transfections of equimolar amounts of RLuc/mVen plasmids (Mean ± SD, n=3). **C)** BRET signal for different linker combinations resulting in a total linker length of 6 nm (Mean ± SD, n=3). **D)** BRET ratio of different Coelenterazine H concentrations (Mean ± SD, n=3). **E)** Scheme for MERLIN with donor located at the ER and acceptor targeted to mitochondria and BRET saturation curves for 0, 6, 12 and 24 nm linker (n=4). **F)** Scheme for MERLIN with donor located at the mitochondria and acceptor targeted to the ER and BRET saturation curves for 0, 6, 12 and 24 nm linker (n=3). **G)** Maximum BRET signal for the different linker lengths and organelle localizations of the MERLIN components. **H)** BRET ratio of the negative controls with the ER located donor (sCal-L1-mVen) and acceptor in the lumen of the ER (mVen-ER5) or nucleus (mVen-H2B6) (Mean ± SD, n=3). **I)** BRET signal of the positive control mVen-L1-RLuc compared to MERLIN with the 3- and 6-nm linker lengths (Mean ± SD, n=3).

As positive control, a construct expressing RLuc and mVen in one polypeptide chain separated by a 3 nm linker ensuring close proximity and efficient energy transfer between the donor and the acceptor was used. This construct obtained higher BRET ratios than all the other MERLIN constructs. A more than four times stronger BRET ratio compared to the mitochondrial/ER located MERLIN constructs with a 3 nm linker, and approximately a

two times stronger ratio than for the 6 nm linker was measured. Of note, since in the positive control donor and acceptor exist in an equimolar ratio, also the mitochondrial and ER constructs were measured in an equimolar ratio which is the reason for the lower maximum BRET ratios compared to the saturation assay (Figure 14H).

As a negative control, biosensor combinations were used that are incapable to come into close apposition due to their localization to different cellular compartments. Figure 14I shows that the combination of the ER-resident donor with an ER lumen facing acceptor (mVen-ER5) or a nuclear located acceptor (mVen-H2B6) resulting in extremely low BRET ratios.

MERLIN is capable of sensing MERCs changes in apoptosis and alterations in PDZD8 protein levels

MERLIN was validated by demonstrating that the biosensors are capable of sensing significant signal changes under cellular conditions that are known to affect MERCs. For this purpose, we measured BRET signals under apoptotic conditions and in cells with increased or decreased protein levels of the tether PDZD8.

Previously, it has been reported that the contact sites between mitochondria and the ER are tightened during apoptosis, with increased contact number and decreased distance between the two organelles (Csordás et al., 2006). To test whether MERLIN is capable of sensing the difference in MERCs under apoptotic conditions, Cos1 cells were transfected with MERLIN constructs and apoptosis was induced by staurosporine. First, apoptosis progression was investigated, showing dramatic mitochondria fragmentation after 1h of apoptosis induction and membrane blebbing and cell shrinkage after 5h (Figure 15A). Next, the BRET signal was monitored for 5h after apoptosis induction and an increase in BRET signal was detected over time for all four linker lengths. Control cells, however, showed no significant difference in BRET signal over time, suggesting that the changes in BRET signal are due to tightened contacts in apoptotic cells (Figure 15B). Cell shrinkage and condensation of cellular components are hallmarks of apoptosis. To rule out that the increased BRET signals are due to cell shrinkage rather than tightened contacts we measured the BRET signal under caspase inhibited conditions. The inhibition of caspases efficiently prevented cell shape changes after apoptosis induction. However, the BRET signal was still increased in apoptotic cells indicating that the changes in BRET signal resulted indeed from tightened contacts between the mitochondria and the ER (Figure 15E).

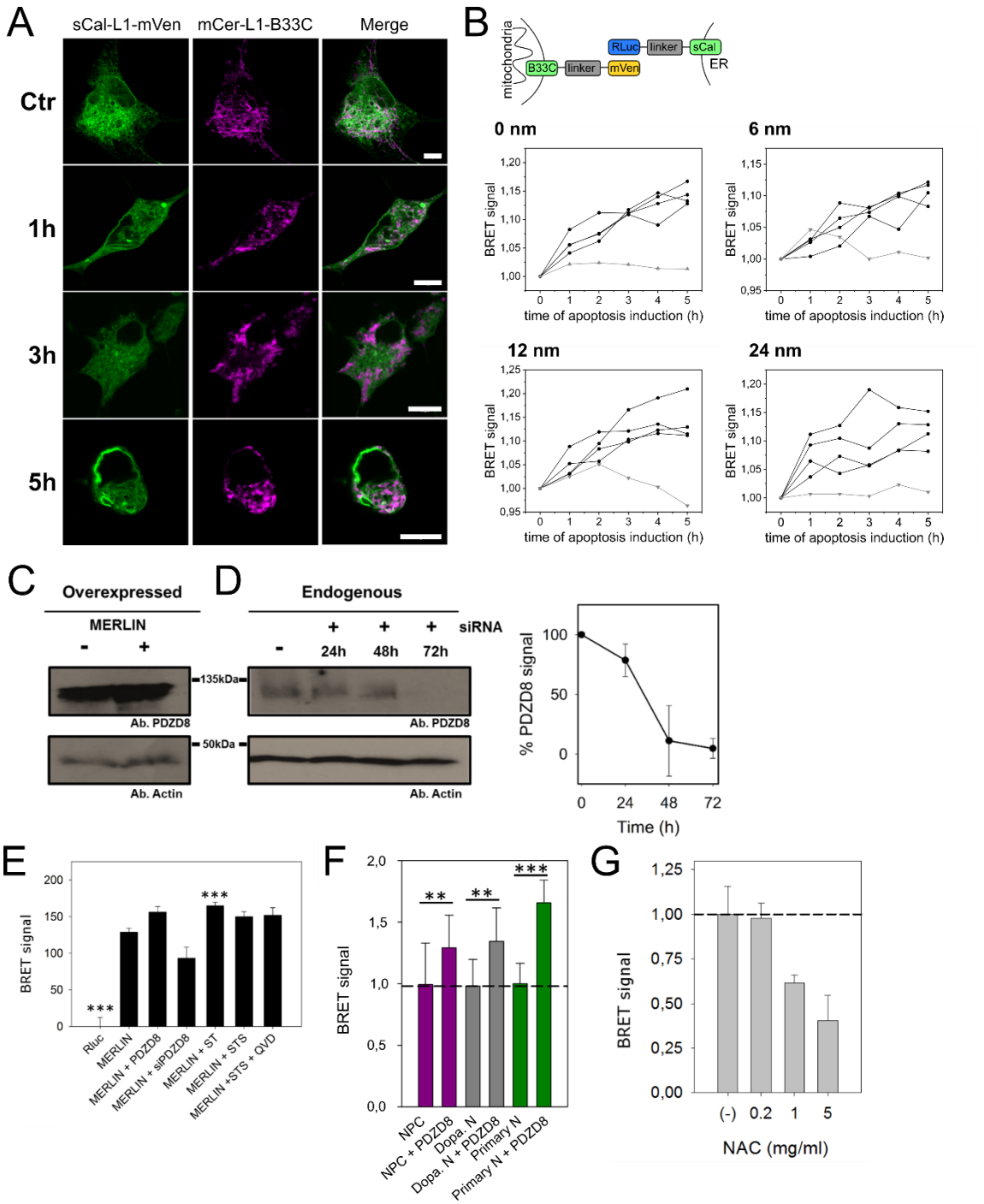

Figure 15: Validation of MERLIN by demonstrating sensitivity to MERCs changes under apoptotic conditions and under altered protein levels of the tether PDZD8. A) Representative images of Cos1 cells transfected with the mitochondrial biosensor (mVen-L1-B33C, green) and the ER targeted biosensor (sCal-L1-mCer, magenta) under healthy (0h) and apoptotic conditions 1h-5h after induction with staurosporine (STS). Scale bar 10 µm. **B)** Scheme and BRET signal over time in apoptotic cells for the different linker lengths. Black lines represent four individual measurements and the grey line the control measurement without induction of apoptosis. Apoptosis was induced at time point 0 h by addition of 1 µM STS (n=4). **C)** Western Blot showing the PDZD8 levels without and with overexpression of PDZD8 in HCT116 WT cells. **D)** Western Blot and quantification of the PDZD8 levels after siRNA knockdown in HCT116 WT cells. **E)** BRET signal in cells co-expressing Rluc-L1-B33C and Scal-L1-mVenus biosensor combination, in the presence of overexpressed PDZD8, the synthetic tether mTagBFP2 and PDZD8 knockdown in HCT116 cells. (**P < 0.025, ***P ≤ 0.001). t test, data are expressed as mean ± SD. **F)** Quantification of BRET signal in neuronal progenitor

cell (magenta) and dopaminergic neurons (grey) in the presence of absence of PDZD8. (**P < 0.025 and ***P < 0.001). T test, data are expressed as mean ± SD. **G)** BRET signal after treatment with different concentrations of NAC (**P < 0.025) t test, data are expressed as mean ± SD. Experiments C-E performed by Hector Flores-Romero. Experiments F-G performed in collaboration with Hector Flores-Romero.

Next, the sensitivity of MERLIN to detect changes induced by the alteration of the protein levels of PDZD8, a known MERCs tether protein, was studied. As expected, due to its tethering function, knockdown of PDZD8 resulted in a decreased BRET signal suggesting a loosening of the contact sites. On the contrary, overexpression of PDZD8 increased the BRET signal indicating a strengthening of MERCs. In agreement, overexpression of a synthetic tether, that physically links the ER and mitochondria (Hirabayashi et al., 2017), resulted in a similar increase in BRET signal as PDZD8 overexpression (Figure 15C-E). Of note, PDZD8 was first reported as a MERCs tether in neurons with a critical role in proper calcium transfer in the neuronal synapses. Neurons are sensitive cell types and their sensitivity to phototoxicity and difficulties with electron microscopy made it hard to study MERCs in these cells. MERLIN is capable to overcome these problems and to detect changes in MERCs induced by PDZD8 overexpression in neuronal progenitor cells and differentiated neurons (Figure 15F). These results demonstrated the possible applications for MERLIN in sensitive cell types like neurons.

Finally, N-acetylcysteine (NAC), a compound that increases the mitochondrial resilience by reducing oxidative stress and inflammation, is known to reduce interactions between the ER and mitochondria (Wright et al., 2015). NAC treatment was used to validate MERLIN. BRET assays demonstrated that indeed MERLIN is able to detect a reduction of proximity between the two organelles which is indicated by the decreased BRET signal after NAC treatment compared to untreated control samples (Figure 15G).

In summary, these results demonstrated that MERLIN is capable to detect a loosening or tightening of the ER and mitochondria at the contact sites for several conditions known to affect MERCs.

MERLIN-based FRET biosensors enable live single-cell analysis of the MERCs

BRET assays are a powerful straight-forward method for bulk live-cell high throughput screenings. However, single-cell microscopy analysis proved to be challenging due to low levels of photon emission and lack of sensitivity of the cameras. To overcome these difficulties and to enable single-cell microscopy analysis, FRET biosensors based on the MERLIN design were generated. In the FRET donor biosensor, the luciferase was replaced by a mCerulean3 (mCer) that is compatible with the acceptor mVen. Fluorescence lifetime imaging (FLIM)-FRET analysis was performed in single living Cos1

cells transfected with the 6 nm linker biosensors with both organelle localizations. As positive control, a construct containing both mCer and mVen in one polypeptide (mCer-L0-mVen) was used. As negative controls, a donor only (either mCer-L1-B33C or sCal-L1-mCer) control and spatially separated donor and acceptor biosensors (mCer-L1-B33C + A2A-mVen) were used.

The lifetime of the donor for the 6 nm linker biosensors was measured and compared to the positive and negative control. The lifetime of the donor is decreasing if there is FRET interaction indicating contact between the ER and mitochondria. The spatially separated control and donor only controls showed longest donor lifetimes (3.67 ± 0.08 ns and 3.70 ± 0.06 ns respectively). For the 6 nm linker biosensors, a significantly shorter donor lifetime was measured suggesting radiation-free energy transfer between the donor and acceptor and thereby interaction between the ER and mitochondria. Of note, the donor lifetime for both organelle localizations was similar (3.54 ± 0.06 ns for sCal-L1-mCer + mVen-L1-B33C and 3.50 ± 0.05 ns for mCer-L1-B33C + sCal-L1-mVen). The shortest donor lifetime was detected for the positive control which expresses mCer and mVen in one polypeptide chain (3.06 ± 0.17 ns) indicating the strongest FRET interaction. (Figure 16A, B)

FLIM-FRET analysis demonstrated that the MERLIN-based FRET biosensors offer the possibility of quantitative single-cell measurement of the proximity between the ER and mitochondria in live cells.

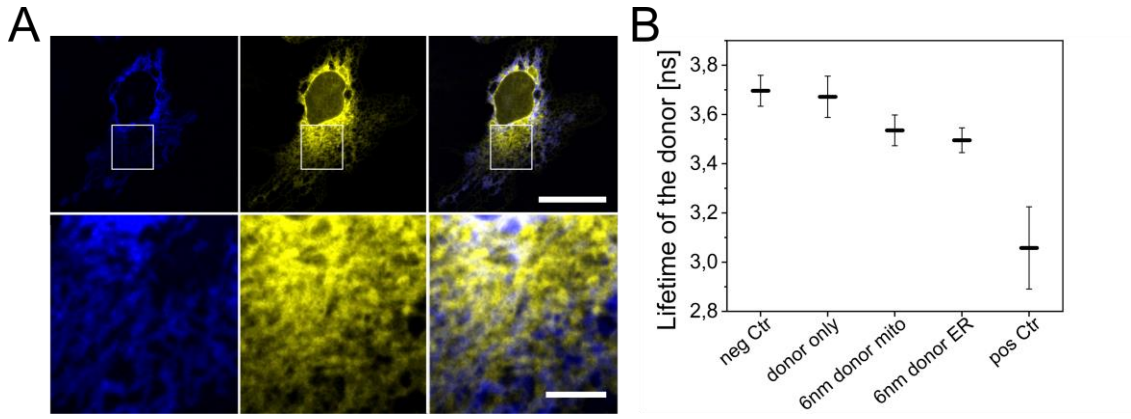

Figure 16: Analysis of MERCs of live single-cells using FLIM-FRET. *A) Upper panel shows a representative Cos1 cell transfected with mCer-L1-B33C (blue) and sCal-L1-mVen (yellow). Lower panel shows the zoom region represented by the white box in the upper panel. The region in the white box was used for FLIM-FRET measurement. Scale bar 25 µm upper panel and 5 µm lower panel. B) The fluorescence lifetime is shown for the donor fluorophore of the 6 nm linker MERLIN biosensors, the negative and the positive control as well as the donor only control. Graph shows three biological replicates with n = 10, Mean ± SD. Experiments performed in collaboration with Michael Heunemann.*

MERLIN detects dynamic alterations and the influence of the mitochondrial dynamics machinery on MERCs

The machinery of the mitochondrial outer membrane fusion, Mfn1 and Mfn2, has been reported to be involved in the contact sites between the ER and mitochondria. However, the exact role of Mfn1 and Mfn2 is still a matter of debate. One hypothesis claims that Mfn1 and Mfn2 act as tethers at the contact sites, while the opposing hypothesis states that they behave as an antagonist of a tether acting as a spacer to separate the ER and mitochondria (de Brito & Scorrano, 2008; Filadi et al., 2015; Naon et al., 2016).

To investigate the role of Mfn1 and Mfn2 in MERCs, BRET measurements were performed in Cos1 cells transfected with the MERLIN biosensors with siRNA knockdown of either Mfn1, Mfn2 or scramble siRNA as a control. Knockdown of Mfn1 and Mfn2 caused a dramatic change in mitochondrial shape and a mild change in ER morphology (Figure 17A). The BRET signal was decreased for cells knocked down for either Mfn1 or Mfn2 compared to the control cells with scramble siRNA knockdown (Mfn1 -8.5 ± 2.3% and Mfn2 -8.1 ± 2.0%). (Figure 17B) These results indicate decreased proximity between the ER and mitochondria in Mfn1 and Mfn2 knockdown conditions pinpointing in the direction of a tethering role for Mfn1 and Mfn2. However, it cannot be excluded that the sever mitochondrial fragmentation influenced or even caused the changes in MERCs.

Furthermore, in addition to the mitochondrial fusion machinery Mfn1 and Mfn2, the mitochondrial fission protein Drp1 was investigated. Drp1 has been reported to be recruited to MERCs to execute the mitochondrial division. Whether Drp1 has also a structural role in MERCs is unknown. In contrast to Mfn1 and Mfn2, knockdown of Drp1 caused elongated mitochondria and had no effect on the ER morphology (Figure 17A). Interestingly, knockdown of Drp1 also resulted in a decreased BRET signal compared to control cells (-7.5 ± 1.3%) (Figure 17B).

The contact sites between the ER and mitochondria are dynamic entities that change and react to the cellular conditions. For example, it has been reported that MERCs tighten under apoptotic or ER stress conditions. To further prove the power of the MERLIN biosensors and the advantage of proximity sensing over physical interaction, the ability of MERLIN to sense reversible changes of MERCs under stress conditions was demonstrated.

The stable HCT116 MERLIN cell line was treated with different compounds known to influence MERCs for four hours and allowed to recover for eight hours. BRET measurement was performed before treatment, four hours after treatment and after four

and eight hours of recovery. As a control, cells without treatment were used to demonstrate sthat measuring BRET was not influencing the contact sites.

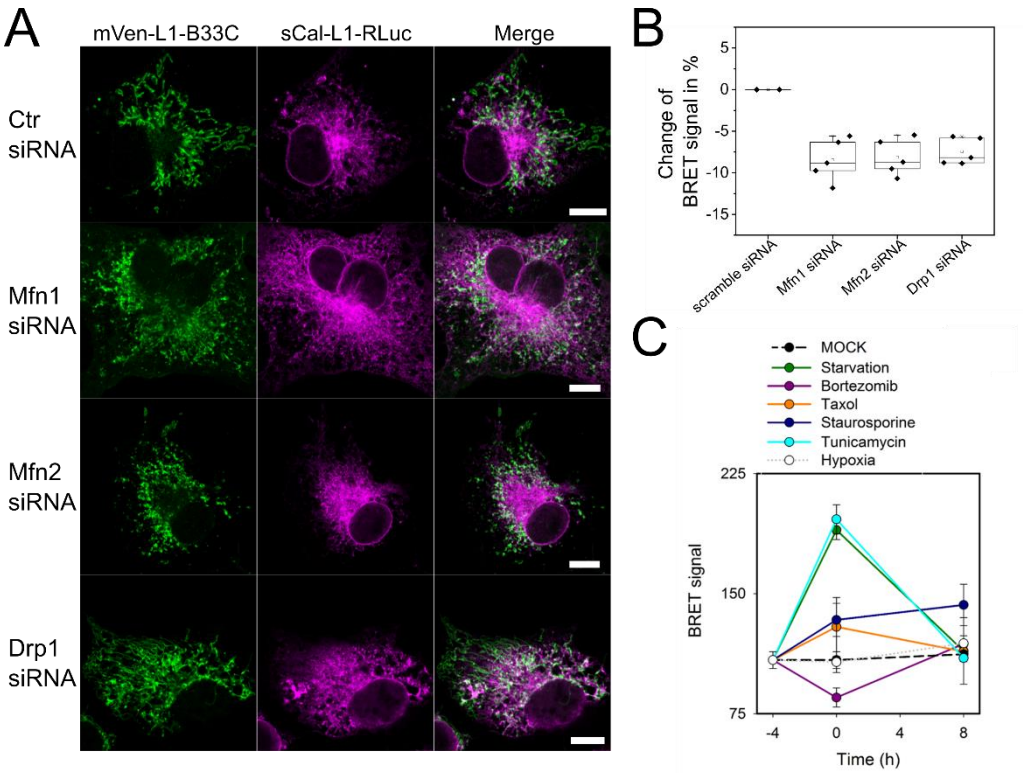

***Figure 17: MERLIN detects dynamic changes in MERCs**. A) Representative Cos1 cells transfected with mVen-L1-B33C (green) and sCal-L1-RLuc (magenta) after siRNA knockdown of Mfn1, Mfn2, Drp1 and scramble siRNA (control). B) Changes in percentage of BRET signal in cells co-expressing the 12 nm linker MERLIN sCal-L2-RLuc and mVen-L2-B33C after knockdown with Mfn1, Mfn2, Drp1, or scramble (Ctr) siRNA normalized to cells without knockdown. n = 3-4, Mean ± SD. C) Measurement of BRET signal of MERLIN as a function of time in HCT116 cells exposed to stress: starvation (green), Bortezomib (purple), Taxol (orange), staurosporine (dark blue), Tunicamycin (cyan), and hypoxia (grey). Control shown in black. BRET was quantified before treatment (−4 h), after 4 h of stress (0 h) and upon recovery at 4 and 8 h. (n=3, Mean ± SD). Experiments C performed in collaboration with Hector Flores-Romero.*

Serum starvation and Tunicamycin, which induces ER stress, have been shown previously in this chapter (Figure 13) and by others using electron microscopy to increase the interaction between the ER and mitochondria (Csordás et al., 2006; Yang et al., 2018). Serum starvation or treatment with Tunicamycin caused an increased BRET signal after four hours indicating stronger interaction between the ER and mitochondria. Serum addition and deprivation of the treatment after four hours resulted in a recovery of the cells and a return to BRET signals comparable to pretreatment levels after eight hours. Interestingly, treatment with Bortezombib, a drug also inducing ER stress resulted in a clear decrease in BRET signal indicating a loosening of the contact sites. Also for Bortezombib, a recovery of the BRET signal after removal of the treatment to levels comparable to those before the treatment could be observed. The opposing effects for Tunicamycin and Bortezombib might be explained by their different mechanisms of action. Tunicamycin blocks the N-linked glycosylation of proteins in the ER and thereby prevents protein folding and causes unfolded protein response. Bortezombib, on the other hand,

acts as a 26S proteasome inhibitor and causes ER stress as a secondary effect. Treatment with Taxol, a drug interfering with the cytoskeleton, which is also used in chemotherapy, slightly increased the BRET signal indicating a connection of the cytoskeleton and MERCs. Of note, addition of Monoethanolamine which was used to mimic hypoxic conditions had no effect on the MERCs. However, it cannot be excluded that stronger hypoxic condition which can be obtained by regulating levels of oxygen could influence MERCs. All tested treatments showed a recovery of the BRET levels after treatment deprivation indicating the possibility to measure plastic changes of MERCs using MERLIN. In contrast, treatment with staurosporine resulted in an increased BRET signal that cannot be recovered, which is in agreement with the irreversibility of the apoptotic process. (Figure 17C)

Altogether, MERLIN proved to be suitable to measure plastic interactions of MERCs and showed that alterations in the mitochondrial morphology machinery or the mitochondrial morphology itself influences the contact sites between the ER and mitochondria.

DISCUSSION

The mitochondria-ER membrane contact sites are distinct juxtaposed regions between the two organelles which are physically associated by protein tethers. They are crucial sites for inter-organelle communication and transport, including calcium signaling, lipid transport and apoptosis.

Here, we present the novel BRET-based biosensor MERLIN that enables reversible live-cell investigation of MERCs. MERLIN is a two-component biosensor with one component located to the mitochondrial outer membrane and one to the ER-membrane. BRET signal is obtained between *Renilla* Luciferase and mVenus when the two components come into close proximity with efficient energy transfer at a distance shorter than 10 nm. A modular linker system is used to bridge the distance between the organelle membranes. The linker lengths range from 0 to 24 nm. The linkers are rigid structures (Kolossov et al., 2008; Marqusee & Baldwin, 1987), however, the short connection between the membrane anchor and the linker allows free rotation which offers the sensor to adapt different 3D-conformations with the maximal distance that can be spanned being the sum of the two linker lengths and the size of the mVenus and the Luciferase.

We validated MERLIN by demonstrating its sensitivity to detect significant alterations in MERCs caused by perturbations that lead to concrete changes in MERCs. First, the MERLIN signal increased under apoptotic conditions, indicating closer interaction between the ER and mitochondria, which is in agreement with previous reports that show closer distance and higher numbers of MERCs under apoptotic conditions (Csordás et al., 2006). Second, overexpression or knockdown of PDZD8, a MERCs tether that is crucial for proper calcium transport in neurons, led to a significant increase or decrease in MERLIN signal, respectively (Hirabayashi et al., 2017). Third, expression of a synthetic tether that promotes the interaction between the two organelles also increased the MERLIN signal (Hirabayashi et al., 2017). Fourth, MERLIN-expressing cells treated with or without Tunicamycin or serum starvation were analyzed by BRET assays and electron microscopy, as an alternative approach. Tunicamycin treatment and starvation caused a increase in BRET signal and as previously reported an increase in the number of membrane contact sites between mitochondria and the ER (Csordás et al., 2006; Yang et al., 2018). In addition, comparing cells with and without MERLIN expression showed that MERLIN has no influence on cell viability or MERCs. Taken together, these results demonstrated the ability of MERLIN to sense changes in the distance between mitochondria and the ER.

The main advantage of MERLIN over the currently available biosensors is that MERLIN relies only on proximity sensing and does not need to establish artificial physical links between the organelles. SplitGFP and dimerization-dependent systems require the interaction of their two components, resulting in stable interactions that are irreversible which makes it impossible to measure dynamic and reversible processes (Cieri et al., 2018; Csordás et al., 2010; Pinaud & Dahan, 2011). The proximity sensing however, enabled us to detect plastic changes in MERCs after transient treatment with drugs causing alterations in MERCs. By following the kinetics of the BRET signal, we demonstrated that application of the drug caused a change in the BRET signal and after deprivation of the drug BRET signal recovered to steady-state levels.

Moreover, the stable interaction of the two components of the split-GFP and dimerization-dependent systems might cause enforced interaction of the organelles and thereby alter MERCs dynamics, composition or the cell homeostasis. MERLIN on the other hand, detects proximity between the two organelles without establishing a link. However, MERLIN detects all close apposition between the two organelles which might not limit the obtained signal exclusively to that of MERCs. Nevertheless, since MERCs are characterized by a very short distance of 10-30 nm, it is likely that the detected signal originates mainly from MERCs.

MERLIN enables high-throughput and straight-forward measurements in a multi-well format and can be applied for genetic or drug screenings. However, MERLIN measures the BRET signal of multiple cells and is not able to detect the number of contacts of a single cell, the contact area or dynamics of an individual contact. Furthermore, BRET measurement is difficult to perform on a single cell level using a microscopy approach because of low light emission and lack of sensitivity of most cameras. Thus, to provide the possibility to use MERLIN in single live cells to measure MERCs changes and dynamics, we generated a FRET biosensor based upon the MERLIN design. The *Renilla* Luciferase of the donor was replaced by a mCerulean3 that acts as a FRET donor for mVenus. We used FLIM-FRET measurement to demonstrate that this FRET-based biosensor is sensitive to MERCs. In contrast to the FRET system, the BRET-based biosensors offer a better signal-to-noise ratio and do not require donor illumination which prevents phototoxicity and crosstalk between the donor and acceptor. Due to these reasons MERLIN can be used in sensitive cell types like neurons.

Mitofusin 2 a component of the mitochondrial fusion machinery has been reported to be involved into the MERCs tethering. However, the exact role of Mfn2 is still a matter of debate with two contrary hypotheses. The first hypothesis claims that Mfn2 acts as a tether

at MERCs while the second hypothesis states that Mfn2 acts as a spacer keeping the two membranes at the correct distance (de Brito & Scorrano, 2008; Filadi et al., 2015; Naon et al., 2016). We used MERLIN to investigate the influence of knockdown of the mitochondrial morphology machinery proteins. ER-resident Mfn2 is assumed to form homo- and heterotypic interactions with mitochondrial Mfn2 and Mfn1 (Eura et al., 2003). Therefore, knockdown of Mfn1 should have a minor effect on MERCs because homotypic Mfn2-Mfn2 interactions are still possible. Mfn2 knockdown on the contrary should abolish all Mitofusin interactions between the ER and mitochondria and therefore have a more severe effect on MERCs than Mfn1. Knockdown of both Mfn1 and Mfn2 resulted in a dramatic fragmentation of mitochondria. Surprisingly, Mfn1 and Mfn2 knockdown showed the same level of decrease in the BRET signal. Next, we knocked down Drp1, the mitochondrial fusion protein and detected as expected a striking elongation of mitochondria. Nonetheless, Drp1 knockdown also resulted in a decrease in BRET signal. This raises the question, whether any alteration to the mitochondrial morphology impacts the interactions with the ER and suggests that acute morphological changes might have a dominant effect on MERCs.

To conclude, we presented MERLIN a proximity-based BRET biosensor for the investigation of MERCs. The main advantage of MERLIN is that it does not rely on physical interactions between the organelles and enables the measurement of dynamic processes and plasticity of MERCs. In addition, the BRET assays can be applied in high-throughput genetic or drug screenings and could be used for in vivo studies in mouse models since bioluminescence assays have already been established in this organism. The MERLIN biosensor could also be adapted to other organelle contacts by exchanging the targeting sequence of the constructs. And finally, we validated MERLIN by studying the effect of knockdown of the mitochondrial morphology machinery proteins on the contact sites between the ER and mitochondria, showing that the effect of acute alterations of the mitochondrial morphology seem to dominate over the effect of individual tethering proteins.

MATERIALS AND METHODS

Reagents

Product	Concentration	Source	Catalog no.
Bortezombib	50 nM		
Coelenterazine H	2 µM	Promega	S2011
DMEM		Sigma	D6046
DMEM phenol red free		Sigma	D5921
ECL Developer		Perkin Elmer	NEL103001EA
FBS	10%	Thermofisher	10270106
Glutaraldehyd	2%	Plano-em.de	R1020
Lipofectamine 2000		Invitrogen	11668019
McCoy		Sigma	M9309
McCoy phenol red free		Sigma	SH30270.01
MitoTracker™ Deep Red	100 nM	Thermofisher	M22426
Monoethanolamine	25 nM		
N-acetylcysteine	0.2-5 mM		
OptiMEM		Thermofisher	31985070
Paraformaldehyde	4%	VWR	PIER28908
PBS		Sigma	D8537
Penicillin/Streptomycin	1%	Sigma	P4333
Ponceau S		Carl Roth	5938.2
Prolong Gold Antifade Mountant		Thermofisher	P36934
Protease inhibitor cocktail	1x	Sigma	4693159001
PVDF membrane		Merck Millipore	IPVH00010
Staurosporine	1 µM	LC Laboratories	S3900
Taxol	15 µM		
TMRE	100 nM	Thermofisher	T669
Trypsin (10x)	1x	Sigma	59418C
Tunicamycin	25 nM		

Table 10: Reagents used in the "MERLIN: A novel BRET-based proximity biosensor for studying mitochondria-ER contact sites" study

Antibodies

Product	Dilution	Source	Catalog no.
AF488-anti mouse	1:200 (IF)	Thermofisher	A-11008
AF633-anti mouse	1:200 (IF)	Thermofisher	A-21052
AF633-anti rabbit	1:200 (IF)	Thermofisher	A-21070
Anti-mouse HRP-conj	1:10000 (WB)	Jackson Immuno	115-035-003
Anti-rabbit HRP-conj	1:10000 (WB)	Jackson Immuno	111-035-003
Dlp1	1:1000 (WB)	BD Biosciences	611113
Grp78	1:100 (IF)	Abcam	ab21685
Mitofusin 1	1:1000 (WB) 1:100 (IF)	Cell signalling	14739
Mitofusin 2	1:1000 (WB) 1:100 (IF)	Cell signalling	11925
PDZD8	1:1000 (WB)	Thermofisher	PA546771
Renilla Luciferase	1:100 (IF)	Abcam	ab185925

Table 11: Antibodies used in the "MERLIN: A novel BRET-based proximity biosensor for studying mitochondria-ER contact sites" study

Buffers

Name	Composition
6x Loading Buffer	4% SDS, 10% ß-mercaptoethanol, 20% glycerol, 0.004% bromophenol blue, 0.125 M Tris HCl pH 6.8
Blocking Buffer (IF)	1% BSA, 1% Tween20 in PBS
Blocking Buffer (WB)	TBS buffer supplemented with 5% (w/v) non-fat dry milk (Roth)
Blotting Buffer	20 mM Tris, 150 mM glycine, 0.02 % (w/v) SDS, 20 % (v/v) methanol in purified water
RIPA Buffer	50 mM Tris, pH 7.5, 150 mM NaCl, 0.1% SDS, 0.5% sodium deoxycholate and 1% Triton X-100, supplemented with 1x protease inhibitor cocktail
TBST	5 mM sodium acetate, 1 mM EDTA, 20 mM Tris HCl, 135 mM NaCl, 1 M HCl pH 7.6, 0.1% Tween 20

Table 12: Buffer used in the "MERLIN: A novel BRET-based proximity biosensor for studying mitochondria-ER contact sites" study

Plasmids and cloning

The MERLIN plasmids were generated using TOPO-TA cloning into pCR2.1-TOPO vector. The restriction enzymes NheI and BamHI were used for the insertion of the constructs into the targeting vector pcDNA3.1 (-) and XbaI and EcoRI for introducing the linker sequence (Eurofins-MWG). The protocol for cloning using restriction enzymes is described is Chapter 2, Materials and Methods section.

Plasmid	**Features**	**Cloning details**
A2A-mVen	A2A-mVen-Stop	Provided by P McCormick
mCer-L0-mVen	mCer-L0-mVen-Stop	Previously cloned in the lab
mCer-L1-B33C	mCer-L1-Bcl-xL(C-terminus 33aa)-Stop	Previously cloned in the lab
mVen-ER-5	mVen-ER-Stop	Addgene #56611
mVen-H2B-6	mVen-H2B-Stop	Addgene #56615
mVen-L1-B33C	mVen-L1-Bcl-xL(C-terminus 33aa)-Stop	Previously cloned in the lab
mVen-L2-B33C	mVen-L2-Bcl-xL(C-terminus 33aa)-Stop	Previously cloned in the lab
pCAG-mito-mTagBFP2	Mito-mTagBFP2-Stop	Addgene #105011
pCAG-PDZD8HA	PDZD8-Stop	Addgene #105005
pcDNA3.1 (-)	Empty vector	Thermofisher (V79020)
pCR2.1-TOPO	Empty vector	Invitrogen
RLuc-L1-B33C	*Renilla*-Luciferase-L1-Bcl-xL(C-terminus 33aa)-Stop	Previously cloned in the lab
RLuc-L1-mVen	*Renilla*-Luciferase-L1-mVen-Stop	Previously cloned in the lab
RLuc-L2-B33C	*Renilla*-Luciferase-L2-Bcl-xL(C-terminus 33aa)-Stop	Previously cloned in the lab
sCal-L1-mCer	sCal-L1-mCer-Stop	Previously cloned in the lab
sCal-L1-mVen	sCal-L1-mVen-Stop	Previously cloned in the lab
sCal-L2-mVen	sCal-L2-mVen-Stop	Previously cloned in the lab
sCal-L1-RLuc	sCal-L1-*Renilla*-Luciferase-Stop	Previously cloned in the lab

sCal-L2-RLuc	sCal-L2-*Renilla*-Luciferase-Sop	Previously cloned in the lab
Smac-mCherry	Smac(aa1-60)-mCherry-Stop	Provided by Dr. S Tait

Table 13: Plasmids used in the "MERLIN: A novel BRET-based proximity biosensor for studying mitochondria-ER contact sites" study

Mammalian cell culture

HCT116 and Cos1 cells were maintained in McCoy's 5A and Dulbecco's Modified Eagle's Medium (DMEM), respectively, supplemented with 10% fetal bovine serum (FBS) and 1% Penicillin/Streptomycin at 37°C and 5% CO_2.

Transfection of expression plasmids in mammalian cells

For all cell experiments, HCT116 and Cos1 cells were seeded two and one day before transfection, respectively. Cells were transfected at a confluency of 80%, the exact cell numbers and the composition of the transfection mix are listed in table 9.

For transfection the following steps were performed:

(i) The medium in the wells for transfection was aspirated and new medium was added.

(ii) In tube one the plasmid DNA was diluted in OptiMEM (mix 1) and in a second tube the Lipofectamine 2000 was diluted in OptiMEM (mix 2). The exact amount of DNA and Lipofectamine 2000 are listed in table X. DNA and Lipofectamine 2000 was used in a 1:3 ratio (1 µg of DNA = 3 µl of Lipofectamine 2000).

(iii) The mixes were incubated for 5 min at room temperature and combined afterwards.

(iv) The combined mixture was incubated for 20 min at room temperature and added dropwise to the well.

(v) The cells were incubated at 37°C and 5% CO_2 for 16 h before testing for transgene expression and experiment performance.

Transfection of siRNA in mammalian cells

HCT116 and Cos1 cells were seeded in a 6-well plate two and one day before siRNA transfection, respectively.

The following siRNAs were used for siRNA transfection: Mfn1 (J-010670-12-0002), Mfn2 (J-012961-05-0002), PDZD8 (L-018369-02-0005), scramble (D-001810-01-20) and Drp1 with a customized sequence (GGAGCCAGCUAGAUAUUAAUU) (Dharmacon).

For transfection the following steps were performed:

(i) The medium in the wells for transfection was aspirated and new medium was added.

(ii) In tube one 2 nM siRNA was diluted in 100 µl OptiMEM (mix 1) and in a second tube 1 µl Lipofectamine 2000 was diluted in 100 µl OptiMEM (mix 2).

(iii) The mixes were incubated for 5 min at room temperature and combined afterwards.

(iv) The combined mixture was incubated for 20 min at room temperature and added dropwise to the well.

(v) The cells were incubated at 37°C and 5% CO_2 for 48-72 h before experiment performance.

Transfection for quantitative BRET assays

Cos1 cells were seeded in a 12-well plate one day before transfection. Cells were transfected with 100 ng donor MERLIN biosensor (RLuc-plasmid) and increasing amounts of acceptor MERLIN biosensor (mVen-plasmids). 50, 100, 200, 300, 400, 500, 600 ng of the acceptor MERLIN biosensor was used. pcDNA3.1 (-), empty vector, was added to the DNA transfection mix to always have the same amount of plasmid DNA transfected (e.g. 100 ng acceptor MERLIN + 500 ng pcDNA3.1 (-) = 600 ng plasmid DNA).

The transfection was performed as described above (Transfection of expression plasmids). In mix 1, 100 ng donor MERLIN + 600 ng acceptor-pcDNA3.1 (-) were diluted in 50 µl OptiMEM. In mix 2, 1.5 µl Lipofectamine 2000 were diluted in 50 µl OptiMEM.

Mitochondria staining

Cells were incubated with MitoTracker™ Deep Red (100 nM) for 30 min and washed afterwards three times with PSB. For the measurement of the mitochondrial membrane potential cells were stained with TMRE (200 nM) for 30 min and afterwards washed three times with PBS.

Generation of stable cell lines

HCT116 cells were seeded in a 6-well plate two days before transfection. For the generation of a stable MERLIN cell line, the donor biosensor sCal-L2-RLuc and the acceptor biosensor mVen-L2-B33C were used.

The following steps were performed to generate knockout cell lines:

(i) HCT116 cells were transfected with 200 ng sCal-L2-RLuc and 200 ng mVen-L2-B33C. 1.2 µl of Lipofectamine 2000 were used for one 6-well. 2 h after transfection the medium was replaced by new medium.

(ii) 48 h after transfection, the cells were trypsinized and transferred to a 15-cm dish and selection medium containing 0.7 µg/ml G418 was added. The optimal G418 concentration for the selection of transfected cells was determined beforehand. 15-cm dishes were chosen because they granted single colony dilution after selection.

(iii) The selection medium was changed every other day for 14 days until the single colonies were big enough to be picked and transferred to a 12-well plate. Single colonies were picked using glass cylinders and trypsinization.

(iv) The different cell clones were tested for the expression of sCal-L2-RLuc and mVen-L2-B33C by Western blotting, microscopy and measuring of the BRET signal.

BRET assays

Quantitative BRET assay

Cos1 cells were seeded in a 12-well plate one day before transfection and transfected as described above (Paragraph “Transfection for quantitative BRET assay”). For the quantification it was essential to have a donor only control (triplicate). In addition, it was always performed a positive control (RLuc-L1-mVen) and a negative control (mVen-ER-5 + RLuc-L1-B33C or mVen-H2B-6 + sCal-L1-Rluc).

For quantitative BRET assays the following steps were performed:

(i) 16 h after transfection, cells were washed once with PBS, detached by trypsinization and transferred to an Eppendorf tube.

(ii) Cells were pelleted (3200 rpm, 5min) and washed twice with PBS. Cells were resuspended in PBS and diluted 1:20 in PBS.

(iii) 50 µl of the diluted cell solution was transferred to a white 96-well plate (Greiner) (triplicates). 5µM Coelenterazine H was added and was incubated for 10 min in the dark.

(iv) BRET measurement was carried out in a Tecan Infinite M200 plate reader. The BRET signal was calculated as the acceptor emission relative to the donor emission and corrected by subtracting the background ratio value detected when RLuc is expressed alone. For the analysis the following formula was used:

$$BRET\ signal\ [mBU] = \frac{\text{mVen emission}}{\text{RLuc emission}} - \frac{\text{mVen emission of RLuc only transfected cells}}{\text{RLuc emission of RLuc only transfected cells}} * 1000$$

Comparative BRET assay in apoptotic cells or after siRNA knockdown

Cos1 cells were seeded in a 6-well (siRNA knockdown) or 12-well (apoptosis) plate one day before transfection. For comparative BRET assay in apoptotic cells, cells without induction of apoptosis were used as a control. Apoptosis was induced with 1 µM staurosporine (STS) for 1 h to 5 h. For comparative BRET assay after siRNA knockdown, control siRNA (scramble) transfection and untransfected cells were used as a control. siRNA was transfected 48 h before BRET measurement. The following steps were performed for comparative BRET assay:

(i) 16 h after MERLIN transfection, for BRET assay in apoptotic cells, cells were treated for 1 h to 5 h with 1 µM STS. Afterwards, cells were washed once with PBS, detached by trypsinization and transferred to an Eppendorf tube.

(ii) Cells were pelleted (3200 rpm, 5min) and washed twice with PBS. Cells were resuspended in PBS and diluted 1:20 in PBS. For comparative BRET assay after siRNA knockdown, the cell solution that wasn't used for dilution is used for Western Blot to test for successful knockdown

(iii) 50 µl of the diluted cell solution was transferred to a white 96-well plate (Greiner) (triplicates). 5µM Coelenterazine H was added and was incubated for 10 min in the dark.

(iv) BRET measurement was carried out in a Tecan Infinite M200 plate reader.

BRET assay in HCT116 stable MERLIN cells

HCT116 stable MERLIN cells were seeded in a white 96-well plate (Greiner) two days before transfection or treatment. After treatment or transfection, cells were washed twice with PBS and PBS with 5 µM Coelenterazine H was added. The plate was incubated in the dark for 10 min and BRET measurement was carried out in a Tecan Infinite M200 plate reader.

BRET assay for characterization of MERCS plasticity

HCT116 stable MERLIN cells were seeded in a white 96-well plate (Greiner) two days before treatment.

(i) Cells were treated with 15 µM Taxol, 1 µM STS, 50 nM Bortezomib, 25 nM Monoethanolamin, 25 nM Tunicamycin, or deprived of FBS (starvation) for 4 h at 37°C and 5% of CO_2.

(ii) Cells were washed twice with PBS and PBS with 5 µM Coelenterazine H was added. The plate was incubated in the dark for 10 min at 37°C and 5% of CO_2 and BRET measurement was carried out in a Tecan Infinite M200 plate reader.

(iii) After measurement, the cells were washed twice with PBS and McCoy 5A medium supplemented with 10% FBS and 1% penicillin/streptomycin was added.

(iv) The cells were incubated for 4-16 h to allow recovery. After 4 h, 8 h and 16 h a second BRET measurement a described in (ii) was performed and fresh medium was added (iii) to continue recovery.

Western Blot

The following steps were performed:

(i) To generate protein lysates of cells the cells were trypsinized and the cells and transferred to a centrifugation tube. The cells were pelleted (1500 rpm, 5 min, 4°C). The cell pellet was resuspended in RIPA buffer and incubated on ice for 20 min. The cell suspension was centrifuged (14000 rpm, 20 min, 4°C) and the supernatant

was transferred to a new tube. The protein concentration of the supernatant was determined using Bradford.

(ii) 50 µg of protein was boiled (95°C) in protein loading buffer for 10 min and afterwards separated on a 12% polyacrylamide gel (120 V).

(iii) The gel was transferred to a PVDF membrane using semi-dry blotting (220mA, 1 h).

(iv) The membrane was stained with Pounceau S solution to check for successful blotting and equal protein loading. The membrane was incubating in destained by deionized water for some minutes.

(v) The membrane was blocked by incubating in 5% milk in TBST for 1 h. Afterwards, the membrane was incubated with the first antibody in TBST either for 1 h at room temperature or overnight at 4°C. The membrane was washed three times with TBST for 5 min and then incubated with the secondary HRP-conjugated antibody diluted in TBST for 1 h. The membrane was washed three times with TBST for 5 min.

(vi) The membrane rinsed with ECL solution (manufactory protocol) and was developed.

Fluorescence microscopy

Confocal microscopy was performed in a Zeiss LSM 710 ConfoCor3 microscope (Carl Zeiss Microimaging). Transmitted light and fluorescence images were acquired through a Zeiss C-Apochromat 40x, NA 1.2 water immersion objective or 63x, NA 1.4 oil immersion objective onto the sample. The samples were excited using 488 nm, 561 nm and 633 nm lasers. The microscope is equipped with an incubator for live cell imaging (37°C and 5% CO_2). Image analysis was performed using ImageJ.

Immunostaining of mitochondrial and ER-resident proteins

HCT116 and Cos1 cells were seeded on 18 mm glass coverslips in 12-well plates two or one day before transfection, respectively. The following steps were performed for immunostaining of mitochondrial and ER-resident proteins:

(i) For cell fixation, cells were incubated with 4% paraformaldehyde in DMEM for 10 min and were washed twice with PBS.

(ii) For cell permeabilization, cells were incubated with 0.25% Triton-X in PBS for 8 min. Afterwards, cells were washed three times for 5 min with PBS.

(iii) Cells were incubated in Blocking Buffer (IF) for 1 h and afterwards incubated in the first antibody diluted in Blocking Buffer (IF) for 45 min. Cells were washed three times for 5 min with PBS.

(iv) Cells were incubated with the second antibody in Blocking Buffer (IF) for 45 min. Cells were washed three times for 5 min with PBS.

(v) Coverslips were mounted on glass slides with Prolong Gold Antifade Mountant. Images were acquired using 63x oil immersion objective.

FLIM-FRET

Cos1 cells were seeded in a µ-Slide 8 well (IBIDI) one day before transfection. Cell were transfected with 100 ng FRET-MERLIN biosensors sCal-L1-mVen and mCer-L1-B33C, sCal-L1-mCer and mVen-L1-B33C, mCer-L1-B33C and A2A-mVen, or mCer-L0-mVen.

FLIM-FRET measurements were performed using a Leica TCS SP8 confocal microscope (Leica Microsystems GmBH) equipped with a FLIM unit (PicoQuant GmbH). For excitation (ex) and emission (em) of fluorescent proteins, the following laser settings were used: mCerulean3 at ex458 and em465–505 nm; mVenus at ex514 and em520–560 nm. FLIM data derive from three different biological replicates and measurements of 10 cells each replicate.

Transmission electron microscopy

HCT116 or HCT116 stable MERLIN cells were seeded on µ-Dish$^{35\ mm,\ high}$ (IBIDI) two days before treatment and/or fixation. Cells were treated with Tunicamycin (25 nM) or deprived from FBS (starvation) for 4h. After washing and fixation with 2.5% glutaraldehyde (Sigma-Aldrich) in 20 mM Hepes buffer (pH 7.4) for 2 h at 37°C, the cells were washed with buffer, postfixed in 2% osmium tetroxide, dehydrated, and embedded in epoxide resin (Araldite, Serva) as described previously (Wolburg-Buchholz et al., 2009). Ultrathin sections were

performed using a Reichert Ultracut ultramicrotome (Leica) and were analyzed in an EM 10 electron microscope (Zeiss). Images were taken by a digital camera (Tröndle).

CHAPTER 4.

Conclusions

The conclusions that can be drawn from **CHAPTER 2**:

1. Under apoptotic conditions, BAK assembles into distinct supra-molecular structures including rings, arc-shaped and linear structures. The form of these structures is comparable to those formed by its homolog BAX; however, they are smaller and more uniform in size.

2. Kinetic measurement of BAK assemblies demonstrated that their distribution slightly changes over time during the progression of apoptosis, from more linear structures towards more rings.

3. BAK and BAX co-assemble into foci and contribute to each other's assembly mechanism: Endogenous BAX slightly increases the size of BAK structures.

4. BAK apoptotic pores lead to an earlier release of mtDNA which might influence in the inflammatory potential of an apoptotic cell.

The conclusion that can be drawn from **CHAPTER 3**:

1. We present MERLIN, a powerful novel biosensor to investigate MERCs molecular architecture and their spatiotemporal changes in living cells.

2. MERLIN is sensitive to changes caused by genetic or pharmacological treatments known to influence MERCs.

3. The main advantage of MERLIN, over other currently available tools, is its proximity sensing ability that does not depend on physical interaction, allowing measurements of reversible changes in MERCs and the prevention of enforced interaction between the two organelles.

4. Knockdown of proteins of the mitochondrial dynamics machinery, namely Drp1, Mfn1 and Mfn2, reduces the interaction between mitochondria and the ER, highlighting the importance of the mitochondrial morphology for MERCs.

5. MERLIN is a powerful tool that offers the possibility for multifaceted applications, like high-throughput genetic or drug screenings, in vivo applications in mouse, measurements in sensitive cell types like neurons, and adaption to other contact sites by replacing the targeting sequences and optimizing the linker length.

References

Ader, N. R., Hoffmann, P. C., Ganeva, I., Borgeaud, A. C., Wang, C., Youle, R. J., & Kukulski, W. (2019). Molecular and topological reorganizations in mitochondrial architecture interplay during Bax-mediated steps of apoptosis. *Elife, 8*. doi: 10.7554/eLife.40712

Anderson, S., Bankier, A. T., Barrell, B. G., de Bruijn, M. H., Coulson, A. R., Drouin, J., . . . Young, I. G. (1981). Sequence and organization of the human mitochondrial genome. *Nature, 290*(5806), 457-465. doi: 10.1038/290457a0

Annis, M. G., Soucie, E. L., Dlugosz, P. J., Cruz-Aguado, J. A., Penn, L. Z., Leber, B., & Andrews, D. W. (2005). Bax forms multispanning monomers that oligomerize to permeabilize membranes during apoptosis. *EMBO J, 24*(12), 2096-2103. doi: 10.1038/sj.emboj.7600675

Area-Gomez, E., & Schon, E. A. (2016). Mitochondria-associated ER membranes and Alzheimer disease. *Curr Opin Genet Dev, 38*, 90-96. doi: 10.1016/j.gde.2016.04.006

Azad, A., Fox, J., Leverrier, S., & Storey, A. (2012). Blockade of the BAK hydrophobic groove by inhibitory phosphorylation regulates commitment to apoptosis. *PLoS One, 7*(11), e49601. doi: 10.1371/journal.pone.0049601

Basso, V., Marchesan, E., Peggion, C., Chakraborty, J., von Stockum, S., Giacomello, M., . . . Ziviani, E. (2018). Regulation of ER-mitochondria contacts by Parkin via Mfn2. *Pharmacol Res, 138*, 43-56. doi: 10.1016/j.phrs.2018.09.006

Baughman, J. M., Perocchi, F., Girgis, H. S., Plovanich, M., Belcher-Timme, C. A., Sancak, Y., . . . Mootha, V. K. (2011). Integrative genomics identifies MCU as an essential component of the mitochondrial calcium uniporter. *Nature, 476*(7360), 341-345. doi: 10.1038/nature10234

Bernales, S., McDonald, K. L., & Walter, P. (2006). Autophagy counterbalances endoplasmic reticulum expansion during the unfolded protein response. *PLoS Biol, 4*(12), e423. doi: 10.1371/journal.pbio.0040423

Bleicken, S., Classen, M., Padmavathi, P. V., Ishikawa, T., Zeth, K., Steinhoff, H. J., & Bordignon, E. (2010). Molecular details of Bax activation, oligomerization, and membrane insertion. *J Biol Chem, 285*(9), 6636-6647. doi: 10.1074/jbc.M109.081539

Bleicken, S., Hantusch, A., Das, K. K., Frickey, T., & Garcia-Saez, A. J. (2017). Quantitative interactome of a membrane Bcl-2 network identifies a hierarchy of complexes for apoptosis regulation. *Nat Commun, 8*(1), 73. doi: 10.1038/s41467-017-00086-6

Bleicken, S., Hofhaus, G., Ugarte-Uribe, B., Schröder, R., & García-Sáez, A. J. (2016). cBid, Bax and Bcl-xL exhibit opposite membrane remodeling activities. *Cell Death Dis, 7*(2), e2121. doi: 10.1038/cddis.2016.34

Bleicken, S., Jeschke, G., Stegmueller, C., Salvador-Gallego, R., García-Sáez, A. J., & Bordignon, E. (2014). Structural model of active Bax at the membrane. *Mol Cell, 56*(4), 496-505. doi: 10.1016/j.molcel.2014.09.022

Bleicken, S., Landeta, O., Landajuela, A., Basañez, G., & García-Sáez, A. J. (2013). Proapoptotic Bax and Bak proteins form stable protein-permeable pores of tunable size. *J Biol Chem, 288*(46), 33241-33252. doi: 10.1074/jbc.M113.512087

Bleicken, S., Wagner, C., & García-Sáez, A. J. (2013). Mechanistic differences in the membrane activity of Bax and Bcl-xL correlate with their opposing roles in apoptosis. *Biophys J, 104*(2), 421-431. doi: 10.1016/j.bpj.2012.12.010

Boehning, D., Patterson, R. L., Sedaghat, L., Glebova, N. O., Kurosaki, T., & Snyder, S. H. (2003). Cytochrome c binds to inositol (1,4,5) trisphosphate receptors,

amplifying calcium-dependent apoptosis. *Nat Cell Biol, 5*(12), 1051-1061. doi: 10.1038/ncb1063
Bolender, N., Sickmann, A., Wagner, R., Meisinger, C., & Pfanner, N. (2008). Multiple pathways for sorting mitochondrial precursor proteins. *EMBO Rep, 9*(1), 42-49. doi: 10.1038/sj.embor.7401126
Bonora, M., Giorgi, C., Bononi, A., Marchi, S., Patergnani, S., Rimessi, A., . . . Pinton, P. (2013). Subcellular calcium measurements in mammalian cells using jellyfish photoprotein aequorin-based probes. *Nat Protoc, 8*(11), 2105-2118. doi: 10.1038/nprot.2013.127
Božič, B., & Rozman, B. (2006). Apoptosis and Autoimmunity. *EJIFCC, 17*(3), 69-74.
Bravo, R., Vicencio, J. M., Parra, V., Troncoso, R., Munoz, J. P., Bui, M., . . . Lavandero, S. (2011). Increased ER-mitochondrial coupling promotes mitochondrial respiration and bioenergetics during early phases of ER stress. *J Cell Sci, 124*(Pt 13), 2143-2152. doi: 10.1242/jcs.080762
Braymer, J. J., & Lill, R. (2017). Iron-sulfur cluster biogenesis and trafficking in mitochondria. *J Biol Chem, 292*(31), 12754-12763. doi: 10.1074/jbc.R117.787101
Brokatzky, D., Dörflinger, B., Haimovici, A., Weber, A., Kirschnek, S., Vier, J., . . . Häcker, G. (2019). A non-death function of the mitochondrial apoptosis apparatus in immunity. *The EMBO Journal, 38*(11), e100907. doi: 10.15252/embj.2018100907
Brooks, C., Wei, Q., Feng, L., Dong, G., Tao, Y., Mei, L., . . . Dong, Z. (2007). Bak regulates mitochondrial morphology and pathology during apoptosis by interacting with mitofusins. *Proc Natl Acad Sci U S A, 104*(28), 11649-11654. doi: 10.1073/pnas.0703976104
Brouwer, J. M., Westphal, D., Dewson, G., Robin, A. Y., Uren, R. T., Bartolo, R., . . . Czabotar, P. E. (2014). Bak core and latch domains separate during activation, and freed core domains form symmetric homodimers. *Mol Cell, 55*(6), 938-946. doi: 10.1016/j.molcel.2014.07.016
Brown, J. M., & Attardi, L. D. (2005). The role of apoptosis in cancer development and treatment response. *Nature Reviews Cancer, 5*(3), 231-237. doi: 10.1038/nrc1560
Buendia, B., Santa-Maria, A., & Courvalin, J. C. (1999). Caspase-dependent proteolysis of integral and peripheral proteins of nuclear membranes and nuclear pore complex proteins during apoptosis. *Journal of Cell Science, 112*(11), 1743-1753.
Cárdenas, C., Miller, R. A., Smith, I., Bui, T., Molgó, J., Müller, M., . . . Foskett, J. K. (2010). Essential regulation of cell bioenergetics by constitutive InsP3 receptor Ca2+ transfer to mitochondria. *Cell, 142*(2), 270-283. doi: 10.1016/j.cell.2010.06.007
Cartron, P.-F., Petit, E., Bellot, G., Oliver, L., & Vallette, F. M. (2014). Metaxins 1 and 2, two proteins of the mitochondrial protein sorting and assembly machinery, are essential for Bak activation during TNF alpha triggered apoptosis. *Cellular Signalling, 26*(9), 1928-1934. doi: https://doi.org/10.1016/j.cellsig.2014.04.021
Cerqua, C., Anesti, V., Pyakurel, A., Liu, D., Naon, D., Wiche, G., . . . Scorrano, L. (2010). Trichoplein/mitostatin regulates endoplasmic reticulum-mitochondria juxtaposition. *EMBO Rep, 11*(11), 854-860. doi: 10.1038/embor.2010.151
Chen, H. C., Kanai, M., Inoue-Yamauchi, A., Tu, H. C., Huang, Y., Ren, D., . . . Cheng, E. H. (2015). An interconnected hierarchical model of cell death regulation by the BCL-2 family. *Nat Cell Biol, 17*(10), 1270-1281. doi: 10.1038/ncb3236
Chen, L., Willis, S. N., Wei, A., Smith, B. J., Fletcher, J. I., Hinds, M. G., . . . Huang, D. C. (2005). Differential targeting of prosurvival Bcl-2 proteins by their BH3-only ligands allows complementary apoptotic function. *Mol Cell, 17*(3), 393-403. doi: 10.1016/j.molcel.2004.12.030
Cheng, E. H.-Y., Sheiko, T. V., Fisher, J. K., Craigen, W. J., & Korsmeyer, S. J. (2003). VDAC2 Inhibits BAK Activation and Mitochondrial Apoptosis. *Science, 301*(5632), 513-517. doi: 10.1126/science.1083995

Cheng, E. H., Wei, M. C., Weiler, S., Flavell, R. A., Mak, T. W., Lindsten, T., & Korsmeyer, S. J. (2001). BCL-2, BCL-X(L) sequester BH3 domain-only molecules preventing BAX- and BAK-mediated mitochondrial apoptosis. *Mol Cell, 8*(3), 705-711. doi: 10.1016/s1097-2765(01)00320-3

Chin, H. S., Li, M. X., Tan, I. K. L., Ninnis, R. L., Reljic, B., Scicluna, K., . . . Dewson, G. (2018). VDAC2 enables BAX to mediate apoptosis and limit tumor development. *Nature Communications, 9*(1), 4976. doi: 10.1038/s41467-018-07309-4

Chipuk, J. E., Moldoveanu, T., Llambi, F., Parsons, M. J., & Green, D. R. (2010). The BCL-2 Family Reunion. *Molecular Cell, 37*(3), 299-310. doi: https://doi.org/10.1016/j.molcel.2010.01.025

Chittenden, T., Harrington, E. A., O'Connor, R., Flemington, C., Lutz, R. J., Evan, G. I., & Guild, B. C. (1995). Induction of apoptosis by the Bcl-2 homologue Bak. *Nature, 374*(6524), 733-736. doi: 10.1038/374733a0

Cieri, D., Vicario, M., Giacomello, M., Vallese, F., Filadi, R., Wagner, T., . . . Calì, T. (2018). SPLICS: a split green fluorescent protein-based contact site sensor for narrow and wide heterotypic organelle juxtaposition. *Cell Death Differ, 25*(6), 1131-1145. doi: 10.1038/s41418-017-0033-z

Cipolat, S., Martins de Brito, O., Dal Zilio, B., & Scorrano, L. (2004). OPA1 requires mitofusin 1 to promote mitochondrial fusion. *Proc Natl Acad Sci U S A, 101*(45), 15927-15932. doi: 10.1073/pnas.0407043101

Cleland, M. M., Norris, K. L., Karbowski, M., Wang, C., Suen, D. F., Jiao, S., . . . Youle, R. J. (2011). Bcl-2 family interaction with the mitochondrial morphogenesis machinery. *Cell Death Differ, 18*(2), 235-247. doi: 10.1038/cdd.2010.89

Cohen, M. M., & Tareste, D. (2018). Recent insights into the structure and function of Mitofusins in mitochondrial fusion. *F1000Research, 7*, F1000 Faculty Rev-1983. doi: 10.12688/f1000research.16629.1

Collado, J., & Fernández-Busnadiego, R. (2017). Deciphering the molecular architecture of membrane contact sites by cryo-electron tomography. *Biochim Biophys Acta Mol Cell Res, 1864*(9), 1507-1512. doi: 10.1016/j.bbamcr.2017.03.009

Comte, J., Maïsterrena, B., & Gautheron, D. C. (1976). Lipid composition and protein profiles of outer and inner membranes from pig heart mitochondria. Comparison with microsomes. *Biochim Biophys Acta, 419*(2), 271-284. doi: 10.1016/0005-2736(76)90353-9

Cosentino, K., & García-Sáez, A. J. (2014). Mitochondrial alterations in apoptosis. *Chem Phys Lipids, 181*, 62-75. doi: 10.1016/j.chemphyslip.2014.04.001

Cosson, P., Marchetti, A., Ravazzola, M., & Orci, L. (2012). Mitofusin-2 independent juxtaposition of endoplasmic reticulum and mitochondria: an ultrastructural study. *PLoS One, 7*(9), e46293. doi: 10.1371/journal.pone.0046293

Crompton, M. (1999). The mitochondrial permeability transition pore and its role in cell death. *Biochem J, 341 (Pt 2)*(Pt 2), 233-249.

Csordás, G., Renken, C., Várnai, P., Walter, L., Weaver, D., Buttle, K. F., . . . Hajnóczky, G. (2006). Structural and functional features and significance of the physical linkage between ER and mitochondria. *J Cell Biol, 174*(7), 915-921. doi: 10.1083/jcb.200604016

Csordás, G., Várnai, P., Golenár, T., Roy, S., Purkins, G., Schneider, T. G., . . . Hajnóczky, G. (2010). Imaging interorganelle contacts and local calcium dynamics at the ER-mitochondrial interface. *Mol Cell, 39*(1), 121-132. doi: 10.1016/j.molcel.2010.06.029

Cui, Z., Vance, J. E., Chen, M. H., Voelker, D. R., & Vance, D. E. (1993). Cloning and expression of a novel phosphatidylethanolamine N-methyltransferase. A specific biochemical and cytological marker for a unique membrane fraction in rat liver. *J Biol Chem, 268*(22), 16655-16663.

Czabotar, P. E., Westphal, D., Dewson, G., Ma, S., Hockings, C., Fairlie, W. D., . . . Colman, P. M. (2013). Bax crystal structures reveal how BH3 domains activate

Bax and nucleate its oligomerization to induce apoptosis. *Cell, 152*(3), 519-531. doi: 10.1016/j.cell.2012.12.031
Dai, H., Smith, A., Meng, X. W., Schneider, P. A., Pang, Y. P., & Kaufmann, S. H. (2011). Transient binding of an activator BH3 domain to the Bak BH3-binding groove initiates Bak oligomerization. *J Cell Biol, 194*(1), 39-48. doi: 10.1083/jcb.201102027
de Brito, O. M., & Scorrano, L. (2008). Mitofusin 2 tethers endoplasmic reticulum to mitochondria. *Nature, 456*(7222), 605-610. doi: 10.1038/nature07534
Denton, R. M. (2009). Regulation of mitochondrial dehydrogenases by calcium ions. *Biochim Biophys Acta, 1787*(11), 1309-1316. doi: 10.1016/j.bbabio.2009.01.005
Desagher, S., & Martinou, J. C. (2000). Mitochondria as the central control point of apoptosis. *Trends Cell Biol, 10*(9), 369-377. doi: 10.1016/s0962-8924(00)01803-1
Desagher, S., Osen-Sand, A., Nichols, A., Eskes, R., Montessuit, S., Lauper, S., . . . Martinou, J. C. (1999). Bid-induced conformational change of Bax is responsible for mitochondrial cytochrome c release during apoptosis. *J Cell Biol, 144*(5), 891-901. doi: 10.1083/jcb.144.5.891
Dewson, G., Kratina, T., Czabotar, P., Day, C. L., Adams, J. M., & Kluck, R. M. (2009). Bak activation for apoptosis involves oligomerization of dimers via their alpha6 helices. *Mol Cell, 36*(4), 696-703. doi: 10.1016/j.molcel.2009.11.008
Dewson, G., Kratina, T., Sim, H. W., Puthalakath, H., Adams, J. M., Colman, P. M., & Kluck, R. M. (2008). To trigger apoptosis, Bak exposes its BH3 domain and homodimerizes via BH3:groove interactions. *Mol Cell, 30*(3), 369-380. doi: 10.1016/j.molcel.2008.04.005
Dewson, G., Ma, S., Frederick, P., Hockings, C., Tan, I., Kratina, T., & Kluck, R. M. (2012). Bax dimerizes via a symmetric BH3:groove interface during apoptosis. *Cell Death Differ, 19*(4), 661-670. doi: 10.1038/cdd.2011.138
Du, C., Fang, M., Li, Y., Li, L., & Wang, X. (2000). Smac, a mitochondrial protein that promotes cytochrome c-dependent caspase activation by eliminating IAP inhibition. *Cell, 102*(1), 33-42. doi: 10.1016/s0092-8674(00)00008-8
Du, Y., Ferro-Novick, S., & Novick, P. (2004). Dynamics and inheritance of the endoplasmic reticulum. *J Cell Sci, 117*(Pt 14), 2871-2878. doi: 10.1242/jcs.01286
Dunn, K. W., Kamocka, M. M., & McDonald, J. H. (2011). A practical guide to evaluating colocalization in biological microscopy. *Am J Physiol Cell Physiol, 300*(4), C723-742. doi: 10.1152/ajpcell.00462.2010
Edlich, F., Banerjee, S., Suzuki, M., Cleland, M. M., Arnoult, D., Wang, C., . . . Youle, R. J. (2011). Bcl-x(L) retrotranslocates Bax from the mitochondria into the cytosol. *Cell, 145*(1), 104-116. doi: 10.1016/j.cell.2011.02.034
Elmore, S. (2007). Apoptosis: A Review of Programmed Cell Death. *Toxicologic Pathology, 35*(4), 495-516. doi: 10.1080/01926230701320337
Enari, M., Sakahira, H., Yokoyama, H., Okawa, K., Iwamatsu, A., & Nagata, S. (1998). A caspase-activated DNase that degrades DNA during apoptosis, and its inhibitor ICAD. *Nature, 391*(6662), 43-50. doi: 10.1038/34112
Eura, Y., Ishihara, N., Yokota, S., & Mihara, K. (2003). Two mitofusin proteins, mammalian homologues of FZO, with distinct functions are both required for mitochondrial fusion. *J Biochem, 134*(3), 333-344. doi: 10.1093/jb/mvg150
Fagone, P., & Jackowski, S. (2009). Membrane phospholipid synthesis and endoplasmic reticulum function. *J Lipid Res, 50 Suppl*(Suppl), S311-316. doi: 10.1194/jlr.R800049-JLR200
Filadi, R., Greotti, E., Turacchio, G., Luini, A., Pozzan, T., & Pizzo, P. (2015). Mitofusin 2 ablation increases endoplasmic reticulum-mitochondria coupling. *Proc Natl Acad Sci U S A, 112*(17), E2174-2181. doi: 10.1073/pnas.1504880112
Fox, J. L., Ismail, F., Azad, A., Ternette, N., Leverrier, S., Edelmann, M. J., . . . Storey, A. (2010). Tyrosine dephosphorylation is required for Bak activation in apoptosis. *EMBO J, 29*(22), 3853-3868. doi: 10.1038/emboj.2010.244

Frank, S., Gaume, B., Bergmann-Leitner, E. S., Leitner, W. W., Robert, E. G., Catez, F., . . . Youle, R. J. (2001). The role of dynamin-related protein 1, a mediator of mitochondrial fission, in apoptosis. *Dev Cell, 1*(4), 515-525. doi: 10.1016/s1534-5807(01)00055-7

Fredriksson, S., Gullberg, M., Jarvius, J., Olsson, C., Pietras, K., Gústafsdóttir, S. M., . . . Landegren, U. (2002). Protein detection using proximity-dependent DNA ligation assays. *Nat Biotechnol, 20*(5), 473-477. doi: 10.1038/nbt0502-473

Friedman, J. R., Lackner, L. L., West, M., DiBenedetto, J. R., Nunnari, J., & Voeltz, G. K. (2011). ER tubules mark sites of mitochondrial division. *Science, 334*(6054), 358-362. doi: 10.1126/science.1207385

García-Sáez, A. J. (2012). The secrets of the Bcl-2 family. *Cell Death Differ, 19*(11), 1733-1740. doi: 10.1038/cdd.2012.105

Gavathiotis, E., Suzuki, M., Davis, M. L., Pitter, K., Bird, G. H., Katz, S. G., . . . Walensky, L. D. (2008). BAX activation is initiated at a novel interaction site. *Nature, 455*(7216), 1076-1081. doi: 10.1038/nature07396

Gillies, L. A., Du, H., Peters, B., Knudson, C. M., Newmeyer, D. D., & Kuwana, T. (2015). Visual and functional demonstration of growing Bax-induced pores in mitochondrial outer membranes. *Mol Biol Cell, 26*(2), 339-349. doi: 10.1091/mbc.E13-11-0638

Giorgi, C., Ito, K., Lin, H. K., Santangelo, C., Wieckowski, M. R., Lebiedzinska, M., . . . Pandolfi, P. P. (2010). PML regulates apoptosis at endoplasmic reticulum by modulating calcium release. *Science, 330*(6008), 1247-1251. doi: 10.1126/science.1189157

Goldstein, J. C., Waterhouse, N. J., Juin, P., Evan, G. I., & Green, D. R. (2000). The coordinate release of cytochrome c during apoptosis is rapid, complete and kinetically invariant. *Nat Cell Biol, 2*(3), 156-162. doi: 10.1038/35004029

Grimm, S. (2012). The ER-mitochondria interface: the social network of cell death. *Biochim Biophys Acta, 1823*(2), 327-334. doi: 10.1016/j.bbamcr.2011.11.018

Große, L., Wurm, C. A., Brüser, C., Neumann, D., Jans, D. C., & Jakobs, S. (2016). Bax assembles into large ring-like structures remodeling the mitochondrial outer membrane in apoptosis. *EMBO J, 35*(4), 402-413. doi: 10.15252/embj.201592789

Hamasaki, M., Furuta, N., Matsuda, A., Nezu, A., Yamamoto, A., Fujita, N., . . . Yoshimori, T. (2013). Autophagosomes form at ER-mitochondria contact sites. *Nature, 495*(7441), 389-393. doi: 10.1038/nature11910

Harmon, M., Larkman, P., Hardingham, G., Jackson, M., & Skehel, P. (2017). A Bi-fluorescence complementation system to detect associations between the Endoplasmic reticulum and mitochondria. *Sci Rep, 7*(1), 17467. doi: 10.1038/s41598-017-17278-1

Hayashi, T., & Su, T. P. (2007). Sigma-1 receptor chaperones at the ER-mitochondrion interface regulate Ca(2+) signaling and cell survival. *Cell, 131*(3), 596-610. doi: 10.1016/j.cell.2007.08.036

Hermann, E., Bleicken, S., Subburaj, Y., & García-Sáez, A. J. (2014). Automated analysis of giant unilamellar vesicles using circular Hough transformation. *Bioinformatics, 30*(12), 1747-1754. doi: 10.1093/bioinformatics/btu102

Hertlein, V., Flores-Romero, H., Das, K. K., Fischer, S., Heunemann, M., Calleja-Felipe, M., . . . García-Sáez, A. J. (2020). MERLIN: a novel BRET-based proximity biosensor for studying mitochondria–ER contact sites. *Life Science Alliance, 3*(1), e201900600. doi: 10.26508/lsa.201900600

Hirabayashi, Y., Kwon, S. K., Paek, H., Pernice, W. M., Paul, M. A., Lee, J., . . . Polleux, F. (2017). ER-mitochondria tethering by PDZD8 regulates Ca(2+) dynamics in mammalian neurons. *Science, 358*(6363), 623-630. doi: 10.1126/science.aan6009

Hirota, J., Furuichi, T., & Mikoshiba, K. (1999). Inositol 1,4,5-trisphosphate receptor type 1 is a substrate for caspase-3 and is cleaved during apoptosis in a caspase-3-

dependent manner. *J Biol Chem, 274*(48), 34433-34437. doi: 10.1074/jbc.274.48.34433

Hockings, C., Alsop, A. E., Fennell, S. C., Lee, E. F., Fairlie, W. D., Dewson, G., & Kluck, R. M. (2018). Mcl-1 and Bcl-x(L) sequestration of Bak confers differential resistance to BH3-only proteins. *Cell Death Differ, 25*(4), 721-734. doi: 10.1038/s41418-017-0010-6

Hoppins, S., Edlich, F., Cleland, M. M., Banerjee, S., McCaffery, J. M., Youle, R. J., & Nunnari, J. (2011). The soluble form of Bax regulates mitochondrial fusion via MFN2 homotypic complexes. *Mol Cell, 41*(2), 150-160. doi: 10.1016/j.molcel.2010.11.030

Hoppins, S., Lackner, L., & Nunnari, J. (2007). The machines that divide and fuse mitochondria. *Annu Rev Biochem, 76*, 751-780. doi: 10.1146/annurev.biochem.76.071905.090048

Hu, J., Prinz, W. A., & Rapoport, T. A. (2011). Weaving the web of ER tubules. *Cell, 147*(6), 1226-1231. doi: 10.1016/j.cell.2011.11.022

Huang, X., Jiang, C., Yu, L., & Yang, A. (2020). Current and Emerging Approaches for Studying Inter-Organelle Membrane Contact Sites. *Front Cell Dev Biol, 8*, 195. doi: 10.3389/fcell.2020.00195

Hung, V., Lam, S. S., Udeshi, N. D., Svinkina, T., Guzman, G., Mootha, V. K., . . . Ting, A. Y. (2017). Proteomic mapping of cytosol-facing outer mitochondrial and ER membranes in living human cells by proximity biotinylation. *Elife, 6*. doi: 10.7554/eLife.24463

Hurst, S., Hoek, J., & Sheu, S. S. (2017). Mitochondrial Ca(2+) and regulation of the permeability transition pore. *J Bioenerg Biomembr, 49*(1), 27-47. doi: 10.1007/s10863-016-9672-x

Ichim, G., & Tait, S. W. (2016). A fate worse than death: apoptosis as an oncogenic process. *Nat Rev Cancer, 16*(8), 539-548. doi: 10.1038/nrc.2016.58

Iyer, S., Uren, R. T., Dengler, M. A., Shi, M. X., Uno, E., Adams, J. M., . . . Kluck, R. M. (2020). Robust autoactivation for apoptosis by BAK but not BAX highlights BAK as an important therapeutic target. *Cell Death Dis, 11*(4), 268. doi: 10.1038/s41419-020-2463-7

Jan, C. H., Williams, C. C., & Weissman, J. S. (2014). Principles of ER cotranslational translocation revealed by proximity-specific ribosome profiling. *Science, 346*(6210), 1257521. doi: 10.1126/science.1257521

Jin, Z., & El-Deiry, W. S. (2005). Overview of cell death signaling pathways. *Cancer Biology & Therapy, 4*(2), 147-171. doi: 10.4161/cbt.4.2.1508

Kamerkar, S. C., Kraus, F., Sharpe, A. J., Pucadyil, T. J., & Ryan, M. T. (2018). Dynamin-related protein 1 has membrane constricting and severing abilities sufficient for mitochondrial and peroxisomal fission. *Nature Communications, 9*(1), 5239. doi: 10.1038/s41467-018-07543-w

Karbowski, M., Lee, Y. J., Gaume, B., Jeong, S. Y., Frank, S., Nechushtan, A., . . . Youle, R. J. (2002). Spatial and temporal association of Bax with mitochondrial fission sites, Drp1, and Mfn2 during apoptosis. *J Cell Biol, 159*(6), 931-938. doi: 10.1083/jcb.200209124

Kawano, S., Tamura, Y., Kojima, R., Bala, S., Asai, E., Michel, A. H., . . . Endo, T. (2018). Structure-function insights into direct lipid transfer between membranes by Mmm1-Mdm12 of ERMES. *J Cell Biol, 217*(3), 959-974. doi: 10.1083/jcb.201704119

Kerkhofs, M., Giorgi, C., Marchi, S., Seitaj, B., Parys, J. B., Pinton, P., . . . Bittremieux, M. (2017). Alterations in Ca(2+) Signalling via ER-Mitochondria Contact Site Remodelling in Cancer. *Adv Exp Med Biol, 997*, 225-254. doi: 10.1007/978-981-10-4567-7_17

Kerr, J. F. R., Wyllie, A. H., & Currie, A. R. (1972). Apoptosis: A Basic Biological Phenomenon with Wideranging Implications in Tissue Kinetics. *British Journal of Cancer, 26*(4), 239-257. doi: 10.1038/bjc.1972.33

Kim, H., Tu, H. C., Ren, D., Takeuchi, O., Jeffers, J. R., Zambetti, G. P., . . . Cheng, E. H. (2009). Stepwise activation of BAX and BAK by tBID, BIM, and PUMA initiates mitochondrial apoptosis. *Mol Cell, 36*(3), 487-499. doi: 10.1016/j.molcel.2009.09.030

Kirichok, Y., Krapivinsky, G., & Clapham, D. E. (2004). The mitochondrial calcium uniporter is a highly selective ion channel. *Nature, 427*(6972), 360-364. doi: 10.1038/nature02246

Kolossov, V. L., Spring, B. Q., Sokolowski, A., Conour, J. E., Clegg, R. M., Kenis, P. J., & Gaskins, H. R. (2008). Engineering redox-sensitive linkers for genetically encoded FRET-based biosensors. *Exp Biol Med (Maywood), 233*(2), 238-248. doi: 10.3181/0707-rm-192

Kornmann, B., Currie, E., Collins, S. R., Schuldiner, M., Nunnari, J., Weissman, J. S., & Walter, P. (2009). An ER-mitochondria tethering complex revealed by a synthetic biology screen. *Science, 325*(5939), 477-481. doi: 10.1126/science.1175088

Kornmann, B., & Walter, P. (2010). ERMES-mediated ER-mitochondria contacts: molecular hubs for the regulation of mitochondrial biology. *J Cell Sci, 123*(Pt 9), 1389-1393. doi: 10.1242/jcs.058636

Korobova, F., Ramabhadran, V., & Higgs, H. N. (2013). An actin-dependent step in mitochondrial fission mediated by the ER-associated formin INF2. *Science, 339*(6118), 464-467. doi: 10.1126/science.1228360

Kothakota, S., Azuma, T., Reinhard, C., Klippel, A., Tang, J., Chu, K., . . . Williams, L. T. (1997). Caspase-3-Generated Fragment of Gelsolin: Effector of Morphological Change in Apoptosis. *Science, 278*(5336), 294-298. doi: 10.1126/science.278.5336.294

Kuwana, T., Bouchier-Hayes, L., Chipuk, J. E., Bonzon, C., Sullivan, B. A., Green, D. R., & Newmeyer, D. D. (2005). BH3 domains of BH3-only proteins differentially regulate Bax-mediated mitochondrial membrane permeabilization both directly and indirectly. *Mol Cell, 17*(4), 525-535. doi: 10.1016/j.molcel.2005.02.003

Kuwana, T., Mackey, M. R., Perkins, G., Ellisman, M. H., Latterich, M., Schneiter, R., . . . Newmeyer, D. D. (2002). Bid, Bax, and lipids cooperate to form supramolecular openings in the outer mitochondrial membrane. *Cell, 111*(3), 331-342. doi: 10.1016/s0092-8674(02)01036-x

Lauterwasser, J., Todt, F., Zerbes, R. M., Nguyen, T. N., Craigen, W., Lazarou, M., . . . Edlich, F. (2016). The porin VDAC2 is the mitochondrial platform for Bax retrotranslocation. *Scientific Reports, 6*(1), 32994. doi: 10.1038/srep32994

Leal, N. S., Schreiner, B., Pinho, C. M., Filadi, R., Wiehager, B., Karlström, H., . . . Ankarcrona, M. (2016). Mitofusin-2 knockdown increases ER-mitochondria contact and decreases amyloid β-peptide production. *J Cell Mol Med, 20*(9), 1686-1695. doi: 10.1111/jcmm.12863

Leber, B., Lin, J., & Andrews, D. W. (2007). Embedded together: the life and death consequences of interaction of the Bcl-2 family with membranes. *Apoptosis, 12*(5), 897-911. doi: 10.1007/s10495-007-0746-4

Leber, B., Lin, J., & Andrews, D. W. (2010). Still embedded together binding to membranes regulates Bcl-2 protein interactions. *Oncogene, 29*(38), 5221-5230. doi: 10.1038/onc.2010.283

Leshchiner, E. S., Braun, C. R., Bird, G. H., & Walensky, L. D. (2013). Direct activation of full-length proapoptotic BAK. *Proc Natl Acad Sci U S A, 110*(11), E986-995. doi: 10.1073/pnas.1214313110

Letai, A., Bassik, M. C., Walensky, L. D., Sorcinelli, M. D., Weiler, S., & Korsmeyer, S. J. (2002). Distinct BH3 domains either sensitize or activate mitochondrial apoptosis, serving as prototype cancer therapeutics. *Cancer Cell, 2*(3), 183-192. doi: 10.1016/s1535-6108(02)00127-7

Lewin, T. M., Kim, J. H., Granger, D. A., Vance, J. E., & Coleman, R. A. (2001). Acyl-CoA synthetase isoforms 1, 4, and 5 are present in different subcellular

membranes in rat liver and can be inhibited independently. *J Biol Chem, 276*(27), 24674-24679. doi: 10.1074/jbc.M102036200
Lewis, A., Hayashi, T., Su, T. P., & Betenbaugh, M. J. (2014). Bcl-2 family in inter-organelle modulation of calcium signaling; roles in bioenergetics and cell survival. *J Bioenerg Biomembr, 46*(1), 1-15. doi: 10.1007/s10863-013-9527-7
Li, H., Zhu, H., Xu, C.-j., & Yuan, J. (1998). Cleavage of BID by Caspase 8 Mediates the Mitochondrial Damage in the Fas Pathway of Apoptosis. *Cell, 94*(4), 491-501. doi: https://doi.org/10.1016/S0092-8674(00)81590-1
Li, P., Nijhawan, D., Budihardjo, I., Srinivasula, S. M., Ahmad, M., Alnemri, E. S., & Wang, X. (1997). Cytochrome c and dATP-Dependent Formation of Apaf-1/Caspase-9 Complex Initiates an Apoptotic Protease Cascade. *Cell, 91*(4), 479-489. doi: 10.1016/S0092-8674(00)80434-1
Lindsten, T., Ross, A. J., King, A., Zong, W. X., Rathmell, J. C., Shiels, H. A., . . . Thompson, C. B. (2000). The combined functions of proapoptotic Bcl-2 family members bak and bax are essential for normal development of multiple tissues. *Mol Cell, 6*(6), 1389-1399. doi: 10.1016/s1097-2765(00)00136-2
Lißе, D., Monzel, C., Vicario, C., Manzi, J., Maurin, I., Coppey, M., . . . Dahan, M. (2017). Engineered Ferritin for Magnetogenetic Manipulation of Proteins and Organelles Inside Living Cells. *Adv Mater, 29*(42). doi: 10.1002/adma.201700189
Llambi, F., Moldoveanu, T., Tait, S. W., Bouchier-Hayes, L., Temirov, J., McCormick, L. L., . . . Green, D. R. (2011). A unified model of mammalian BCL-2 protein family interactions at the mitochondria. *Mol Cell, 44*(4), 517-531. doi: 10.1016/j.molcel.2011.10.001
Lovell, J. F., Billen, L. P., Bindner, S., Shamas-Din, A., Fradin, C., Leber, B., & Andrews, D. W. (2008). Membrane binding by tBid initiates an ordered series of events culminating in membrane permeabilization by Bax. *Cell, 135*(6), 1074-1084. doi: 10.1016/j.cell.2008.11.010
Ma, S. B., Nguyen, T. N., Tan, I., Ninnis, R., Iyer, S., Stroud, D. A., . . . Dewson, G. (2014). Bax targets mitochondria by distinct mechanisms before or during apoptotic cell death: a requirement for VDAC2 or Bak for efficient Bax apoptotic function. *Cell Death & Differentiation, 21*(12), 1925-1935. doi: 10.1038/cdd.2014.119
Mandal, T., Shin, S., Aluvila, S., Chen, H. C., Grieve, C., Choe, J. Y., . . . Oh, K. J. (2016). Assembly of Bak homodimers into higher order homooligomers in the mitochondrial apoptotic pore. *Sci Rep, 6*, 30763. doi: 10.1038/srep30763
Mannella, C. A. (2006). Structure and dynamics of the mitochondrial inner membrane cristae. *Biochim Biophys Acta, 1763*(5-6), 542-548. doi: 10.1016/j.bbamcr.2006.04.006
Mannella, C. A., Buttle, K., Rath, B. K., & Marko, M. (1998). Electron microscopic tomography of rat-liver mitochondria and their interaction with the endoplasmic reticulum. *Biofactors, 8*(3-4), 225-228. doi: 10.1002/biof.5520080309
Manor, U., Bartholomew, S., Golani, G., Christenson, E., Kozlov, M., Higgs, H., . . . Lippincott-Schwartz, J. (2015). A mitochondria-anchored isoform of the actin-nucleating spire protein regulates mitochondrial division. *Elife, 4*. doi: 10.7554/eLife.08828
Marchi, S., Bonora, M., Patergnani, S., Giorgi, C., & Pinton, P. (2017). Methods to Assess Mitochondrial Morphology in Mammalian Cells Mounting Autophagic or Mitophagic Responses. *Methods Enzymol, 588*, 171-186. doi: 10.1016/bs.mie.2016.09.080
Marqusee, S., & Baldwin, R. L. (1987). Helix stabilization by Glu-...Lys+ salt bridges in short peptides of de novo design. *Proc Natl Acad Sci U S A, 84*(24), 8898-8902. doi: 10.1073/pnas.84.24.8898
McArthur, K., Whitehead, L. W., Heddleston, J. M., Li, L., Padman, B. S., Oorschot, V., . . . Kile, B. T. (2018). BAK/BAX macropores facilitate mitochondrial herniation and

mtDNA efflux during apoptosis. *Science, 359*(6378). doi: 10.1126/science.aao6047
McCormack, J. G., Halestrap, A. P., & Denton, R. M. (1990). Role of calcium ions in regulation of mammalian intramitochondrial metabolism. *Physiol Rev, 70*(2), 391-425. doi: 10.1152/physrev.1990.70.2.391
Moldoveanu, T., Follis, A. V., Kriwacki, R. W., & Green, D. R. (2014). Many players in BCL-2 family affairs. *Trends Biochem Sci, 39*(3), 101-111. doi: 10.1016/j.tibs.2013.12.006
Moldoveanu, T., Grace, C. R., Llambi, F., Nourse, A., Fitzgerald, P., Gehring, K., . . . Green, D. R. (2013). BID-induced structural changes in BAK promote apoptosis. *Nat Struct Mol Biol, 20*(5), 589-597. doi: 10.1038/nsmb.2563
Moldoveanu, T., Liu, Q., Tocilj, A., Watson, M., Shore, G., & Gehring, K. (2006). The X-ray structure of a BAK homodimer reveals an inhibitory zinc binding site. *Mol Cell, 24*(5), 677-688. doi: 10.1016/j.molcel.2006.10.014
Montessuit, S., Somasekharan, S. P., Terrones, O., Lucken-Ardjomande, S., Herzig, S., Schwarzenbacher, R., . . . Martinou, J. C. (2010). Membrane remodeling induced by the dynamin-related protein Drp1 stimulates Bax oligomerization. *Cell, 142*(6), 889-901. doi: 10.1016/j.cell.2010.08.017
Morciano, G., Marchi, S., Morganti, C., Sbano, L., Bittremieux, M., Kerkhofs, M., . . . Pinton, P. (2018). Role of Mitochondria-Associated ER Membranes in Calcium Regulation in Cancer-Specific Settings. *Neoplasia, 20*(5), 510-523. doi: 10.1016/j.neo.2018.03.005
Moreau, C., Cartron, P. F., Hunt, A., Meflah, K., Green, D. R., Evan, G., . . . Juin, P. (2003). Minimal BH3 peptides promote cell death by antagonizing anti-apoptotic proteins. *J Biol Chem, 278*(21), 19426-19435. doi: 10.1074/jbc.M209472200
Muñoz, J. P., Ivanova, S., Sánchez-Wandelmer, J., Martínez-Cristóbal, P., Noguera, E., Sancho, A., . . . Zorzano, A. (2013). Mfn2 modulates the UPR and mitochondrial function via repression of PERK. *EMBO J, 32*(17), 2348-2361. doi: 10.1038/emboj.2013.168
Murphy, A. N., Bredesen, D. E., Cortopassi, G., Wang, E., & Fiskum, G. (1996). Bcl-2 potentiates the maximal calcium uptake capacity of neural cell mitochondria. *Proc Natl Acad Sci U S A, 93*(18), 9893-9898. doi: 10.1073/pnas.93.18.9893
Naon, D., Zaninello, M., Giacomello, M., Varanita, T., Grespi, F., Lakshminaranayan, S., . . . Scorrano, L. (2016). Critical reappraisal confirms that Mitofusin 2 is an endoplasmic reticulum-mitochondria tether. *Proc Natl Acad Sci U S A, 113*(40), 11249-11254. doi: 10.1073/pnas.1606786113
Nutt, L. K., Pataer, A., Pahler, J., Fang, B., Roth, J., McConkey, D. J., & Swisher, S. G. (2002). Bax and Bak promote apoptosis by modulating endoplasmic reticular and mitochondrial Ca2+ stores. *J Biol Chem, 277*(11), 9219-9225. doi: 10.1074/jbc.M106817200
Oakes, S. A., Scorrano, L., Opferman, J. T., Bassik, M. C., Nishino, M., Pozzan, T., & Korsmeyer, S. J. (2005). Proapoptotic BAX and BAK regulate the type 1 inositol trisphosphate receptor and calcium leak from the endoplasmic reticulum. *Proc Natl Acad Sci U S A, 102*(1), 105-110. doi: 10.1073/pnas.0408352102
Obonai, T., Mizuguchi, M., & Takashima, S. (1998). Developmental and aging changes of Bak expression in the human brain. *Brain Res, 783*(1), 167-170. doi: 10.1016/s0006-8993(97)01361-9
Obulesu, M., & Lakshmi, M. J. (2014). Apoptosis in Alzheimer's disease: an understanding of the physiology, pathology and therapeutic avenues. *Neurochem Res, 39*(12), 2301-2312. doi: 10.1007/s11064-014-1454-4
Oettinghaus, B., D'Alonzo, D., Barbieri, E., Restelli, L. M., Savoia, C., Licci, M., . . . Scorrano, L. (2016). DRP1-dependent apoptotic mitochondrial fission occurs independently of BAX, BAK and APAF1 to amplify cell death by BID and oxidative stress. *Biochim Biophys Acta, 1857*(8), 1267-1276. doi: 10.1016/j.bbabio.2016.03.016

Oltvai, Z. N., Milliman, C. L., & Korsmeyer, S. J. (1993). Bcl-2 heterodimerizes in vivo with a conserved homolog, Bax, that accelerates programmed cell death. *Cell, 74*(4), 609-619. doi: 10.1016/0092-8674(93)90509-o

Opferman, J. T., & Kothari, A. (2018). Anti-apoptotic BCL-2 family members in development. *Cell Death Differ, 25*(1), 37-45. doi: 10.1038/cdd.2017.170

Osellame, L. D., Singh, A. P., Stroud, D. A., Palmer, C. S., Stojanovski, D., Ramachandran, R., & Ryan, M. T. (2016). Cooperative and independent roles of the Drp1 adaptors Mff, MiD49 and MiD51 in mitochondrial fission. *Journal of Cell Science, 129*(11), 2170-2181. doi: 10.1242/jcs.185165

Otera, H., Miyata, N., Kuge, O., & Mihara, K. (2016). Drp1-dependent mitochondrial fission via MiD49/51 is essential for apoptotic cristae remodeling. *J Cell Biol, 212*(5), 531-544. doi: 10.1083/jcb.201508099

Paillusson, S., Stoica, R., Gomez-Suaga, P., Lau, D. H. W., Mueller, S., Miller, T., & Miller, C. C. J. (2016). There's Something Wrong with my MAM; the ER-Mitochondria Axis and Neurodegenerative Diseases. *Trends Neurosci, 39*(3), 146-157. doi: 10.1016/j.tins.2016.01.008

Pedelacq, J. D., & Cabantous, S. (2019). Development and Applications of Superfolder and Split Fluorescent Protein Detection Systems in Biology. *Int J Mol Sci, 20*(14). doi: 10.3390/ijms20143479

Peña-Blanco, A., & García-Sáez, A. J. (2018). Bax, Bak and beyond — mitochondrial performance in apoptosis. *The FEBS Journal, 285*(3), 416-431. doi: https://doi.org/10.1111/febs.14186

Perkins, G. A., & Frey, T. G. (2000). Recent structural insight into mitochondria gained by microscopy. *Micron, 31*(1), 97-111. doi: 10.1016/s0968-4328(99)00065-7

Perkins, G. A., Tjong, J., Brown, J. M., Poquiz, P. H., Scott, R. T., Kolson, D. R., . . . Spirou, G. A. (2010). The micro-architecture of mitochondria at active zones: electron tomography reveals novel anchoring scaffolds and cristae structured for high-rate metabolism. *J Neurosci, 30*(3), 1015-1026. doi: 10.1523/jneurosci.1517-09.2010

Pernas, L., & Scorrano, L. (2016). Mito-Morphosis: Mitochondrial Fusion, Fission, and Cristae Remodeling as Key Mediators of Cellular Function. *Annu Rev Physiol, 78*, 505-531. doi: 10.1146/annurev-physiol-021115-105011

Phillips, M. J., & Voeltz, G. K. (2016). Structure and function of ER membrane contact sites with other organelles. *Nat Rev Mol Cell Biol, 17*(2), 69-82. doi: 10.1038/nrm.2015.8

Pinaud, F., & Dahan, M. (2011). Targeting and imaging single biomolecules in living cells by complementation-activated light microscopy with split-fluorescent proteins. *Proc Natl Acad Sci U S A, 108*(24), E201-210. doi: 10.1073/pnas.1101929108

Pinton, P., Ferrari, D., Magalhães, P., Schulze-Osthoff, K., Di Virgilio, F., Pozzan, T., & Rizzuto, R. (2000). Reduced loading of intracellular Ca(2+) stores and downregulation of capacitative Ca(2+) influx in Bcl-2-overexpressing cells. *J Cell Biol, 148*(5), 857-862. doi: 10.1083/jcb.148.5.857

Pinton, P., Giorgi, C., Siviero, R., Zecchini, E., & Rizzuto, R. (2008). Calcium and apoptosis: ER-mitochondria Ca2+ transfer in the control of apoptosis. *Oncogene, 27*(50), 6407-6418. doi: 10.1038/onc.2008.308

Poston, C. N., Duong, E., Cao, Y., & Bazemore-Walker, C. R. (2011). Proteomic analysis of lipid raft-enriched membranes isolated from internal organelles. *Biochem Biophys Res Commun, 415*(2), 355-360. doi: 10.1016/j.bbrc.2011.10.072

Pozzan, T., Rizzuto, R., Volpe, P., & Meldolesi, J. (1994). Molecular and cellular physiology of intracellular calcium stores. *Physiol Rev, 74*(3), 595-636. doi: 10.1152/physrev.1994.74.3.595

Prudent, J., Zunino, R., Sugiura, A., Mattie, S., Shore, G. C., & McBride, H. M. (2015). MAPL SUMOylation of Drp1 Stabilizes an ER/Mitochondrial Platform Required for Cell Death. *Mol Cell, 59*(6), 941-955. doi: 10.1016/j.molcel.2015.08.001

Qian, S., Wang, W., Yang, L., & Huang, H. W. (2008). Structure of transmembrane pore induced by Bax-derived peptide: evidence for lipidic pores. *Proc Natl Acad Sci U S A, 105*(45), 17379-17383. doi: 10.1073/pnas.0807764105

Rao, L., Perez, D., & White, E. (1996). Lamin proteolysis facilitates nuclear events during apoptosis. *Journal of Cell Biology, 135*(6), 1441-1455. doi: 10.1083/jcb.135.6.1441

Rieusset, J. (2018). The role of endoplasmic reticulum-mitochondria contact sites in the control of glucose homeostasis: an update. *Cell Death Dis, 9*(3), 388. doi: 10.1038/s41419-018-0416-1

Riley, J. S., Quarato, G., Cloix, C., Lopez, J., O'Prey, J., Pearson, M., . . . Tait, S. W. (2018). Mitochondrial inner membrane permeabilisation enables mtDNA release during apoptosis. *EMBO J, 37*(17). doi: 10.15252/embj.201899238

Rizzuto, R., Brini, M., Murgia, M., & Pozzan, T. (1993). Microdomains with high Ca2+ close to IP3-sensitive channels that are sensed by neighboring mitochondria. *Science, 262*(5134), 744-747. doi: 10.1126/science.8235595

Rizzuto, R., Pinton, P., Carrington, W., Fay, F. S., Fogarty, K. E., Lifshitz, L. M., . . . Pozzan, T. (1998). Close contacts with the endoplasmic reticulum as determinants of mitochondrial Ca2+ responses. *Science, 280*(5370), 1763-1766. doi: 10.1126/science.280.5370.1763

Rongvaux, A., Jackson, R., Harman, C. C., Li, T., West, A. P., de Zoete, M. R., . . . Flavell, R. A. (2014). Apoptotic caspases prevent the induction of type I interferons by mitochondrial DNA. *Cell, 159*(7), 1563-1577. doi: 10.1016/j.cell.2014.11.037

Ruby, J. R., Dyer, R. F., & Skalko, R. G. (1969). Continuities between mitochondria and endoplasmic reticulum in the mammalian ovary. *Z Zellforsch Mikrosk Anat, 97*(1), 30-37. doi: 10.1007/bf00331868

Sala-Vila, A., Navarro-Lérida, I., Sánchez-Alvarez, M., Bosch, M., Calvo, C., López, J. A., . . . Del Pozo, M. A. (2016). Interplay between hepatic mitochondria-associated membranes, lipid metabolism and caveolin-1 in mice. *Sci Rep, 6*, 27351. doi: 10.1038/srep27351

Salvador-Gallego, R., Mund, M., Cosentino, K., Schneider, J., Unsay, J., Schraermeyer, U., . . . García-Sáez, A. J. (2016). Bax assembly into rings and arcs in apoptotic mitochondria is linked to membrane pores. *EMBO J, 35*(4), 389-401. doi: 10.15252/embj.201593384

Samtleben, S., Jaepel, J., Fecher, C., Andreska, T., Rehberg, M., & Blum, R. (2013). Direct imaging of ER calcium with targeted-esterase induced dye loading (TED). *J Vis Exp*(75), e50317. doi: 10.3791/50317

Saraste, M. (1999). Oxidative phosphorylation at the fin de siècle. *Science, 283*(5407), 1488-1493. doi: 10.1126/science.283.5407.1488

Sarosiek, K. A., Chi, X., Bachman, J. A., Sims, J. J., Montero, J., Patel, L., . . . Letai, A. (2013). BID preferentially activates BAK while BIM preferentially activates BAX, affecting chemotherapy response. *Mol Cell, 51*(6), 751-765. doi: 10.1016/j.molcel.2013.08.048

Savill, J., & Fadok, V. (2000). Corpse clearance defines the meaning of cell death. *Nature, 407*(6805), 784-788. doi: 10.1038/35037722

Schellenberg, B., Wang, P., Keeble, J. A., Rodriguez-Enriquez, R., Walker, S., Owens, T. W., . . . Gilmore, A. P. (2013). Bax exists in a dynamic equilibrium between the cytosol and mitochondria to control apoptotic priming. *Mol Cell, 49*(5), 959-971. doi: 10.1016/j.molcel.2012.12.022

Schwarz, D. S., & Blower, M. D. (2016). The endoplasmic reticulum: structure, function and response to cellular signaling. *Cell Mol Life Sci, 73*(1), 79-94. doi: 10.1007/s00018-015-2052-6

Scorrano, L., Ashiya, M., Buttle, K., Weiler, S., Oakes, S. A., Mannella, C. A., & Korsmeyer, S. J. (2002). A distinct pathway remodels mitochondrial cristae and

mobilizes cytochrome c during apoptosis. *Dev Cell, 2*(1), 55-67. doi: 10.1016/s1534-5807(01)00116-2
Scorrano, L., Oakes, S. A., Opferman, J. T., Cheng, E. H., Sorcinelli, M. D., Pozzan, T., & Korsmeyer, S. J. (2003). BAX and BAK regulation of endoplasmic reticulum Ca2+: a control point for apoptosis. *Science, 300*(5616), 135-139. doi: 10.1126/science.1081208
Shamas-Din, A., Brahmbhatt, H., Leber, B., & Andrews, D. W. (2011). BH3-only proteins: Orchestrators of apoptosis. *Biochim Biophys Acta, 1813*(4), 508-520. doi: 10.1016/j.bbamcr.2010.11.024
Sheridan, C., Delivani, P., Cullen, S. P., & Martin, S. J. (2008). Bax- or Bak-induced mitochondrial fission can be uncoupled from cytochrome C release. *Mol Cell, 31*(4), 570-585. doi: 10.1016/j.molcel.2008.08.002
Shiao, Y. J., Lupo, G., & Vance, J. E. (1995). Evidence that phosphatidylserine is imported into mitochondria via a mitochondria-associated membrane and that the majority of mitochondrial phosphatidylethanolamine is derived from decarboxylation of phosphatidylserine. *J Biol Chem, 270*(19), 11190-11198. doi: 10.1074/jbc.270.19.11190
Shibata, Y., Voeltz, G. K., & Rapoport, T. A. (2006). Rough sheets and smooth tubules. *Cell, 126*(3), 435-439. doi: 10.1016/j.cell.2006.07.019
Somlyo, A. P., Bond, M., & Somlyo, A. V. (1985). Calcium content of mitochondria and endoplasmic reticulum in liver frozen rapidly in vivo. *Nature, 314*(6012), 622-625. doi: 10.1038/314622a0
Stone, S. J., Levin, M. C., Zhou, P., Han, J., Walther, T. C., & Farese, R. V., Jr. (2009). The endoplasmic reticulum enzyme DGAT2 is found in mitochondria-associated membranes and has a mitochondrial targeting signal that promotes its association with mitochondria. *J Biol Chem, 284*(8), 5352-5361. doi: 10.1074/jbc.M805768200
Stone, S. J., & Vance, J. E. (2000). Phosphatidylserine synthase-1 and -2 are localized to mitochondria-associated membranes. *J Biol Chem, 275*(44), 34534-34540. doi: 10.1074/jbc.M002865200
Subburaj, Y., Cosentino, K., Axmann, M., Pedrueza-Villalmanzo, E., Hermann, E., Bleicken, S., . . . García-Sáez, A. J. (2015). Bax monomers form dimer units in the membrane that further self-assemble into multiple oligomeric species. *Nat Commun, 6*, 8042. doi: 10.1038/ncomms9042
Sugiura, A., Nagashima, S., Tokuyama, T., Amo, T., Matsuki, Y., Ishido, S., . . . Yanagi, S. (2013). MITOL regulates endoplasmic reticulum-mitochondria contacts via Mitofusin2. *Mol Cell, 51*(1), 20-34. doi: 10.1016/j.molcel.2013.04.023
Sun, M. G., Williams, J., Munoz-Pinedo, C., Perkins, G. A., Brown, J. M., Ellisman, M. H., . . . Frey, T. G. (2007). Correlated three-dimensional light and electron microscopy reveals transformation of mitochondria during apoptosis. *Nat Cell Biol, 9*(9), 1057-1065. doi: 10.1038/ncb1630
Suzuki, M., Youle, R. J., & Tjandra, N. (2000). Structure of Bax: coregulation of dimer formation and intracellular localization. *Cell, 103*(4), 645-654. doi: 10.1016/s0092-8674(00)00167-7
Szabadkai, G., Bianchi, K., Várnai, P., De Stefani, D., Wieckowski, M. R., Cavagna, D., . . . Rizzuto, R. (2006). Chaperone-mediated coupling of endoplasmic reticulum and mitochondrial Ca2+ channels. *J Cell Biol, 175*(6), 901-911. doi: 10.1083/jcb.200608073
Szalai, G., Krishnamurthy, R., & Hajnóczky, G. (1999). Apoptosis driven by IP(3)-linked mitochondrial calcium signals. *EMBO J, 18*(22), 6349-6361. doi: 10.1093/emboj/18.22.6349
Taylor, R. C., Cullen, S. P., & Martin, S. J. (2008). Apoptosis: controlled demolition at the cellular level. *Nature Reviews Molecular Cell Biology, 9*(3), 231-241. doi: 10.1038/nrm2312

Thevathasan, J. V., Kahnwald, M., Cieśliński, K., Hoess, P., Peneti, S. K., Reitberger, M., . . . Ries, J. (2019). Nuclear pores as versatile reference standards for quantitative superresolution microscopy. *Nat Methods, 16*(10), 1045-1053. doi: 10.1038/s41592-019-0574-9

Tubbs, E., & Rieusset, J. (2016). Study of Endoplasmic Reticulum and Mitochondria Interactions by In Situ Proximity Ligation Assay in Fixed Cells. *J Vis Exp*(118). doi: 10.3791/54899

Tubbs, E., & Rieusset, J. (2017). Metabolic signaling functions of ER-mitochondria contact sites: role in metabolic diseases. *J Mol Endocrinol, 58*(2), R87-R106. doi: 10.1530/jme-16-0189

Ugarte-Uribe, B., & García-Sáez, A. J. (2014). Membranes in motion: mitochondrial dynamics and their role in apoptosis. *Biol Chem, 395*(3), 297-311. doi: 10.1515/hsz-2013-0234

Uren, R. T., O'Hely, M., Iyer, S., Bartolo, R., Shi, M. X., Brouwer, J. M., . . . Kluck, R. M. (2017). Disordered clusters of Bak dimers rupture mitochondria during apoptosis. *Elife, 6*. doi: 10.7554/eLife.19944

Vance, J. E. (1990). Phospholipid synthesis in a membrane fraction associated with mitochondria. *J Biol Chem, 265*(13), 7248-7256.

Vance, J. E. (2014). MAM (mitochondria-associated membranes) in mammalian cells: lipids and beyond. *Biochim Biophys Acta, 1841*(4), 595-609. doi: 10.1016/j.bbalip.2013.11.014

Verfaillie, T., Rubio, N., Garg, A. D., Bultynck, G., Rizzuto, R., Decuypere, J. P., . . . Agostinis, P. (2012). PERK is required at the ER-mitochondrial contact sites to convey apoptosis after ROS-based ER stress. *Cell Death Differ, 19*(11), 1880-1891. doi: 10.1038/cdd.2012.74

Verhagen, A. M., Ekert, P. G., Pakusch, M., Silke, J., Connolly, L. M., Reid, G. E., . . . Vaux, D. L. (2000). Identification of DIABLO, a mammalian protein that promotes apoptosis by binding to and antagonizing IAP proteins. *Cell, 102*(1), 43-53. doi: 10.1016/s0092-8674(00)00009-x

Voelker, D. R. (1989). Reconstitution of phosphatidylserine import into rat liver mitochondria. *J Biol Chem, 264*(14), 8019-8025.

Voelker, D. R. (2003). New perspectives on the regulation of intermembrane glycerophospholipid traffic. *J Lipid Res, 44*(3), 441-449. doi: 10.1194/jlr.R200020-JLR200

Voelker, D. R. (2005). Bridging gaps in phospholipid transport. *Trends Biochem Sci, 30*(7), 396-404. doi: 10.1016/j.tibs.2005.05.008

Wajant, H. (2002). The Fas Signaling Pathway: More Than a Paradigm. *Science, 296*(5573), 1635-1636. doi: 10.1126/science.1071553

Walensky, L. D., Pitter, K., Morash, J., Oh, K. J., Barbuto, S., Fisher, J., . . . Korsmeyer, S. J. (2006). A stapled BID BH3 helix directly binds and activates BAX. *Mol Cell, 24*(2), 199-210. doi: 10.1016/j.molcel.2006.08.020

Wasiak, S., Zunino, R., & McBride, H. M. (2007). Bax/Bak promote sumoylation of DRP1 and its stable association with mitochondria during apoptotic cell death. *J Cell Biol, 177*(3), 439-450. doi: 10.1083/jcb.200610042

Wei, M. C., Zong, W. X., Cheng, E. H., Lindsten, T., Panoutsakopoulou, V., Ross, A. J., . . . Korsmeyer, S. J. (2001). Proapoptotic BAX and BAK: a requisite gateway to mitochondrial dysfunction and death. *Science, 292*(5517), 727-730. doi: 10.1126/science.1059108

West, M., Zurek, N., Hoenger, A., & Voeltz, G. K. (2011). A 3D analysis of yeast ER structure reveals how ER domains are organized by membrane curvature. *J Cell Biol, 193*(2), 333-346. doi: 10.1083/jcb.201011039

Westphal, D., Dewson, G., Menard, M., Frederick, P., Iyer, S., Bartolo, R., . . . Kluck, R. M. (2014). Apoptotic pore formation is associated with in-plane insertion of Bak or Bax central helices into the mitochondrial outer membrane. *Proc Natl Acad Sci U S A, 111*(39), E4076-4085. doi: 10.1073/pnas.1415142111

Westphal, D., Kluck, R. M., & Dewson, G. (2014). Building blocks of the apoptotic pore: how Bax and Bak are activated and oligomerize during apoptosis. *Cell Death Differ, 21*(2), 196-205. doi: 10.1038/cdd.2013.139

Whitaker, M. (2010). Genetically encoded probes for measurement of intracellular calcium. *Methods Cell Biol, 99*, 153-182. doi: 10.1016/b978-0-12-374841-6.00006-2

White, M. J., McArthur, K., Metcalf, D., Lane, R. M., Cambier, J. C., Herold, M. J., . . . Kile, B. T. (2014). Apoptotic caspases suppress mtDNA-induced STING-mediated type I IFN production. *Cell, 159*(7), 1549-1562. doi: 10.1016/j.cell.2014.11.036

Wieckowski, M. R., Giorgi, C., Lebiedzinska, M., Duszynski, J., & Pinton, P. (2009). Isolation of mitochondria-associated membranes and mitochondria from animal tissues and cells. *Nat Protoc, 4*(11), 1582-1590. doi: 10.1038/nprot.2009.151

Williams, A., Hayashi, T., Wolozny, D., Yin, B., Su, T. C., Betenbaugh, M. J., & Su, T. P. (2016). The non-apoptotic action of Bcl-xL: regulating Ca(2+) signaling and bioenergetics at the ER-mitochondrion interface. *J Bioenerg Biomembr, 48*(3), 211-225. doi: 10.1007/s10863-016-9664-x

Willis, S. N., Chen, L., Dewson, G., Wei, A., Naik, E., Fletcher, J. I., . . . Huang, D. C. (2005). Proapoptotic Bak is sequestered by Mcl-1 and Bcl-xL, but not Bcl-2, until displaced by BH3-only proteins. *Genes Dev, 19*(11), 1294-1305. doi: 10.1101/gad.1304105

Willis, S. N., Fletcher, J. I., Kaufmann, T., van Delft, M. F., Chen, L., Czabotar, P. E., . . . Huang, D. C. (2007). Apoptosis initiated when BH3 ligands engage multiple Bcl-2 homologs, not Bax or Bak. *Science, 315*(5813), 856-859. doi: 10.1126/science.1133289

Wolburg-Buchholz, K., Mack, A. F., Steiner, E., Pfeiffer, F., Engelhardt, B., & Wolburg, H. (2009). Loss of astrocyte polarity marks blood-brain barrier impairment during experimental autoimmune encephalomyelitis. *Acta Neuropathol, 118*(2), 219-233. doi: 10.1007/s00401-009-0558-4

Wolter, K. G., Hsu, Y. T., Smith, C. L., Nechushtan, A., Xi, X. G., & Youle, R. J. (1997). Movement of Bax from the cytosol to mitochondria during apoptosis. *J Cell Biol, 139*(5), 1281-1292. doi: 10.1083/jcb.139.5.1281

Wright, D. J., Renoir, T., Smith, Z. M., Frazier, A. E., Francis, P. S., Thorburn, D. R., . . . Gray, L. J. (2015). N-Acetylcysteine improves mitochondrial function and ameliorates behavioral deficits in the R6/1 mouse model of Huntington's disease. *Translational psychiatry, 5*(1), e492-e492. doi: 10.1038/tp.2014.131

Xu, X. P., Zhai, D., Kim, E., Swift, M., Reed, J. C., Volkmann, N., & Hanein, D. (2013). Three-dimensional structure of Bax-mediated pores in membrane bilayers. *Cell Death Dis, 4*(6), e683. doi: 10.1038/cddis.2013.210

Yamaguchi, R., Lartigue, L., Perkins, G., Scott, R. T., Dixit, A., Kushnareva, Y., . . . Newmeyer, D. D. (2008). Opa1-mediated cristae opening is Bax/Bak and BH3 dependent, required for apoptosis, and independent of Bak oligomerization. *Mol Cell, 31*(4), 557-569. doi: 10.1016/j.molcel.2008.07.010

Yang, Z., Zhao, X., Xu, J., Shang, W., & Tong, C. (2018). A novel fluorescent reporter detects plastic remodeling of mitochondria-ER contact sites. *J Cell Sci, 131*(1). doi: 10.1242/jcs.208686

Yi, M., Weaver, D., & Hajnóczky, G. (2004). Control of mitochondrial motility and distribution by the calcium signal: a homeostatic circuit. *J Cell Biol, 167*(4), 661-672. doi: 10.1083/jcb.200406038

Youle, R. J., & Strasser, A. (2008). The BCL-2 protein family: opposing activities that mediate cell death. *Nature Reviews Molecular Cell Biology, 9*(1), 47-59. doi: 10.1038/nrm2308

Zhai, D., Jin, C., Huang, Z., Satterthwait, A. C., & Reed, J. C. (2008). Differential regulation of Bax and Bak by anti-apoptotic Bcl-2 family proteins Bcl-B and Mcl-1. *J Biol Chem, 283*(15), 9580-9586. doi: 10.1074/jbc.M708426200